



ISSN 1028-8546

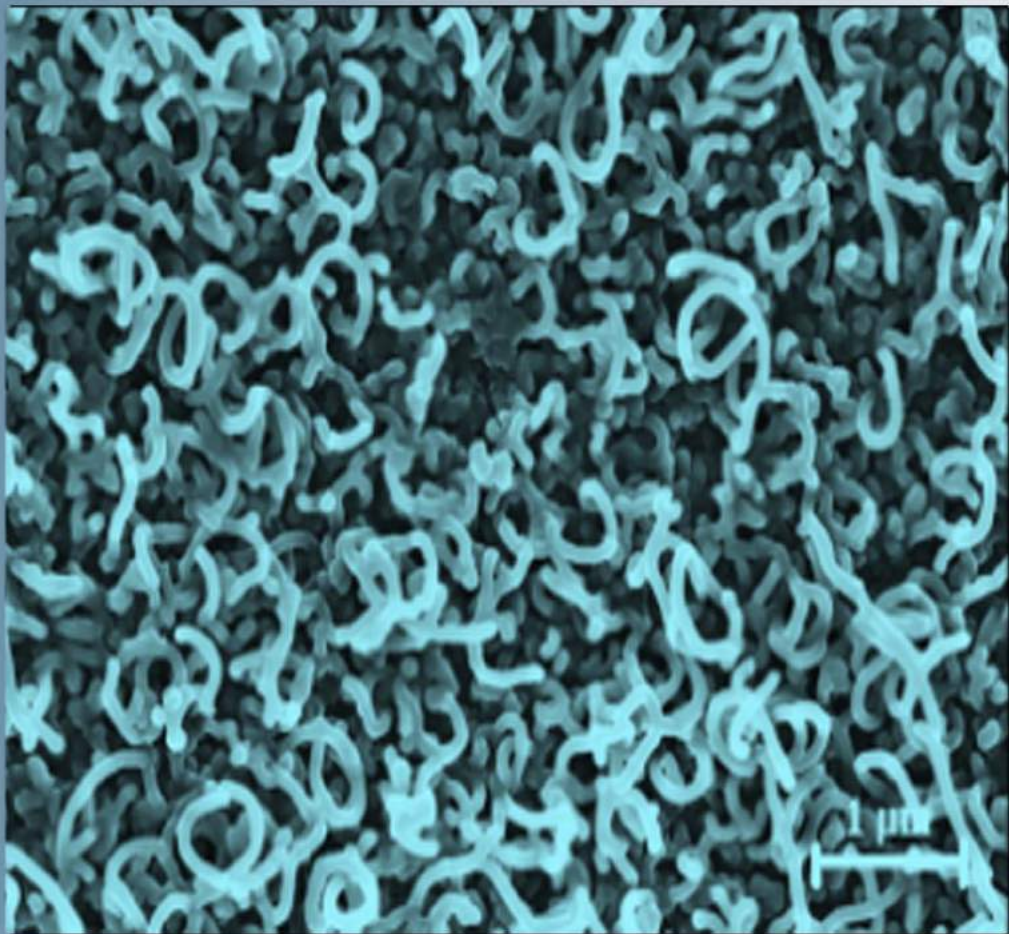
Volume XXIV, Number 3

Section: En

October, 2018

Azerbaijan Journal of Physics

Fizika



www.physics.gov.az

G.M. Abdullayev Institute of Physics
Azerbaijan National Academy of Sciences
Department of Physical, Mathematical and Technical Sciences

Published from 1995
Ministry of Press and Information
of Azerbaijan Republic,
Registration number 402, 16.04.1997

ISSN 1028-8546
vol. XXIV, Number 03, 2018
Series: En

Azerbaijan Journal of Physics

FIZIKA

*G.M.Abdullayev Institute of Physics
Azerbaijan National Academy of Sciences
Department of Physical, Mathematical and Technical Sciences*

HONORARY EDITORS

Arif PASHAYEV

EDITORS-IN-CHIEF

Nazim MAMEDOV

Chingiz QAJAR

SENIOR EDITOR

Talat MEHDIYEV

INTERNATIONAL REVIEW BOARD

Ivan Scherbakov, Russia
Kerim Allahverdiyev, Azerbaijan
Mehmet Öndr Yetiş, Turkey
Gennadii Jablonskii, Buelorussia
Rafael Imamov, Russia
Vladimir Man'ko, Russia
Eldar Salayev, Azerbaijan
Dieter Hochheimer, USA
Victor L'vov, Israel
Vyacheslav Tuzlukov, South Korea

Majid Ebrahim-Zadeh, Spain
Firudin Hashimzadeh, Azerbaijan
Anatoly Boreysho, Russia
Mikhail Khalin, Russia
Hasan Bidadi, Tebriz, Iran
Natiq Atakishiyev, Mexico
Tayar Djafarov, Azerbaijan
Arif Hashimov, Azerbaijan
Javad Abidinov, Azerbaijan
Bagadur Tagiyev, Azerbaijan

Talat Mehdiyev, Azerbaijan
Vali Huseynov, Azerbaijan
Ayaz Baramov, Azerbaijan
Tofiq Mammadov, Azerbaijan
Salima Mehdiyeva, Azerbaijan
Shakir Nagiyev, Azerbaijan
Rauf Guseynov, Azerbaijan
Almuk Abbasov, Azerbaijan
Yusif Asadov, Azerbaijan

TECHNICAL EDITORIAL BOARD

Senior secretary Elmira Akhundova, Nazli Guseynova, Sakina Aliyeva,
Nigar Akhundova, Elshana Aleskerova, Rena Nayimbayeva

PUBLISHING OFFICE

131 H.Javid ave, AZ-1143, Baku
ANAS, G.M.Abdullayev Institute of Physics

Tel.: (99412) 539-51-63, 539-32-23
Fax: (99412) 537-22-92
E-mail: jophphysics@gmail.com
Internet: www.physics.gov.az

It is authorized for printing:

Published at "SƏRQ-QƏRB"
17 Ashug Alessger str., Baku
Typographer : Aziz Gulaliyev

Sent for printing on: ___.__. 201__
Printing approved on: ___.__. 201__
Physical binding: _____
Number of copies: _____200
Order: _____

SPECTRAL VARIABILITY OF THE LINE HeI 5876Å/Be HERBIG TYPE STAR HD 179218

A.N. ADIGEALZADE

*N. Tusi Shamakhy Astrophysical Observatory of Azerbaijan National
Academy of Sciences, Y. Mamedaliyev settl.,
Shamakhy, Azerbaijan, AZ 5626
hadigozalzade@gmail.com*

The results of spectral observations of the Herbig Ae/Be type star HD 179218 are presented. Two wave-like cycles of variability in the parameters of hydrogen lines H α and H β with a characteristic time of ~ 40 days are revealed. The first wave of variations is deeper; the branches of decreasing and increasing the spectral parameters of the lines are more clearly expressed. At the time of the first minimum, in the profile of the emission line H α the appearance and disappearance of additional blue and red emission components are observed. At the same time, narrow absorption components were discovered in the H β line. Synchronously with this, a significant variation in the lines of He I, Si II, D NaI, [OI] was observed. In addition, the parameters of many spectral lines shows variations with smaller amplitude and with a characteristic time of 10-20 days. Possible mechanisms of the observed variability of the star are discussed.

Keywords: stars: variables: Herbig Ae/Be– stars: circumstellar matter – stars: individual – HD179218

The Herbig Ae/Be type stars (HAeBe) are pre-main sequence (PMS) objects of intermediate mass 2-10 M_{\odot} and are considered to be the progenitors of Vega type stars, which are surrounded with a residual protoplanetary disk. Spectral monitoring of individual objects has shown that in the spectra of these stars are observed variable emission and absorption lines (see, for example, Praderie et al. (1986), Pogodin (1994), Rodgers et al. (2002), Mora et al., (2004)). The same features are also characteristic of classical T Tauri stars (CTTS) (see, for example, Johns & Basri (1995), Schisano et al. (2009) and references therein). It is known that in young stars, emission lines, as well as some absorption lines, are formed in the circumstellar disks or in the envelopes of the stars. Such circumstellar matter can often participate in accretion, polar outflows, winds and other forms of disk interaction with the central star. Tracking the variation in the observed spectral lines makes it possible to perform diagnostics of the physical processes that are occurring in the stellar atmosphere and in the circumstellar environment. In young stars, in particular, these processes can directly affect the formation of the planets and their evolution. Consequently, one of the important problems in the study of the early stage of evolution of stars is the study of the characteristics of the circumstellar structure and the processes of interaction of the central star with the surrounding matter.

HD 179218 (MWC 614, Sp B9-A2) is an isolated HAe/Be type star. Despite the fact that the star is relatively bright comparatively to other HAe stars, it has been studied less. Only when the star was included in the catalog of The et al. (1994), it became the subject of active research. The circumstellar surroundings of the star were studied by IR photometry and speckle interferometry by Millan-Gabet et al. (2001), Prizkal et al. (1997), which did not reveal closely spaced components. Spectral studies of the star were performed by Miroshnichenko et al. (1998) and in more detail, Kozlova (2004), Kozlova and Alexeev (2017).

According to the classification of Meeus et al. (2001), the spectral energy distribution (SED) of the star belongs to group I, i.e. starting with the infrared band K and further there is an excess of radiation excited in the dust. On the

Mendigutia et al. (2012) the profile of the line H α is consisting of a stable single-peak structure. Perhaps the star has a close companion, about 2.5 arcsec apart (Wheelwright et al., 2010). Fedele et al. (2008) showed that the star has two dust rings at distances of 1 AU and 20 AU, and the space between from 1 to 6 AU from the star filled with gas. The magnetic field of the star was measured by Hubrig et al. (2009) where on the data 2008 they have got about 51 ± 30 G.

The purpose of this paper is to carry out monitoring of the spectral variability of the star on spectral lines obtained in the visual range of spectrum.

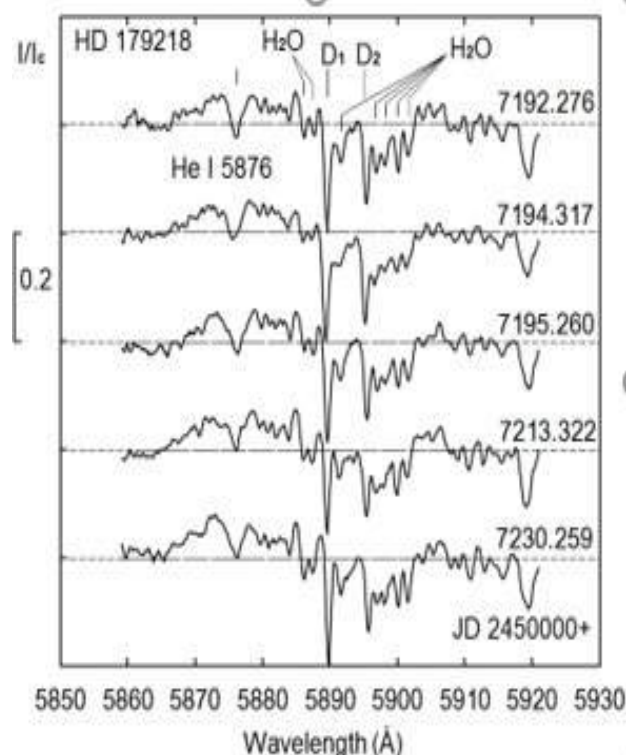


Fig.1. A spectral range of spectra is containing lines of HeI 5876 Å and doublet D1, D2 NaI. Individual sky (atmospheric) lines are indicated.

In the Figure 1 have shown the spectral region containing the lines He I $\lambda 5876 \text{ \AA}$ and the sodium doublet D1, D2 NaI. This section presents the results of the analysis for the helium line. As can be seen, this line has blue and red emission components separated by a central absorption. This is the line in which only a saddle-like two peak emission profile is observed. The average half-width of the absorption is 1.5 \AA with a scatter of up to 1.0 \AA . The total width of the line at the continuum level is more than 20 \AA . Figure 7 shows the profiles obtained at different nights, including at night JD 2457192 - 2457295, in which the first minimum of the spectral parameters of the hydrogen lines $H\alpha$ and $H\beta$ was obtained. As can be seen, the profile of the He I line $\lambda 5876 \text{ \AA}$ stably keeps the structure from night to night, does not show any noticeable variations.

The average value of the shift of the emission peaks in the He I line of 5876 \AA corresponds to approximately -

150 and +150 km/s, for the blue and red components, respectively. The radial velocities of individual emission peaks is showing a variability of about an average value 50 km/s. The central absorption is displaced about +20 km/s.

Figure 2 is presented diagrams of variations in the equivalent widths of the central absorption of EWa, the radial velocities of the absorption vertex Vp, the ratio of the equivalent widths of the blue component to the red EW1/EW2, and the half-width of the FWHM absorption in the line He I 5876. As can be seen, while parameters of the hydrogen lines are decreased, the parameters of the absorption component of the line He I 5876 is showing a certain variation: EWa tends to increase, Vp is shifted to the red part of the spectrum by about 20 km/s, the ratio EW1/EW2 is increased by 5-7 times, and the parameter FWHM is also increased. A decrease in the FWHM of the absorption is observed between two waves of parameter reduction.

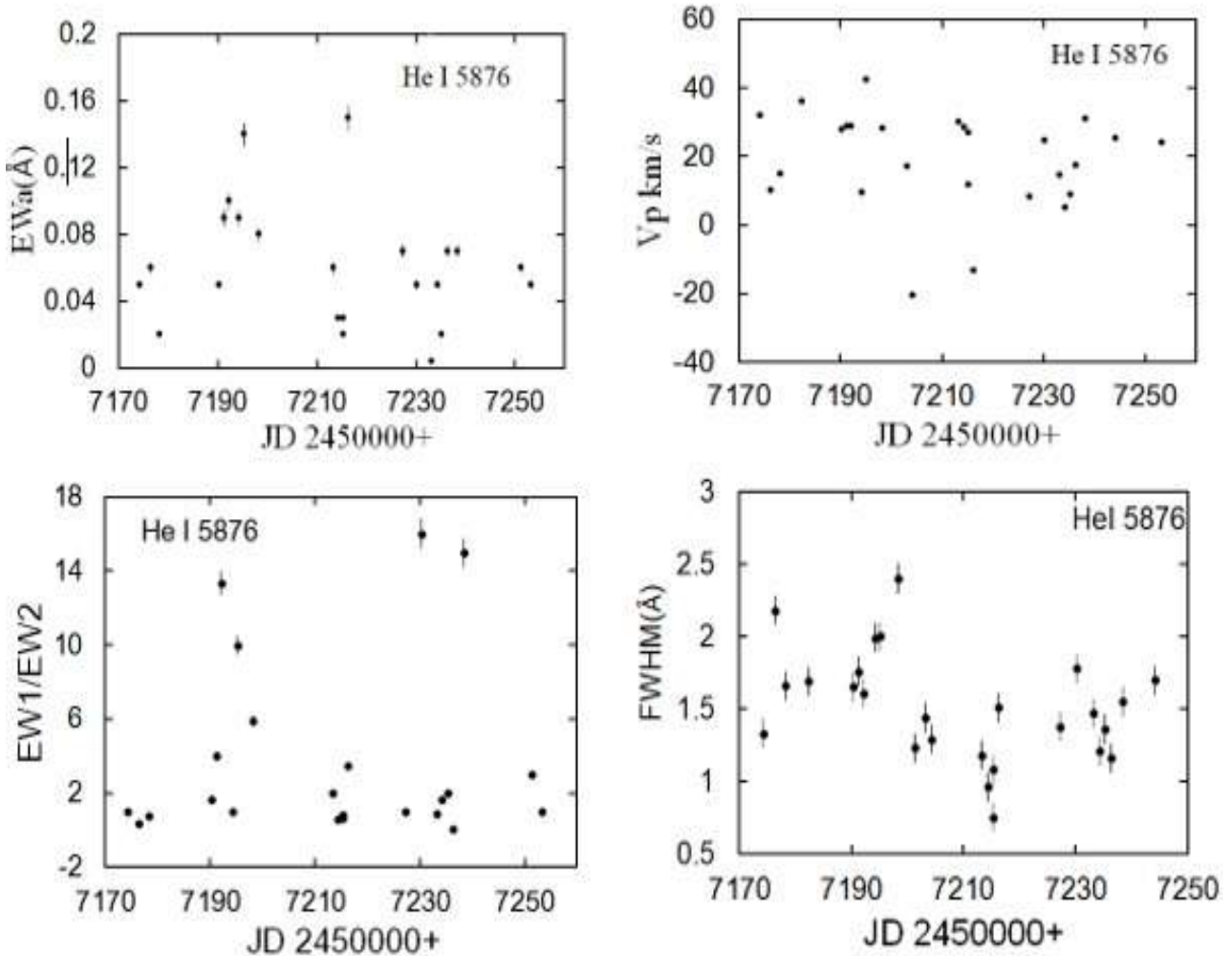


Fig.2. The time variation of the spectral parameters of the He I line is $\lambda 5876 \text{ \AA}$.

In Fig. 2, the top panels are from left to right EWa-equivalent width of the absorption component, Vp is the radial velocity of the absorption peak, lower panels - EW1/EW2 are the ratio of the equivalent widths of the blue emission component to red and the FWHM of the absorption component.

It is also possible that a star can be a spectral-double or multiple system. In fact, it is difficult to explain the observed wave-like variation of the radial velocities and other parameters of the $H\alpha$ line. Kozlova & Alekseev (2017) showed that the dependence of the brightness V on the color index V-I has two separate distributions. This fact is accepted by the authors in favor of the duality of a star.

The time of our observations from May to September 2015 corresponds to the minimum of the 4000-day cycle of variability found in Kozlova & Alekseev (2017). Therefore, the observed features of the variation in the spectrum of a star in the H α line can be related to the moment of the star's stay at the minimum of the 4000-day

cycle. Then the results obtained by us, perhaps, are a kind of unique event and can be observed only in the minima of the 4000-day cycle. Our observations have shown that in order to elucidate these questions it is necessary to perform a more dense series of photometric and spectral observations of the star.

-
- [1] *F. Praderie, T. Simon, C. Catala, & A. Boesgaard*, M. 1986, ApJ, 303,311
- [2] *M.A. Pogodin*, 1994, A&A, 282, 141
- [3] *B. Rodgers, D.H. Wooden, V. Grinin, et al.*, 2002, ApJ, 564, 405
- [4] *A. Mora, C. Eiroa, A. Natta, et al.* 2004, A&A, 419, 225
- [5] *C.M. Johns, & G. Basri* 1995, AJ, 109, 2800
- [6] *E. Schisano, E. Covino, J.M. Alcalá, et al.* 2009, A&A, 501, 1013
- [7] *R. Millan-Gabet, F.P. Schloerb, W.A. Traub* Ap.J. 2001, 546, 358
- [8] *N. Pirzkal, E.J. Spillar, H.M. Dyck*, Ap.J. 1997, 481, 392
- [9] *A.S. Miroshnichenko, K.S. Bjorkman, C.L. Mulliss et al.* PASP. 1998, 110, 883
- [10] *O.V. Kozlova*, Astrophysics, 2004, 47, No 3, 287
- [11] *O.V. Kozlova, I.Yu. Alekseev*, ASP Conf. Ser. 510, 153, (2017)
- [12] *G. Meeus, L.B.F.M. Waters, J. Bouwman et al.*, Astronomy and Astrophysics 365, 476 (2001).
- [13] *H.E.Wheelwright, R.D.Oudmaijer, S.P.Goodwin*, Monthly Notices Royal Astron. Soc. 401, 1199 (2010)

**KRAMERS-KRONIG ANALYSIS OF Ni_{1-x}Zn_xFe₂O₄ FERRITES
INFARED DIFFUSE REFLECTANCE SPECTRA**

Sh.A. AHMADOVA, A.A. SADIGOVA, Sh.N. ALIYEVA, T.R. MEHDIYEV

*G.M. Abdullayev Institute of Physics of NASA
Azerbaijan AZ-1143, Baku, H. Javid ave., 131*

The results of the analysis of infrared spectra Ni_{1-x}Zn_xFe₂O₄ ferrite are presented [1] by Kramers - Kronig. The spectra of n, k, ε_i, ε_r, Im(ε⁻¹) are calculated. As is known, the process involves the addition of ions Zn to the structure of zinc-nickel ferrite in the form (Zn_x²⁺Fe_{1-x}³⁺)[Ni_{1-x}²⁺Fe_{1+x}³⁺]O₄, where there is change in the zinc in the substrate to the coherent change of Fe in A- and B-sublattices and Ni in B. On the sublattice, the ion junctions are derived from the A sublattice of the subgroup of Ni octahedral voids, thereby forming the FeO₆ complex. Precisely, this process is accompanied by changes in charge and spins distributions, and, consequently, with superfluous and double bonded interconnections of cation nickel and glue. It is shown that the observed spectra of spectra are reflected by the ferrite correlation with the Ni²⁺, Zn²⁺, Fe²⁺ and Fe³⁺ concentrations in the different concentrations.

Keywords: Kramers-Kronig analysis, IR spectra, ferrites

PACS: 71.23

The features of the infrared diffuse reflectance spectra of Ni_{1-x}Zn_xFe₂O₄ ferrites with different concentrations of Zn [1] in the range from 4000 cm⁻¹ to 50 cm⁻¹ were interpreted by analyzing the results of studies of these spectra by the Kramers-Kronig (KK) procedure. The spectral dependences n(ω), k(ω), ε_i(ω), ε_r(ω) and loss function Im(ε(ω))⁻¹ are established. The KK method has long been used to analyze the reflection spectra to obtain various optical parameters of materials [2-15]. This can be due to it being easier to develop and can be applied to analyze a wide variety of materials (organic to inorganic, solid to liquid, and single crystal, polycrystalline, and amorphous) without reference to specific models. However, the application of the KK method was hindered by its complexity of the integration.

Many algorithms have been proposed for the Kramers-Kronig (KK) analysis [16]. However, none can be applied to any reflection spectrum without giving rise to unphysical effects. Furthermore, they do not make possible determination of the values of the optical constants; only the shape of the optical constants spectra is determined, more or less precisely. In this paper an algorithm for KK analysis is presented in which the disadvantages described above are removed as far as possible [17]. This algorithm can be applied for any reflectivity (R) spectrum measured in the visible or ultraviolet, in the energy range (ω, ω₀). As additional data, the curve for the absorption coefficient (α) in the range (0, ω) is required. KK analysis is based on the use of the following formula [18]:

$$\theta(\omega_0) = \frac{\omega_0}{\pi} \int_0^\infty \frac{\ln R(\omega) - \ln R(\omega_0)}{\omega^2 - \omega_0^2} d\omega \quad (1)$$

where θ denotes the phase shift of the electromagnetic wave on reflection. The KK integral (1) requires a knowledge of R throughout the entire energy range, not only in the measuring energy range (ω, ω₀). Thus, the necessity for R-extrapolations in both the low-energy range (0, ω) and the high-energy range (ω₀, ∞) arises. Obviously, the artificial R-extrapolation never gives the same values of θ as the experimental R-curve. Thus, there is an extrapolation error in the calculated optical constants.

The method of extrapolation error determination presented previously [19] tends towards overestimation of the error.

The infrared reflectance spectroscopy is a main tool for optical investigations in the IR spectral range. The optical parameters of a system under investigation, the dielectric function ε(ω) or the optical conductivity σ(ω) which is directly related with the dielectric function as ε(ω) = 1 + i4πσ(ω)/ω are determined from the reflectivity spectrum R(ω) making use of the KK relations. The KK analysis, however, requires for extrapolations of the experimental data to the low- and high-frequency limits, which usually essentially reduces an accuracy of the analysis. We present an algorithm of the Kramers-Kronig analysis based on an anchor-window technique. The high-frequency asymptote of the reflectivity spectrum is determined by a minimization of differences between the KK-deduced optical conductivity σ_{KK}(ω) and the known σ(ω) values, measured a priori in a small anchor-window.

Following results with KK relations are expressed figure 1.

The analysis of IR spectra of investigated compositions of Ni_{1-x}Zn_xFe₂O₄ ferrites in 4000cm⁻¹ - 500cm⁻¹ range shows that the information about IR spectra of ZnO, NiO and Fe₂O₃ components is necessary for interpretation of spectral peculiarities (see fig.1).

The complex reflectance spectrum is mathematically decomposed into two separate spectra - extinction coefficient and refractive index spectrum. These are also called K and N spectra. The real (n = refractive index) and imaginary (k = extinction) parts of the complex index of refraction are calculated from the reflectance spectrum using the following formulas:

$$n(\omega) = \frac{1 - R(\omega)}{1 + R(\omega) - 2\sqrt{R(\omega)} \cos(\theta(\omega))} \quad (2)$$

$$k(\omega) = \frac{2\sqrt{R(\omega)} \sin(\theta(\omega))}{1 + R(\omega) - 2\sqrt{R(\omega)} \cos(\theta(\omega))}$$

where R is the reflectance, n – wavenumber, θ – phase shift angle of the sample.

KRAMERS-KRONIG ANALYSIS OF $Ni_{1-x}Zn_xFe_2O_4$ FERRITES INFARED DIFFUSE REFLECTANCE SPECTRA

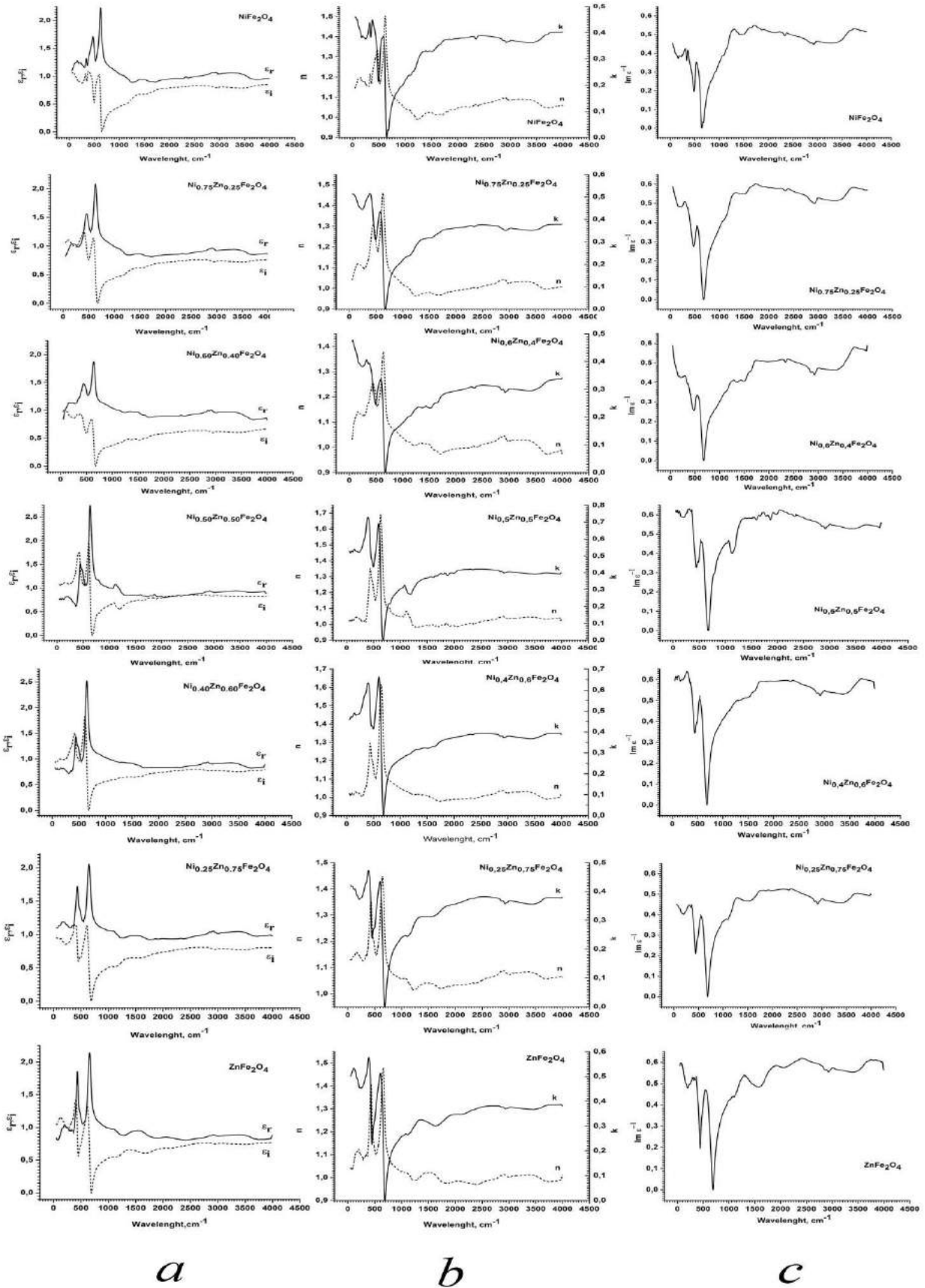


Fig.1 Dependence of ϵ_r , ϵ_i , n , k and $Im(\epsilon^{-1})$ of $Ni_{1-x}Zn_xFe_2O_4$ ferrites in different concentrations.

Extrapolation to zero frequency is easy to produce if we suggest that the reflection R approaches a value that is usually known and remains constant. It is assumed that in the extrapolation region there is no sharp structure characteristic for interband transitions. The reflection should be quite high at frequencies below the frequency of plasma oscillations and rapidly decrease at frequencies greater than the plasma frequency. In this case, the change in reflection is given by the expression:

$$R(\omega) = c\omega^{-4}$$

For a given wavenumber, the phase shift is calculated using the equation (3):

$$\begin{aligned} \varepsilon_r(\omega) &= (n^2 - k^2)_{\omega_0} = 1 + \frac{2}{\pi} \int_0^{\infty} \frac{\omega \varepsilon_i(\omega)}{\omega^2 - \omega_0^2} d\omega \\ \varepsilon_i(\omega) &= (2nk)_{\omega_0} = -\frac{2\omega_0}{\pi} \int_0^{\infty} \frac{\varepsilon_r(\omega)}{\omega^2 - \omega_0^2} d\omega \end{aligned} \quad (3)$$

As it is known, the incorporation of Zn ions into the structure of the nickel-zinc ferrite is recorded in the form of $(Zn_x^{2+}Fe_{1-x}^{3+})[Ni_{1-x}^{2+}Fe_{1+x}^{3+}]O_4$, that is, a change in the zinc content in the A-sublattice leads to a consistent change in the Fe content in the A and B-sublattices and Ni in the B-sublattice, the iron ions being displaced from the A-sublattice to the octahedral sites of the B-sublattice released from Ni, that is, forming FeO_6 . Naturally, such a process is accompanied by changes in charge and spin distributions and, consequently, super- and double exchange interactions involving nickel and iron cations. It is shown that the observed changes in the reflection spectra of these ferrites are connected with the redistribution of Ni^{2+} , Zn^{2+} , Fe^{2+} and Fe^{3+} ions concentration in different compounds.

This work was supported by the Science Development Foundation under The President of the Republic of Azerbaijan-Grant № EIF-BGM-3-BRFTF-2+/2017-15/04/1.

-
- [1] A.A. Sadigova, S.A. Ahmadova, Sh.N. Aliyeva, T.R. Mehdiyev, IR Diffuse Reflectance Spectra of Nanopowders of $Ni_{1-x}Zn_xFe_2O_4$ Ferrites, AJP Fizika XXIV, 2018, s.26
- [2] F. Stern, 1961. Optical Properties of Lead-salt and III-V Semiconductors. J. Appl. Phys. 32(10): 2166-2173
- [3] D.M. Roessler 1966. Kramers-Kronig Analysis of Reflection Data: III. Approximations, with Reference to Sodium Iodide. Brit. J. Appl. Phys. 17: 1313-1317
- [4] A. Hadni, J. Claudel, D. Chanal, P. Strimer, and P. Vergnat. 1967. Optical Constants of Potassium Bromide in the Far Infrared. Phys. Rev. 163(3): 836-843
- [5] J.J. White 1972. Optical Properties of Silver Bromide. J. Opt. Soc. Am. 62: 212-218
- [6] M.R. Querry, R.C. Waring, W.E. Holland, G.M. Hale, and W. Nijm. 1972. Optical Constants in the Infrared for Aqueous Solutions of NaCl. J. Opt. Soc. Am. 62(7): 849-855
- [7] A.S. Barker, and M. Ilegems. 1973. Infrared Lattice Vibrations and Free-Electron Dispersion in GaN. Physical Review B. 7(2): 743-750
- [8] R.S. Bauer, W.E. Spicer, and J.J. White, III. 1974. Investigation of the Kramer-Kronig Analysis: Revised Optical Constants of AgCl. J. Opt. Soc. Am. 64(6): 830-833
- [9] L.N. Didrikil, 1975. Determination of the Optical Constants of Condensed Media from the Reflectance Spectra of Nonpolarized or Partly Polarized Light at an Oblique Angle of Incidence Using Kramers-Kronig Method. Opt. Spectrosc. 38(2): 202-205
- [10] K.A. Maslin, C. Patel, and T.J. Parker. 1991. Far-infrared Optical Constants of a Selection of Zincblende Structure Crystals at 300 K. Infrared Phys. 32: 303-310
- [11] K. Kamaras, K.-L. Barth, F. Keilmann, R. Henn, M. Reedyk, C. Thomsen, M. Cardona, J. Kircher, P. L. Richards, and J. -L. Stehle. 1995. The Low-Temperature Infrared Optical Functions of SrTiO3 Determined by Reflectance Spectroscopy and Spectroscopic Ellipsometry. J. Appl. Phys. 78(2): 1235-1240
- [12] K. Yamamoto, and A. Masui. 1995. Complex Reflective Index Determination of Bulk Materials from Infrared Reflection Spectra. Appl. Spectrosc. 49(5): 639-644
- [13] H. Ishida, and K. Yamamoto. 1997. Complex Reflective Index Determination for Uniaxial Anisotropy with the Use of Kramers-Kronig Analysis. Appl. Spectrosc. 51(9): 1287-1293
- [14] E.I. Kamitsos, Y. D. Yannopoulos, C. P. Varsamis, and H. Jain. 1997. Structure-property Correlation in Glasses by Infrared Reflectance Spectroscopy. J. Non-Cryst. Solids. 222: 59-68
- [15] D.M. Roessler, 1965. Kramers-Kronig Analysis of Reflection Data. Brit. J. Appl. Phys. 16: 1119-1123
- [16] K. Jezierski, J. Misiewicz, J. Wnuk and J.M. Pawlikowski, 1981 Opt. Appl. 11 571-97
- [17] K. Jezierski 1984a PhD Thesis Technical University of Wroctaw
- [18] F. Stern, 1963 Solid State Phys. 15 299-408 (New York: Academic)
- [19] K. Jezierski, 1984b J. PhJs. C: Solid State Phys. 17 475-82

RESPONSE OF SILVER CHALCOGALLATES TO X-RAYS

S.M. ASADOV ^{1*}, S.N. MUSTAFAEVA ², V.F. LUKICHEV ³¹*Nagiev Institute of Catalysis and Inorganic Chemistry, ANAS, Baku, Azerbaijan.*salim7777@gmail.com²*Institute of Physics, ANAS, Baku, Azerbaijan.* solmust@gmail.com³*Institute of Physics and Technology of RAS, Moscow, Russia* icic.lab6@yandex.ru

A technique is proposed for producing single crystals of silver thiogallates with high X-ray conductivity and sensitivity coefficients at room temperature. Single crystals of AgGaSe₂ grown by chemical transport reactions method in comparison with AgGaS₂ and AgGaS_{2x}Se_{2-2x} had the highest X-ray sensitivity. At an effective radiation hardness of 30 keV and a dose rate of $\dot{E} = 10$ R / min the coefficient of roentgen sensitivity $K = 5.4 \times 10^{-13}$ (A min)/(V R) for AgGaS₂ and $K = 15 \times 10^{-13}$ (A min)/(V R) for AgGaSe₂. The coefficient of X-ray conductivity AgGaSe₂ varies within 1.2–8.5 min / R an effective radiation hardness of $V_a = 25$ –50 keV and a dose rate of $\dot{E} = 0.75$ –31.3 R / min.

Keywords: X-ray, AgGaS_{2x}Se_{2-2x}, single crystals, effective radiation hardness, chemical transport reactions

PACs: 61.05.–a, 61.43

AgGaS₂ single crystals can be produced by the Bridgman-Stockbarger (BS) technique [1-3]. This method makes it possible to reduce the cooling rate of grown crystals and obtain single crystals of high optical quality with an absorption coefficient of 0.1 cm⁻¹. However, high pressures in the furnace, on the one hand, require cumbersome experimental equipment and, on the other hand, reduce the heater temperature accuracy.

The aim of this study was to obtain optically homogeneous based AgGaS₂ single crystals with high X-ray sensitivity. Single crystals were grown by the BS technique and also using the method of chemical transport reactions (CTR). AgGaS₂ was synthesized from its elementary components: Ag (high purity grade), Ga (5N grade), S (high purity grade, TU 609254677), and Se (TU 6-09-2521-77). The initial synthesis components were taken in a stoichiometric ratio. The synthesis was performed in a horizontal furnace with the temperature within it increasing at a rate of 50 K/h to 1275 K. The reaction between the components proceeded for 4 h.

The synthesized material was transferred to an ampule into a dual chamber vertical furnace for growth. AgGaS₂ single crystals were grown using the BS technique. The AgGaS₂ melting temperature was $T_m = 1271 \pm 3$ K. The thermal conditions in the furnace were maintained using VRT-3 high-precision temperature controllers. The temperature gradient at the crystallization front in the furnace was 3 K/mm. The ampule with molten material was lowered vertically and cooled at a rate of 0.5 mm/h. Following crystallization, the furnace was turned off and cooled to room temperature together with the sample.

The growth of AgGaS_{2x}Se_{2-2x} ($x = 0; 0.5$ и 1.0) single crystals was performed by the CTR method. AgGaX₂ (X – S, Se) are taken together with the transporting agent iodine in the ampoule for the crystal growth. They react to form the gaseous binary iodides and selenium at high temperature. All these gaseous species diffuse to the colder growth zone due to the drop in temperature. At the growth zone they react back to form the ternary chalcogenide with the release of iodine. The iodine liberated diffuses back to the source end to form the metal iodides once again. The

main advantage of growing single crystals using the CTR method is the ability to conduct the process at lower temperatures and pressures.

The results of X-ray studies at room temperature showed that single crystals based on the AgGaS₂ compound crystallize in the chalcopyrite structure with the lattice parameters $a = 5.7571$ – 5.7572 Å and $c = 10.3110$ – 10.3036 Å for AgGaS₂ and $a = 5.992$; $c = 10.883$ Å for AgGaSe₂. The results of analyzing the X-ray dosimetry properties of AgGaS_{2x}Se_{2-2x} single crystals are detailed below. All measurements were conducted at $T = 300$ K. The studied AgGaS_{2x}Se_{2-2x} single crystals exhibited high sensitivity to X-ray radiation. The X-ray conductivity coefficient (relative change in electric conductivity of crystal due to X-ray radiation at a given dose) of a sample was determined by the following equation:

$$K_{\sigma} = \frac{\sigma_E - \sigma_0}{\sigma_0 \cdot E} \quad (1)$$

where σ_E is the sample electric conductivity (Ohm⁻¹cm⁻¹) under the action of X-ray irradiation with a dose rate of \dot{E} (R/min) and σ_0 is the dark electric conductivity of a single crystal. The X-ray sensitivity (A min)/(V R) of a single crystal was calculated as

$$K = \frac{\Delta I_{E,0}}{U \cdot E} \quad (2)$$

where $\Delta I_{E,0} = I_E - I_0$; I_E is the current strength in the sample at an X-ray dose rate of \dot{E} (R/min), I_0 is the dark current, and U is the external voltage applied to the sample.

Fig. 1 shows the dependences of the X-ray sensitivity coefficient on the X-ray dose for an AgGaS₂ single crystal at $T = 300$ K and $U = 60$ V. It can be seen that the X-ray sensitivity of AgGaS₂ varied from 1.3×10^{-11} to 1.4×10^{-10} (A min)/(V R). It was found that the X-ray sensitivity coefficient of AgGaS₂ increased with increasing radiation dose. The value of K increased fairly rapidly at $V_a = 25$ keV. At higher values of effective hardness of X-ray

radiation, the $K(E)$ dependence flattened; the X-ray sensitivity depended only weakly on E at $V_a = 50$ keV. Similar patterns were observed in the case of the dose dependence of X-ray conductivity coefficient K_σ of AgGaS₂ single crystals.

Single crystals of AgGaSe₂ grown by CTR method in comparison with AgGaS₂ and AgGaS_{2x}Se_{2-2x} had the highest X-ray sensitivity. At an effective radiation hardness of 30 keV and a dose rate of $E = 10$ R/min the coefficient of roentgen sensitivity $K = 5.4 \times 10^{-13}$ (A min)/(V R) for AgGaS₂ and $K = 15 \times 10^{-13}$ (A min)/(V R) for AgGaSe₂ (Figs. 2 and 3). The coefficient of X-ray conductivity AgGaSe₂ varies within 1.2–8.5 min/R an effective radiation hardness of $V_a = 25$ –50 keV and a dose rate of $E = 0.75$ –31.3 R/min. It was found that the X-ray sensitivity coefficient of AgGaS_{2x}Se_{2-2x} increased with increasing radiation dose. The value of K increased fairly rapidly at $V_a = 25$ keV. At higher values of effective hardness of X-ray radiation, the $K(E)$ dependence flattened; the X-ray sensitivity depended only weakly on E at $V_a = 50$ keV. Similar patterns were observed in the case of the dose dependence of K_σ of AgGaS_{2x}Se_{2-2x} single crystals.

The X-ray ampere characteristics of AgGaS_{2x}Se_{2-2x} single crystals were also studied. It follows from the results of these studies that the dependence of the steady X-ray current on the X-ray radiation dose is a power law one:

$$I_r = \Delta I_{E,0} = I_E - I_0 \sim E^\alpha.$$

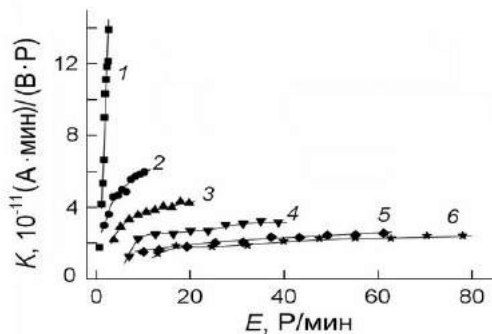


Fig. 1. Dependences of X-ray sensitivity coefficient on irradiation dose rate for AgGaS₂ (BS method) single crystal ($T = 300$ K and $U = 60$ V) at various accelerating voltages V_a (keV) applied to tube: 25 (1), 30 (2), 35 (3), 40 (4), 45 (5), and 50 (6).

The values of α for the studied single crystals varied depending on the effective hardness of X-ray radiation

from 2–2.5 at $V_a = 25$ keV to 1.2–1.3 at $V_a = 30$ –50 keV. The X-ray ampere characteristics of studied single crystals tended toward linearity ($\alpha \rightarrow 1$) at higher V_a values. This is important from a practical standpoint. We also investigated the X-ray current in the AgGaS_{2x}Se_{2-2x} samples and found that the dark current in the samples, in contrast to CdIn₂S₄ and CdGa₂S₄ single crystals [2, 3], reached a steady state value almost immediately after the X-ray radiation was turned off.

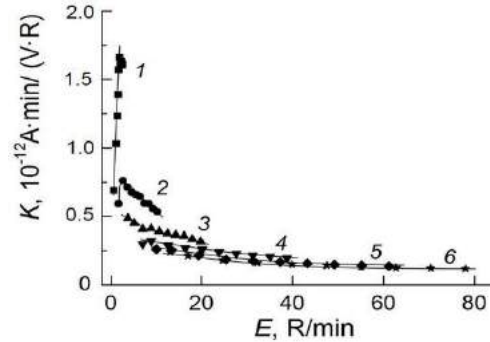


Fig. 2. Dependences of X-ray sensitivity coefficient on irradiation dose rate for AgGaS₂ (CTR method) single crystal ($T = 300$ K and $U = 60$ V) at various accelerating voltages V_a (keV) applied to tube: 25 (1), 30 (2), 35 (3), 40 (4), 45 (5), and 50 (6).

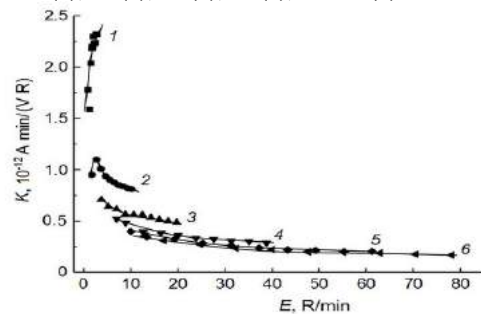


Fig. 3. Dependences of X-ray sensitivity coefficient on irradiation dose rate for AgGaS_{2e} (CTR method) single crystal ($T = 300$ K and $U = 60$ V) at various accelerating voltages V_a (keV) applied to tube: 25 (1), 30 (2), 35 (3), 40 (4), 45 (5), and 50 (6).

Thus, the obtained single crystals can be recommended as active materials for the creation on their basis of uncooled and practically non-inertial X-ray recording devices.

ACKNOWLEDGMENT: Research has been supported by the SDFAR (grant № EIF-BGM-3-BRFTF-2+/2017-15/05/1), (grant № EIF-BGM-4-RFTF-1/2017) and grant № RFFI AzRus 1. «A3_a». 2018.

[1] S.N. Mustafaeva, M.M. Asadov, D.T. Guseinov, X-Ray Dosimetric Properties of Vapor-Grown CdGa₂S₄ Single Crystals // Inorganic Materials. 2010. V. 46. № 6. P. 587-589
 [2] S.N. Mustafaeva, M.M. Asadov, D.T. Guseinov X-Ray Electric Properties of CdIn₂S₄ Monocrystal

// Inorganic Materials: Applied Research. 2010. V. 1. № 4. P. 293-296
 [3] T. Uematsu, T. Doi, T. Torimoto, S. Kuwabata Preparation of Luminescent AgInS₂-AgGaS₂ Solid Solution Nanoparticles and Their Optical Properties // J. Phys. Chem. Lett. 2010. V.1. № 22. P. 3283

INFLUENCE OF FULLERENES C₆₀ ON OPERATING CHARACTERISTICS OF LIQUID CRYSTAL MBBA

T.D. IBRAGIMOV, A.R. IMAMALIYEV, G.F. GANIZADE
Institute of Physics of Azerbaijan National Academy of Sciences,
H. Javid av.131, Baku, AZ 1143, Azerbaijan
tdibragimov@mail.ru

Influence of fullerenes C₆₀ on the threshold voltages of Freederickzs and Carr-Helfrich effects and switching times of the Carr-Helfrich effect in nematic liquid crystal 4-methoxybenzilidene – 4' – butylaniline (MBBA) are presented. It is shown that the clearing temperature and threshold voltage of both effects decreases at the additive of fullerenes. The threshold voltage of electrohydrodynamic instability at low frequencies and also critical frequency of disappearance of Williams' domains decrease. Moreover, the switching times of this effect also decrease. Experimental results are explained by increasing of elastic constant, suppression of conductivity and an increase in numbers of turbulence nucleation at the additive of particles.

Keywords: Liquid crystal; Freedericksz effect; Williams' domain; fullerenes
PACS: 64.70. mj; 64.70. pv; 77.84. Nh; 82.70.Dd.

INTRODUCTION

A series of contributions are devoted to influence of nanoparticles on electrooptic properties of liquid crystals. Particularly, the review on similar researches is resulted in [2]. There is a lot of works on liquid crystalline colloids based on fullerene derivatives, for instance, [3]. But influence of the pure fullerenes on electrooptic parameters of liquid crystals did not practically study.

The results of investigation of Influence of fullerenes C₆₀ on electrooptic properties of liquid crystal 4-methoxybenzilidene – 4' – butylaniline is presented in the report.

EXPERIMENTAL

We used the nematic liquid crystal (LC) 4-methoxybenzilidene – 4' – butylaniline (MBBA) (NIIOPIK, Russia) as a matrix having negative anisotropy of dielectric permittivity. The fullerenes C₆₀ (U.S. Research Nanomaterials, In.) was added into the liquid crystal with 0.5 wt.% and was shaken in a vortex mixer for 1 hour, followed by sonication for 4 hours.

The cell had a sandwich structure and consisted of two plane-parallel glass plates whose inner surfaces were coated with thin transparent and conductive indium-tin-oxide (ITO) layer. The initial configuration of both the LC and the colloid was homeotropic. The cell thickness was fixed with calibrated 20 μm polymer spacers for measurements. Both the colloid and the pure LC were injected into the empty cell by capillary action at the isotropic state.

A set-up for measurements of electro-optical parameters was assembled on the base of the Carl Zeiss polarization microscope. The electric impulses of the special form applied to the cell from the functional generator (model G6-28, Russia). A light, passing through the cell, fell on the photo diode and was registered by digital storage oscilloscope (model 6022BE, Hantek). Switching times were defined from an electro-optic response by application of unipolar rectangular impulses while threshold voltage was defined using unipolar triangular impulses in quasi-static regime. Besides, a value

of the threshold voltage was supervised under the polarization microscope. Frequency dependence of the threshold voltage was registered by application of sinusoidal voltage. All measurements were carried out at temperature 23°C.

RESULTS AND DISCUSSION

Observation under the polarization microscope has shown that the presence of fullerenes in MBBA shifts the clearing point from 42.2°C to 41.6°C. It is qualitatively agreed to following expression from [3] for the spherical form and low concentration of isotropic particles:

$$T_c = (1-f) T_0$$

where f is the volume fraction of particles, T_0 is the clearing temperature of the pure LC.

Besides, it has been shown that the threshold voltage of Freedericksz effect also decreases from 3.7 V to 3,3 V. The threshold voltage at strong coupling is defined as follows [4]:

$$U_{th.F.} = \pi \sqrt{\frac{K_{33}}{\epsilon_0 \Delta \epsilon}}$$

where K_{33} is the bend elastic constant; ϵ_0 is electric constant; $\Delta \epsilon$ is the dielectric anisotropy. Considering numerical values of dielectric anisotropy ($\Delta \epsilon^{LC} = 0.50$; $\Delta \epsilon^{col} = 0.99$ [5]) we may define the bend elastic constant for both the pure LC and the colloid which equals to $6.14 \cdot 10^{12}$ H и $9.68 \cdot 10^{12}$ H, correspondingly. Therefore, there is an increase of elastic constant in the colloid.

The frequency dependence of threshold voltage of Williams's domains formation as the pure LC and the colloid is shown in Fig.1.

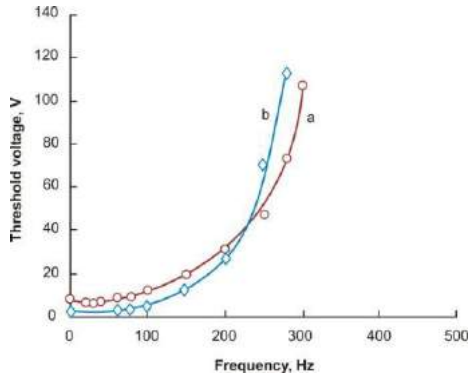


Fig.1. The frequency dependence of the threshold voltage of Williams's domains formation: (a) pure MBBA, (b) MBBA + fullerenes.

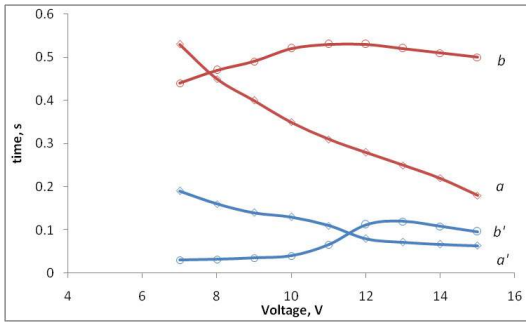


Fig.2. Voltage dependence of switching times: (a) a rise time of the pure MBBA, (a') a rise time of the colloid, (b) a decay time of the pure MBBA, (b') a decay time of the colloid.

Apparently, the threshold voltage of Williams's domains formation for the colloid is less than for the pure LC at low frequencies. Obviously, it is connected with an increase in numbers of turbulence nucleation at the additive

of particles. The critical frequency of disappearance of Williams's domains in the colloid is also less. It is connected with conductivity reduction in the colloid [5].

The results of measurements of switching times for hydrodynamic instability (Williams's domains formation) of the pure LC and the colloid depending on the applied voltage are resulted in Fig.2.

Apparently, the additive of particles reduces both a rise time and a decay time that, basically, is connected with an increase in dielectric anisotropy and reduction of the threshold voltage. Actually, a rise time for the Carr-Helfrich effect is defined by following expressions [6]:

$$\tau_{on} = \frac{\beta \eta d^2}{U^2 - U_{th}^2}$$

where η is the translational viscosity, β is the parameter depending on material properties of the substance such as elastic constants and density, d is the cell thickness, U is the applied voltage. One can calculate the rotational viscosity for both samples. These calculations show that the viscosity increases at the additive of fullerenes.

As can be also seen from this Fig. 2, a decay time also decreases at present of fullerenes. In accordance with [6,7], a decay time is defined by following expressions:

$$\tau_{off} = \frac{\alpha \eta d^2}{\pi^2 K_{33}}$$

It is obvious that decreasing of decay time is connected with increasing in an elastic constant.

In summary, the additive of fullerenes in MBBA improves the operating characteristics of liquid crystal MBBA, namely, decreases the threshold voltages and switching times in the Carr-Helfrich effect.

-
- [1] Liquid crystals with nano and microparticles, edited by *Jan P. F. Lagerwall and Giusy Scalia*, Singapore, World Scientific, 2017, v.2, 920 p.
 - [2] *N. V. Kamanina*. Fullerene-dispersed nematic liquid crystal structures: dynamic characteristics and self-organization processes, *Physics – Uspekhi*, 2005, v. 48, No4, pp. 419 - 427
 - [3] *F. Haragushi, K. Inoue, N. Toshima et al.*, Reduction of the threshold voltages of nematic liquid crystal electrooptical devices by doping inorganic nanoparticles, *Japanese Journal Applied Physics*, 2007, v. 46, pp. L796-L797
 - [4] *T.D. Ibragimov, G.M. Bayramov, A.R. Imamaliyev*. Design and electro-optic behavior of novel polymer - liquid crystalline composites, *Journal of Molecular Liquids*, 2016, v. 221, pp. 1151–1154
 - [5] *T.D. Ibragimov, F.R. Imamaliyev, G.F. Ganizade*, Influence of fullerenes on dielectric and conductivity properties of liquid crystal MBBA. *Azerbaijan Journal of Physics*, 2018, No2 (in Press)
 - [6] *T.D. Ibragimov, A.R. Imamaliyev, G.M. Bayramov*, Influence of barium titanate particles on electro-optic characteristics of liquid crystalline mixture H37, *Optik*, 2016, v.127, pp. 1217–1220
 - [7] *T.D. Ibragimov, G.M. Bayramov*, Influence of small particles on Carr–Helfrich electrohydrodynamic instability in the liquid crystal, *Optik*, 2013, v. 124, pp.3004-3006

DE SITTER COSMOLOGICAL MODEL AND THE PROBLEM OF DARK MATTER AND ENERGY

B.A. RAJABOV

N. Tusi Shamakhi Astrophysics Observatory,
Azerbaijan National Academy of Sciences
balaali.rajabov@mail.ru

It is shown that after contraction of unitary irreducible representations of the de Sitter group SO (4,1), a direct sum of unitary irreducible representations of the Poincaré group with different signs of the rest mass is obtained. This result is used to interpret the phenomena of "dark matter" and "dark energy" in terms of Wigner's elementary quantum systems in the de Sitter world.

Keywords: de Sitter world, SO(4,1) group, Wigner-Inönü limit, "dark matter", "dark energy", contraction, elementary systems.

1. INTRODUCTION

Recently, the nature of dark matter and dark energy has been intensively studied, and various assumptions about their composition are being considered, [1].

In this paper, we propose an explanation of these phenomena by the Wigner's elementary systems in the de Sitter world, [2].

2. WIGNER'S THEORY OF ELEMENTARY SYSTEMS

A real understanding of the nature of the spin and mass of elementary particles appeared after the classical work of E. Wigner on the representations of the inhomogeneous Lorentz group (that is, the Poincaré group), [3]. He studied the projective representation of this group in the Hilbert space of states of a quantum system and introduced the concept of an elementary system and showed that such systems correspond to irreducible representations. Moreover, Wigner proved that the rest mass and the spin of an elementary particle are invariants that uniquely characterize irreducible representations of the Poincaré group.

Invariants of the inhomogeneous Poincaré group are constructed using translation generators P_μ and 4-dimensional rotations $M_{\mu\nu}$ as follows, [4]:

$$m^2 = P_\mu P^\mu, \quad w^2 = w_\mu w^\mu = m^2 s(s + 1) \tag{1}$$

$$w_\rho = \frac{1}{2} \epsilon_{\lambda\mu\nu\rho} P^\lambda M^{\mu\nu}$$

where m - mass, s - spin of the particle, and w_ρ is the Pauli-Lubansky-Bargmann vector.

Important! In the case $m^2 > 0$, there is a third invariant - the sign of energy:

$$\varepsilon = \frac{P_0}{|P_0|} = \pm 1.$$

3. EINSTEIN'S EQUATIONS AND DE SITTER'S SOLUTIONS

According to general relativity theory, the Einstein equations in the vacuum, take the form, [5]:

$$R_{\mu\nu} = \Lambda g_{\mu\nu} \tag{2}$$

where $R_{\mu\nu}$ - Ricci tensor, $g_{\mu\nu}$ - metric tensor, Λ - cosmological constant (the values of Λ are permanently refined with the accumulation of observations: $\Lambda \sim 10^{-53} m^2$, 1998).

It is known that general solutions of Einstein's equations do not have a group of motions. But in 1917 Willem de Sitter found two solutions of (2) for $\Lambda \neq 0$ that allow 10-parameter groups of motions, which are the maximal groups of motions of Einstein spaces, [5]:

$$ds^2 = \frac{dr^2}{1-r^2/R^2} + r^2(d\vartheta^2 + \sin^2\vartheta d\varphi^2) - (1 - r^2/R^2)c^2 dt^2, \quad \text{if } \Lambda > 0, \tag{3}$$

$$ds^2 = \frac{dr^2}{1 + r^2/R^2} + r^2(d\vartheta^2 + \sin^2\vartheta d\varphi^2) - (1 + r^2/R^2)c^2 dt^2, \quad \text{if } \Lambda < 0. \tag{4}$$

$$\Lambda = \pm \frac{3}{R^2}$$

where R – radius of curvature of space.

These spaces have global symmetry groups SO(4,1) and SO(3,2) that leave the metrics (3)-(4) invariant. Spaces (3)-(4) are called de Sitter worlds of the 1st and 2nd kind or de Sitter worlds DS and anti-de Sitter AdS.

We restrict ourselves to the de Sitter world (3) and the SO(4,1) group. The case of the anti-de Sitter world will be considered in a separate paper, because of the difficulties in interpreting the space-time measurements.

The commutation relations for the generators of the group SO(4,1) have the form:

$$[M_{\mu\nu}, M_{\rho\sigma}] = i(g_{\mu\rho}M_{\nu\sigma} - g_{\mu\sigma}M_{\nu\rho} - g_{\nu\rho}M_{\mu\sigma} + g_{\nu\sigma}M_{\mu\rho}),$$

$$[M_{\mu\nu}, P_\rho] = i(g_{\mu\rho}P_\nu - g_{\nu\rho}P_\mu), \quad [P_\mu, P_\nu] = \frac{i}{R^2} M_{\mu\nu}, \quad P_\mu = \frac{1}{R} M_{4\mu}$$

The Casimir operators of the Lie algebra of the group $SO(4,1)$ have the following form, [4]:

$$C_1 = \frac{1}{2R^2} M_{ab} M^{ab} = -P_\lambda P^\lambda - \frac{1}{2R^2} M_{\mu\nu} M^{\mu\nu} = M^2,$$

$$C_2 = -W_a W^a, \quad W_a = \frac{1}{8R} \epsilon_{abcde} M^{bc} M^{de}$$

When $R \rightarrow \infty$ the Lie algebra of the group $SO(4,1)$ becomes over to the Lie algebra of the Poincaré group, and the Casimir operators become:

$$C_1 \rightarrow m^2, \quad C_2 \rightarrow m^2 s(s+1),$$

where m, s - spin and rest mass, respectively (this limiting transition corresponds to the well-known Wigner-Inönü contraction, [6]).

From the limiting transition of the Casimir operators C_1, C_2 it follows that unlike the Minkowski world in the de Sitter world, elementary systems are identified not by mass and spin, but by some functions of spin and mass.

In particular, non-degenerate representations of the group $SO(4,1)$ can be realized in the space of $2s+1$ -component vector-functions and the degree of homogeneity of σ on the upper field of the cone, [7].

Then the parameters σ, s will play the role of invariants characterizing the irreducible representations of the group $SO(4,1)$. In addition, after the operation of contraction, the parameter s becomes into spin and the σ to the function of mass m .

The basis for our assumption about the nature of dark matter and energy is the following theorem on the contraction of representations of the de Sitter group $SO(4,1)$ to the representations of the Poincaré group $ISO(3,1)$.

Theorem. The result of the contraction of the UIR's $T^{(\sigma,s)}(g), g \in SO(4,1), \sigma = -3/2 + imR$, for $R \rightarrow \infty$ is the direct sum of UIR, $U^{(m,s,\varepsilon)}(g), g \in ISO(3,1)$ with mass σ, s and differing in energy sign ε .

Proof. The proof of the theorem is given in the article [8].

CONCLUSION

In the flat world of Minkowski, Wigner's elementary systems are determined by the rest mass, the spin and the

sign of their energy can be identified with elementary particles. The considerations about the stability of physical systems require to limit the energy spectrum from below and to exclude negative energies.

In the de Sitter world, elementary Wigner systems are identified by spin and by a parameter, which is the flat limit of a function of spin and mass, with different energy signs. But unlike the Minkowski world, we cannot exclude negative energies from consideration.

That is, elementary systems on a cosmological scale can be in states with positive and negative energies. Elementary systems in a state with positive energy behave like a gravitating mass, and in a negative energy state as an anti-gravity mass.

And so, our final conclusions are as follows:

1. Mysterious "dark matter" and "dark energy" consist of such elementary systems.
2. "Dark matter" and "dark energy" are the first manifestations of quantum properties on the scale of the universe. Until now, quantum phenomena have been encountered in the micro-world, and also as macroscopic quantum effects in the theory of condensed matter.
3. "Dark matter" and "dark energy" are carriers of information about the first moments of the universe after the Big Bang.

The last conclusion follows from the fact that according to the standard cosmological model, the de Sitter world is a necessary phase of the evolution of the universe in the first instants ($10^{-34} - 10^{-32}$ seconds) after the Big Bang.

Of course, our universe is not de Sitter's world, although according to some data it is developing in the direction of this model. Considering the given phenomena of dark matter and dark energy in the general case is a difficult task because today there is no quantum theory of gravity. The solution of this problem in general for the gravitational field requires not only new physical concepts but also new mathematics. The main results of this work were reported in the 3rd International Scientific Conference "Modern Problems of Astrophysics-III", September 25-27, 2017, Georgia.

-
- | | |
|---|--|
| <p>[1] New Ideas in Dark Matter 2017, arXiv: 1707.0459v1 [hep-oh], 2017, p.113</p> <p>[2] B.A. Rajabov, arXiv:1801.10004, (2018), p.12</p> <p>[3] E. Wigner, On unitary representations of the inhomogeneous Lorentz group, Nuclear Physics B (Proc.Suppl.), 6, (1989), 9-64; Ann. Math., 40, 149 (1939)</p> <p>[4] F. Gürsey, Introduction to Group Theory, in "Relativity, Groups and Topology", eds. C. DeWitt, B. DeWitt, New York-London, 1964</p> | <p>[5] S. Weinberg, Gravitation and Cosmology, John Wiley and Sons, Inc., New York-London-Sydney-Toronto, 1972</p> <p>[6] Wigner-Inönü, Proc. Nat. Acad. Sci. (USA), 39, 510, 1953; 40, 119 (1954)</p> <p>[7] B.A. Rajabov, Trans. Nat. Acad. Sci., Azerbaijan, series of phys.-math. sciences, No.6, (1983), pp.58-63 (in Russian)</p> <p>[8] B.A. Rajabov, The contraction of the representations of the group $SO(4,1)$ and cosmological interpretation, Astronomy& Astrophysics (Caucasus), 3, (2018), pp.74-90</p> |
|---|--|

NEW ELECTROMAGNETIC METHODS OF SLOWDOWN AND TRAPPING OF PARTICLES

AZAD Ch. IZMAILOV

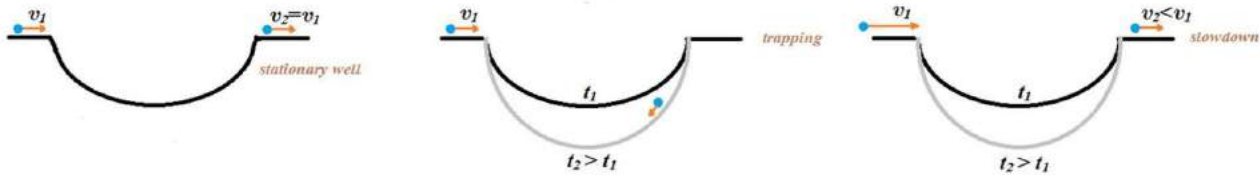
*Institute of Physics, Azerbaijan National Academy of Sciences, Javid av. 131,
Baku, Az-1143, AZERBAIJAN
azizm57@rambler.ru*

Electromagnetic “cooling” and localization of microparticles (in particular, atoms and molecules) under conditions of the high vacuum are very important for a number of directions of physics and technologies including quantum information, ultra-high-resolution spectroscopy, and optomechanics of such particles.

I have proposed sufficiently simple methods for the slowdown and trapping of various microparticles (including atoms and molecules) by means of external electromagnetic fields which induce (for such particles) potential wells having fixed spatial distributions but deepening over time up to some limit. It is assumed that considered particles are under conditions of the high vacuum and forces acting on these particles are not dissipative, that is they move without friction. Depending on whether the particles have electric (magnetic) moment, it is possible to use the controllable electric (magnetic) field or far-off-resonance laser radiation for inducing of corresponding potential wells for given particles.

In the present work, I theoretically demonstrate possible applications of proposed methods for “cooling” and localization of particles for a number of nonstationary electromagnetic potential wells with different fixed spatial configurations. In particular, optomechanics of levitated particles by various far-off-resonance laser beams, amplifying over time (up to some limit), is analyzed. New schemes of traps and decelerators of polarizable particles, based on corresponding nonstationary gradient forces, are considered.

Proposed “cooling” and trapping methods may be applied in definite cases also for atoms and molecules in the ground quantum state. Realization of such methods for atoms and molecules is important for applications in ultra-high-resolution spectroscopy, precision frequency standards and in quantum computing processes.



Motion of classical particles without friction in a potential well deepening over time

BASIC RELATIONSHIPS

We will consider problems which may be solved on the basis of classical mechanics and electrodynamics. Let us assume that a point particle with the mass m freely moving in a three-dimensional space before its entering to the region V of the potential well $U(R, t)$, which explicitly depends not only on the coordinate R but also on time t . The total energy of such a particle with the non-relativistic velocity v is described by the known formula:

$$E(R, v, t) = 0.5mv^2 + U(R, t) \tag{1}$$

Further we will consider the potential energy $U(R, t)$ of the following type:

$$U(R, t) = s(R) * \varphi(t) \tag{2}$$

where the coordinate function $s(R) \leq 0$ in the region V , and $\varphi(t) \geq 0$ is nondecreasing function of time t .

Such a potential (2) may be created for particles having electric or magnetic moment by a controllable electromagnetic field with the growing strength (up to a certain time moment) but with a fixed spatial distribution. We have the following motion equation of the particle in case of the potential energy (2):

$$m \frac{d^2R}{dt^2} = -\varphi(t) \frac{ds(R)}{dR} \tag{3}$$

From relations (1)-(3) we directly receive the formula for the time derivative of the total energy $E(R, v, t)$ of the particle:

$$\frac{dE}{dt} = s(R) \frac{d\varphi(t)}{dt} \leq 0. \tag{4}$$

According to inequality (4), increase of the function $\varphi(t)$ with time t leads to decrease of the total energy $E(R, v, t)$ (1) of the particle in the region V of the potential well, where the coordinate function $s(R) \leq 0$.

We see from formula (1) that the particle cannot go beyond the potential well and reach the region with $U(R, t) = 0$, when its total energy E will be negative. It is important to note, that under such a condition $E < 0$, the considered classical particle will be localized in the region V of the potential well even after output of the nondecreasing time function $\varphi(t)$ on a constant value.

At the same time, a sufficiently fast particle overcomes such potential wells in spite of their deepening over time. However, according to formulas (1) and (4), kinetic energy of this particle decreases at transits of such wells between space regions where the particle potential energy $U(r, t) = 0$.

Further we will analyze trapping and slowdown of considered classical particles by a spatially inhomogeneous electromagnetic radiation with intensity increasing over time up to a certain limit. In so doing, it is assumed that the radiation pressure exerted on particles by such a radiation is small compared to the light induced gradient force acting upon them. This is possible for

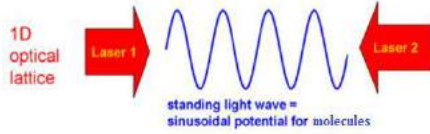
particles that are nearly transparent in the spectral range of their irradiation. We will analyze not too strong radiation, for which the induced electric dipole moment of the particle is proportional to the electric field strength, while the potential energy of the particle is proportional to the electric field squared.

TRAPPING OF PARTICLES BY LASER FIELDS AMPLIFYING OVER TIME

Let us analyze the possible (for practical realization) case of the amplifying with time standing light wave (along the axis z) whose intensity has the transversal Gaussian distribution. Such a radiation creates the potential well of the type $U(R,t) = s(R) * \varphi(t)$ (2) with the following coordinate function $s(R)$ for particles with light induced dipole moments:

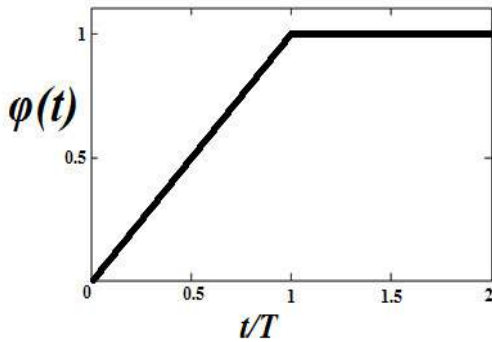
$$s(R) = -J_0 * \exp(-r^2/r_0^2) * \sin^2(kz), \quad (5)$$

where $r = \sqrt{x^2 + y^2}$ is the distance from the central axis of the light beam (with the characteristic radius r_0), k is the wave number, and $J_0 > 0$ is the value with the dimension of energy, which is determined by a polarizability of a particle.



For example, we will consider the following time dependence $\varphi(t)$ (2) for the radiation intensity:

$$\varphi(t) = (t/T) * \eta(T - t) + \eta(t - T), \quad (t \geq 0), \quad (6)$$



where $\eta(q)$ is the step function ($\eta(q) = 1$ if $q \geq 0$ and $\eta(q) = 0$ when $q < 0$). The function $\varphi(t)$ (6) linearly increases from 0 to 1 in the interval $0 \leq t \leq T$ and is equal to unit, when $t > T$.

Fig.1, a present numerically calculated (on the basis of the motion equation (3)), temporary dependences of the distance $r(t)$ from the axis of the light beam and longitudinal coordinate $z(t)$ of the particle, which approaches from the outside to the given beam at starting conditions specified in the moment $t_0=0$. We see, that during increasing of the radiation intensity with time t (6), trapping and three-dimensional localization of the considered particle occurs in the region of the beam which, according to the function $s(R)$ (5), creates the spatially

periodic potential along the axis z . In this case the particle carries out vibration transversal motions $r(t)$ in limits determined by the characteristic radius r_0 of the light beam (Fig.1, a) and also undergoes comparatively fast nondamped oscillations $z(t)$ in the longitudinal direction in the limit of the half wavelength $\lambda = 2\pi/k \ll r_0$ of the radiation (Fig.2).

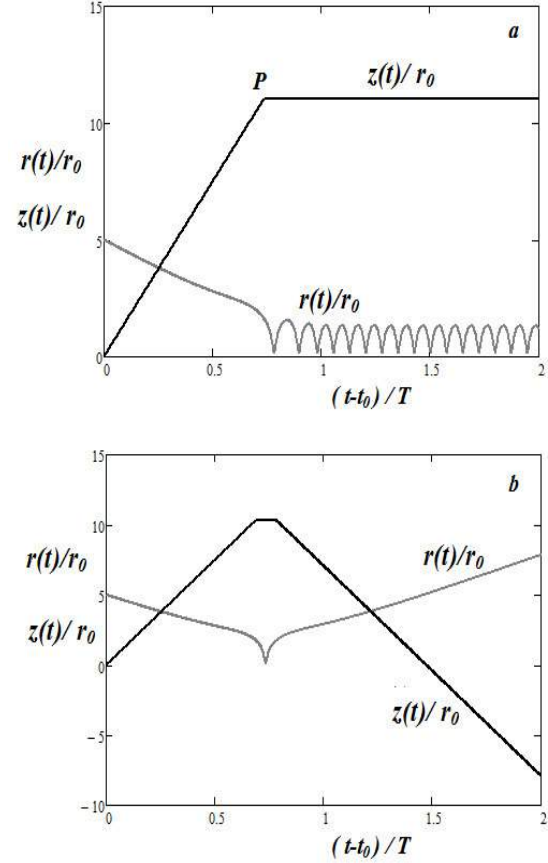


Fig.1. Dependences of particle coordinates $r(t) = \sqrt{x(t)^2 + y(t)^2}$ and $z(t)$ on time $t \geq t_0$ at particle initial coordinates $x(t_0)=0, y(t_0) = 5r_0, z(t_0)=0$ and its initial velocity components $v_x(t_0) = -2.5(r_0/T), v_y(t_0) = -5(r_0/T), v_z(t_0) = 15(r_0/T)$, given in moments $t_0 = 0$ (a) and $t_0 > T$ (b), when $J_0 = 5000m(r_0/T)^2$ and $kr_0=1000$.

The given particle remains localized in such a potential well even if $(t - t_0) > T$ (Fig.1, a), that is after the output of the radiation intensity on the constant value according to formula (6). One can see from comparison of Fig.1,a and dependence 1 in Fig.3 that trapping of this particle occurs when its total energy $E(t)$ (1) decreases up to negative values because of the inequality (4).

Fig.1, b presents dynamics of a particle with the same initial values of velocity and coordinates as in Fig.1, a but specified in a moment $t_0 > T$. Then, according to the dependence (6), the given particle flies through the stationary light beam, whose intensity is equal to the maximum value for the considered case of Fig.1,a. We see that this particle is not captured by the light beam and moves away from it after the primary rapprochement (Fig.1,b). The total energy $E(t)$ (1) of the given particle is constant during the whole its movement (dependence 2 in Fig.3).

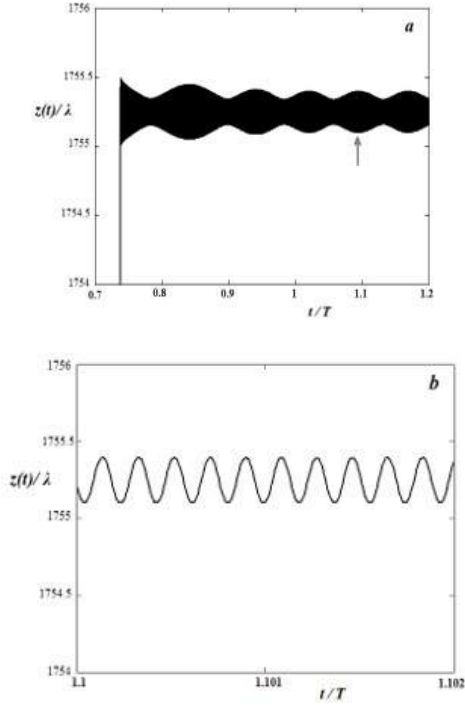


Fig.2. Particle coordinate $z(t)$ (in units of the radiation wavelength $\lambda = 2\pi/k$) versus time t in enlarged scales in the neighborhood of the point P from fig.1,a. Fig. 2,b presents the dependence $z(t)$ in the narrow region indicated by the arrow in fig. 2,a.

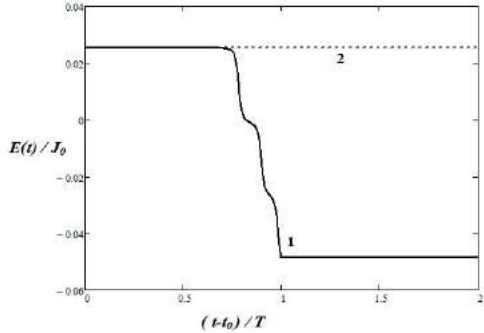
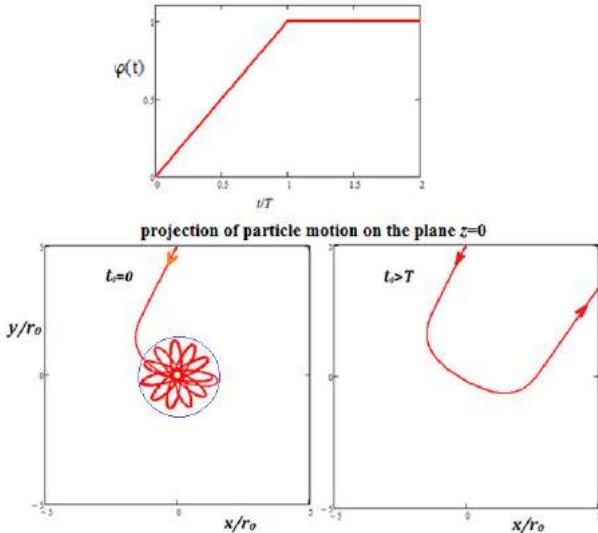


Fig.3. The total energy $E(t)$ (in units $J_0 = 5000 \cdot m \cdot r_0^2 / T^2$) versus time $t \geq t_0$. Curves 1 and 2 were calculated respectively for parameters of fig.1,a and fig.1,b.

VISUAL DEMONSTRATION OF DISCUSSED TRAPPING PROCESS



I have carried out numerical calculations also for a number of other potential wells with cylindrical and spherical symmetries described by the general formula $U(R, t) = s(R) * \varphi(t)$. These calculations confirmed following qualitative results (a), (b) and (c) of the present work:

- (a) Even a highly shallow but increasing with time potential well may continuously capture sufficiently slow-speed particles flying through it.
- (b) Such trapped particles will remain in this potential well even after going out of a nondecreasing strength of the corresponding electromagnetic field on stationary values. However, such a stationary trap already will not capture new particles.
- (c) Since considered electromagnetic traps are based on non-dissipative forces, then particles, captured in given traps, carry out non-damped oscillation motions in limits of corresponding potential wells.

SLOWDOWN OF PARTICLES BY LASER FIELDS AMPLIFYING OVER TIME

Now we will analyze the case of a running (along the axis z) light beam, the intensity of which increases over time and is characterized by the Gaussian transverse intensity distribution. For particles with induced dipole moment, this radiation creates a potential well of the type $U(R, t) = s(R) * \varphi(t)$ with the coordinate function $s(R)$ of the form:

$$s(R) = -P_0 * \exp(-r^2/r_0^2), \quad (7)$$

where $r = \sqrt{x^2 + y^2}$ is the distance from the beam central axis (r_0 is the characteristic beam radius), $P_0 > 0$ is a constant quantity with the dimension of energy that is determined by a particle polarizability.

For example, let us consider the following time dependence $\varphi(t)$ (2) for the beam intensity:

$$\varphi(t) = 1 - \exp\left(\frac{-t}{\tau}\right), \quad (t \geq 0), \quad (8)$$

where τ is a characteristic time interval? Function $\varphi(t)$ (8) increases with time from 0 to 1 and asymptotically approaches to 1 when $t \gg \tau$.

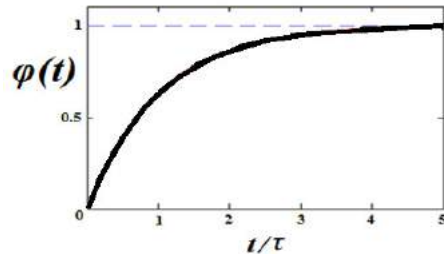


Fig.4a demonstrates numerically calculated, on the basis of motion equations (3), dependence of the modulus of the particle velocity v on time t at initial conditions specified in a moment t_0 . The situation is considered, when such particles in this moment t_0 are located outside of the region where the light beam (7) can exert sufficient influence on them. In case $t_0 = 0$, particles with the speed $v_0 = v(t_0)$ transit through the laser beam (7) during

increasing of its intensity according to the time dependence $\varphi(t)$ (8). Then, at first the sharp increase of the particle speed takes place because of its getting into the light induced potential well (curve 1 in Fig.4a). However, after the passage of such a deepening over time well, the particle speed goes to the constant final value v_f , which is about 35% lower than its initial value v_0 .

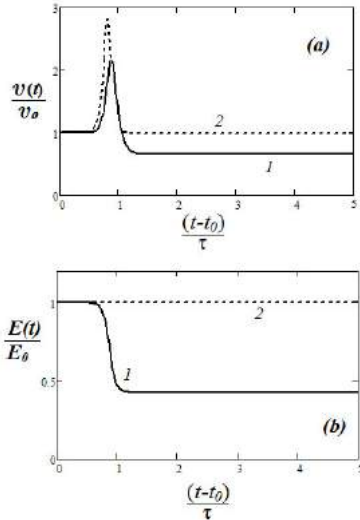


Fig.4. Dependence of the particle velocity modulus v (a) and its total energy E (b) on time t at following initial coordinates of this particle $x(t_0)=0$, $y(t_0)=5r_0$, $z(t_0)=0$ and its velocity components $v_x(t_0)=0.5(r_0/\tau)$, $v_y(t_0)=-5(r_0/\tau)$ and $v_z(t_0)=1.5(r_0/\tau)$, specified in the moment $t_0=0$ (curves 1) and $t_0 \gg \tau$ (curves 2) for the function $\varphi(t)$ (6), when $P_0=100m(r_0/\tau)^2$, $v_0=v(t_0)=\sqrt{v_x(t_0)^2+v_y(t_0)^2+v_z(t_0)^2}$ and $E_0=E(t_0)$.

According to the formula (4), this process is accompanied by decrease of the particle total energy (curve 1 in Fig.4b).

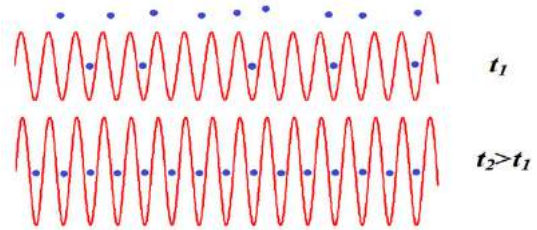
Curves 2 in Fig.1 correspond to a particle with the same initial values of velocity and coordinates as for considered above curves 1, but specified in a time moment $t_0 \gg \tau$. Then, according to the time dependence (8), such a particle initially transits through the stationary light beam whose intensity already reaches a maximum value. In this case the final particle speed v_f is equal to its initial value v_0 and the total energy of the particle is constant during all process of particle transit through such a stationary potential well (curves 2 in Figs.4a and 4b).

POSSIBLE APPLICATIONS

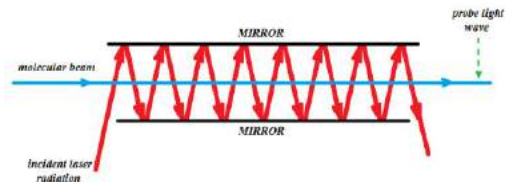
We have considered structureless classical particles in potential wells of the certain type

$U(R, t) = s(R) * \varphi(t)$. In practice it is possible, for example, for a collection of noninteracting (with each other) microparticles, which fly without friction under conditions of the ultrahigh vacuum at action of the controllable electric (magnetic) fields or nonresonance laser radiation with fixed spatial configurations.

For analysis of possible trapping and slowdown of atoms and molecules by electromagnetic potential wells, consideration of their quantum structure is necessary. At the same time, results obtained in this work may be applied also for such atomic objects in definite cases. Thus, for example, it is possible creation of traps for atoms and molecules by a nonhomogeneous laser radiation with frequencies essentially detuned from resonances with atomic (molecular) transitions. Then the gradient force acts on atoms (molecules), which are in the ground quantum state, in the direction to the point of minimum of the light induced potential well. In particular, such wells may be induced also by laser beams considered in the present work. However, as was shown above, even highly slow-speed microparticles, flying from outside through such stationary beams, will not be captured in corresponding potential wells. At the same time, proposed intensification of the laser radiation (during a certain time interval) will lead to large increase of a number of particles captured in given traps.



It is necessary to note, that existing methods for slowdown of atoms by means of resonance laser radiation are inefficient for molecules because of their relatively complex quantum level structure. At the same time, the slowdown mechanism of particles by nonresonance light beams demonstrated in the present work is applicable also for cooling of ensembles of molecules in the ground quantum state. Therefore, in the future, development of corresponding effective decelerators of molecules under conditions of ultra-high vacuum will be important on the basis of search of optimal spatial configurations and amplification dynamics of nonresonance laser radiation.



Scheme of possible molecules decelerator on the basis of nonresonant laser radiation amplifying over time.

This work is the continuation of research carried out by author in following recent papers:

- [1] A.Ch. Izmailov "Trapping of classical particles by an electromagnetic potential well deepening over time", Optics and Spectroscopy, 2015, V. 119, N5, pages 883-886 (see also arXiv:1503.01076, March 2015)
- [2] A.Ch. Izmailov "On motion control of microparticles by an electromagnetic field amplifying over time for spectroscopy problems", Optics and Spectroscopy, 2017, V. 122, N2, pages 315-321 (see also arXiv: 1604.07345, April 2016)

SYNTHESIS AND PHOTOLUMINESCENT PROPERTIES OF IODINATED MULTI WALLED CARBON NANOTUBES

S. H. ABDULLAYEVA^{1,2}, S.A. MAMMADOVA¹, A.B. HUSEYNOV², A.O. ISRAFILOV²

1. Institute of Physics named after G. M. Abdullayev, Azerbaijan National Academy of Sciences

2. High Tech Research Center under the Ministry of Transport, Communications and High

Technologies of the Republic of Azerbaijan

samiras416@gmail.com

This paper reports synthesis and photoluminescent properties of iodinated multi-walled carbon nanotubes (I-MWCNTs). MWCNTs were synthesized by Aerosol-Chemical Vapor Deposition method (A-CVD) and iodinated by crystalline iodine under increased pressure (approximately ~ 20 bar) at 400^o C. X-Ray Diffraction (XRD) and Raman spectroscopy analysis proved the presence of iodine atoms in I-MWCNTs. After iodination, the concentration of introduced iodine atoms constitute approximately 30% in weight. Photoluminescence (PL) intensity of the I-MWCNTs remarkably enhanced by the introduction of iodine atoms and explained with defects, due to the formed covalent C - I bonds over the MWCNTs which can play the role of luminescence centres in I-MWCNTs. I-MWCNTs show a wide emission spectrum with two emission peaks (430nm, 520nm). For the first time the intensity of these peaks was highly increased due to the effective iodination of MWCNTs by our group.

Keywords: A-CVD, Iodinated Multi Walled Carbon Nanotubes, Photoluminescence, XRD, Raman spectroscopy

PACS: 78.67.Ch, 73.22.-f, 81.07

1. INTRODUCTION.

The visible luminescence of the functionalized carbon nanotubes in solution firstly discovered by Riggs [1]. Later, this was confirmed by another studies in literature [2-4]. The low toxicity and photoluminescent properties of carbon nanotubes makes this material very useful in the field of photonics and for large scale optoelectronic applications. Only a few studies have investigated the photoluminescent properties of iodinated MWCNTs [5-7]. This motivated us to prepare I-MWCNTs and investigate their photoluminescent properties.

2. EXPERIMENTAL SECTION

Pristine MWCNTs were synthesized by an Aerosol - Chemical Vapor Deposition method (A-CVD) on the experimental laboratory setup (Scientific Instruments Dresden GMBH, SCIDRE, Germany). Cyclohexane (Cy) was used as a source of carbon and ferrocene (Fc) as a catalyst precursor [8]. Synthesis process was carried out at 9000C temperature at atmospheric pressure.

Iodination of MWCNTs were prepared in a sealed quartz ampoule under increased pressure (approximately ~ 20 bar) at 400^oC for 2 hours. The obtained product was washed in ethanol until the absorbed iodine completely disappeared and dried at 120 ^oC temperature.

The iodinated MWCNTs were characterized by Raman spectroscopy and XRD. Raman scattering measurements were performed in a wide wavenumber range between 500 and 9000 cm⁻¹ by Nanofinder 30 Confocal Laser Microspectrometer method operating at 532 nm laser line (Laser power 8mW, a 100 grooves/mm grating, exposure time 10s).

X-ray diffraction patterns were recorded using a Bruker 5000 diffractometer in standard (θ -2 θ) geometry using Cu K α radiation.

Photoluminescence (PL) measurements of I-MWCNTs / ethanol suspension in the 350-700 nm regions

were obtained upon excitation with the 325 nm lines of an IK series He-Cd laser.

3. RESULTS AND DISCUSSIONS

3.1 X-RAY DIFFRACTION ANALYSIS

XRD studies were performed on iodinated MWCNTs and shown in Fig. 1. It is clear from the XRD analysis that the main peaks at 26^o (002), 43^o (100) and 53.2^o (004) shows good consistence to the data from the standard CNTs diffraction file (PDF 00-058-1638) and proves high crystallinity of MWCNTs.

Moreover, XRD spectra proves the presence of covalent C- I bonds over the carbon nanotubes and small amount of absorbed iodine atoms into the pores of MWCNTs.

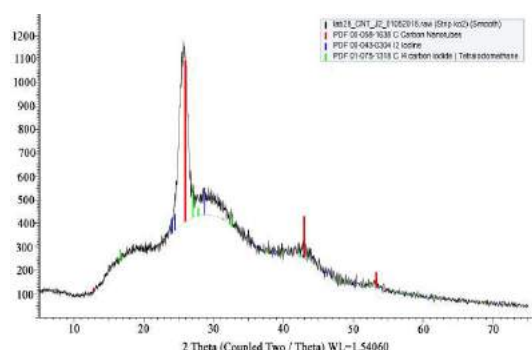


Fig.1. XRD patterns of pristine and I-MWCNTs

3.2 RAMAN SPECTROSCOPY

Raman spectra of both, pristine and I-MWCNTs were recorded using 532 nm exciting line. The Raman spectra of pristine and I-MWCNTs exhibits similar characteristic peaks (fig.2).

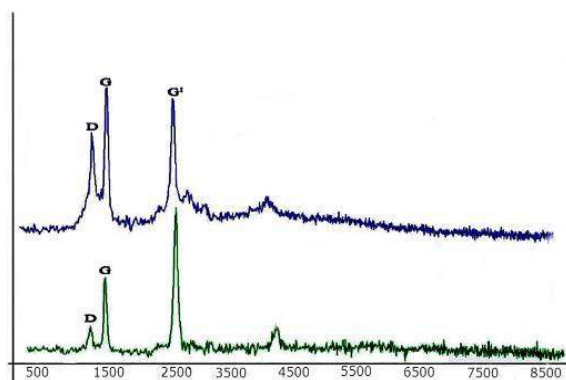


Fig.2. Raman spectra of pristine MWCNTs (green line) and I-MWCNTs (blue line)

The main exception is that for I-MWCNTs the D band intensity at approximately (1300cm^{-1}) significantly increases compared to the pristine MWCNTs. After iodination, a large number of C-I bonds were formed over the MWCNTs surface, due to the interaction large amount of iodine atoms (30% wt). The increase of the D/G ratio implies that more sp^2 -hybridized carbons are converted to sp^3 -hybridized carbons and form defects. It is assumed that these defects play the role of luminescent centers.

3.3. UV-VIS PHOTOLUMINESCENCE PROPERTIES OF IODINATED MWCNTS

Photoluminescence emission spectra of the pristine and I-MWCNTs suspension in ethanol are reported in Fig. 3. Experiments were carried out with the 325 nm laser excitation of samples in the 300-700 nm region. As shown in Fig. 3, I-MWCNTs have a wide emission spectrum with two emission peaks (430nm, 520nm).

The enhancement of peaks can be explained with distribution of nonequivalent emission sites due to the dispersion of the defects with iodination of MWCNTs. The C-I bonds can form defects which can play the role of luminescent centers in I-MWCNTs.

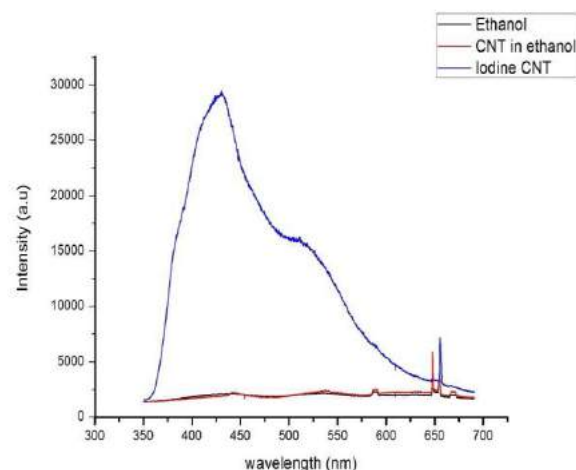


Fig. 3. Photoluminescence (PL) spectra of ethanol (black line), pristine MWCNT /ethanol (red line) and I-MWCNTs /ethanol (blue line) suspension

CONCLUSIONS

MWCNTs were synthesized by A-CVD method at 900°C and iodinated with a simple chemical route in a sealed quartz ampoule at 400°C for 3 hours. In comparison with other authors, our group firstly obtained functionalized carbon nanotubes with iodine content of 30 wt%. XRD analysis have shown the presence of iodine phases on spectrum and Raman spectroscopy revealed the enhancement of defect band in iodinated MWCNTs. I-MWCNTs suspension in ethanol exhibits emission spectrum with two intense peaks at blue (430 nm) and green (520 nm) regions. For the first time the intensity of these peaks was highly increased which is explained with defects that formed due to the C-I chemical covalent bonds (which play the role of luminescent centers for I-MWCNTs) after incorporation of iodine atoms.

-
- [1] J.E. Riggs, Z.L. Guo, D. Carroll, Y.P. Sun // J. Am. Chem. Soc. 2000. V. 122. P. 5879
- [2] L. Minati, G. Speranza, I. Bernagozzi, S. Torrenzo et.al. // Diamond and Related Materials. 2011. V. 20. P.1046
- [3] O. Kozak, M. Sudolská, G. Pramanik, P. Cígler et al. // Chemistry of Materials. 2016. V. 28. P. 4085
- [4] S. Yaragalla, G. Anilkumar, N. Kalarikkal, S. Thomas //Materials Science in Semiconductor Processing. 2016. V. 41. P. 491
- [5] Zh. Qian, J. Ma, J. Zhou, P. Lin // J. Mater. Chem. 2012. V.22.P. 22113
- [6] W.Y. Zhou et al. // Appl. Phys. Lett. 2002.V.80. P.2553
- [7] J. Zhou, P. Lin, Ma J., X. Shan et all. // RSC Adv. 2013. V.3 P. 9625
- [8] S.H. Abdullayeva, S.A. Mammadova, M. Huseynova B., Huseynov A. B. et all. // Azerbaijan Journal of Physics. 2017. V.3. P. 31

NEUTRON DIFFRACTION STUDY OF As_40Se_60 , $\text{As}_40\text{Se}_30\text{S}_30$, $\text{As}_40\text{Se}_30\text{Te}_30$ CHALCOGENIDE GLASSES

R.I. ALEKBEROV¹, A.I. ISAYEV¹, S.I. MEKHTIYEVA¹, M. FÁBIÁN^{2,3}

¹*Institute of Physics named after academician G.M. Abdullayev's of Azerbaijan National Academy of Sciences, G. Javid ave 131, AZ 1143 Baku, Azerbaijan,*

Rahim-14@mail.ru

²*Centre for Energy Research, P.O.B. 49, H-1525 Budapest, Hungary*

³*Wigner Research Centre for Physics, P.O.B. 49, H-1525 Budapest, Hungary*

The partial, total and average coordination number of atoms and, their neighbor distributions have been determined by the neutron diffraction method and application of the Reverse Monte Carlo modeling for experimental data in As_40Se_60 , $\text{As}_40\text{Se}_30\text{S}_30$ and $\text{As}_40\text{Se}_30\text{Te}_30$ chalcogenide glasses. The total coordination number of the arsenic and chalcogen atoms is 3 and 2 for all compounds. The average coordination number is 2.4, i.e. the 8-N rule is performed and main structural element is AsSe_3 type pyramids, where depending on the chemical composition Se atom is replaced by S or Te atoms. It has been established the change of the optical gap by variation of the chemical composition.

Keywords: amorphous, chalcogenide glass, neutron scattering

PACS: 61.05.F, 71.23.Cq, 61.43 Dq

INTRODUCTION

The structure of chalcogenide glasses are characterized by short range order (SRO) determined by the coordination number, bond lengths and angle of the bond [1]. In addition, there is a certain order in the arrangement of structural elements on a nanometer scale - i.e. medium range order (MRO).

The purpose of this paper is to study the local structure and optical properties of chalcogenide glasses, with compositions As_40Se_60 , $\text{As}_40\text{Se}_30\text{Te}_30$ and $\text{As}_40\text{Se}_30\text{S}_30$. For the study were applied neutron diffraction measurements and optical results. In this study we have used the software package RMC⁺⁺ [2] while applying of Reverse Monte Carlo simulation (RMC) to experimental results for obtaining the atomic structural parameters.

EXPERIMENTAL DETAILS

The glassy bulk samples with compositions of As_40Se_60 , $\text{As}_40\text{Se}_30\text{Te}_30$ and $\text{As}_40\text{Se}_30\text{S}_30$ was powdered in order to prepare specimens for the neutron diffraction. Neutron diffraction (ND) data have been obtained on the 2-axis 'PSD' monochromatic neutron diffractometer (wavelength was $\lambda_0=1.068$ Å; $Q=0.45-9.8$ Å⁻¹) at the 10 MW Budapest Research Reactor [3], with thermal neutrons.

RESULTS AND THEIR DISCUSSION

Fig. 1a shows that all curves of the $S(Q)$ dependence in the interval $1.2 \div 1.3$ Å⁻¹ exhibit the first sharp diffraction maximum (FSDP). Fig. 1b shows FSDP curves in which the amplitude, shape and position of the maximum undergo a change depending on the chemical composition of the material. It can be seen that FSDP is weakly expressed for $\text{As}_40\text{Se}_30\text{Te}_30$ the composition than other compositions, which is evidence of higher disorder. In Fig. 2 the corresponding total pair distribution functions, $G_{\text{total}}(r)$, calculated by the RMC simulation from the experimental values of structure factors, are presented. The

diffraction result of chalcogenide samples has been attributed to the influence of MRO, and this is called first sharp peak (FSDP) or a pre-peak in the structure factor.

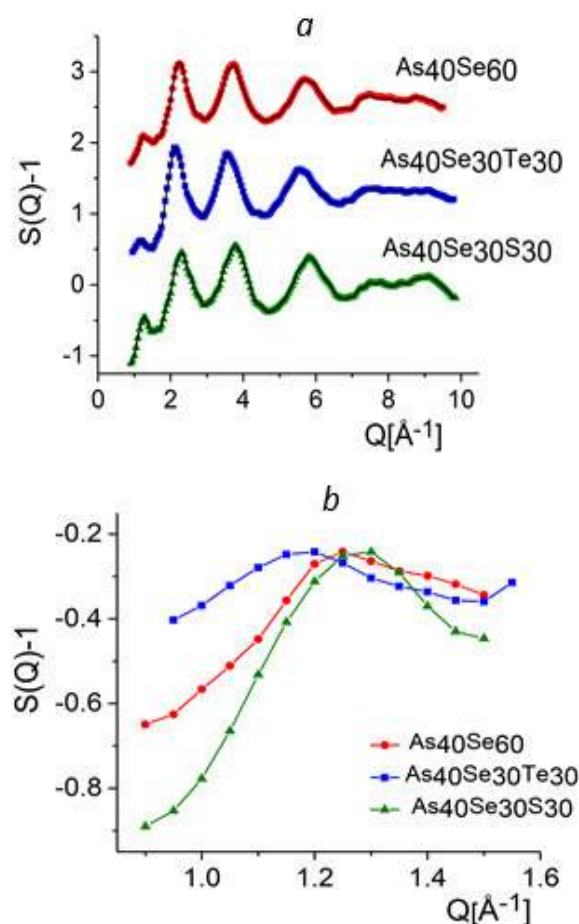


Fig. 1 Neutron diffraction structure factor, $S(Q)$ of glassy series: experimental data (color marks) and RMC simulation (solid line) (a) and the first sharp diffraction peak (FSDP) curves for As_40Se_60 (circle), $\text{As}_40\text{Se}_30\text{Te}_30$ (squares) and $\text{As}_40\text{Se}_30\text{S}_30$ (triangles) glassy series(b).

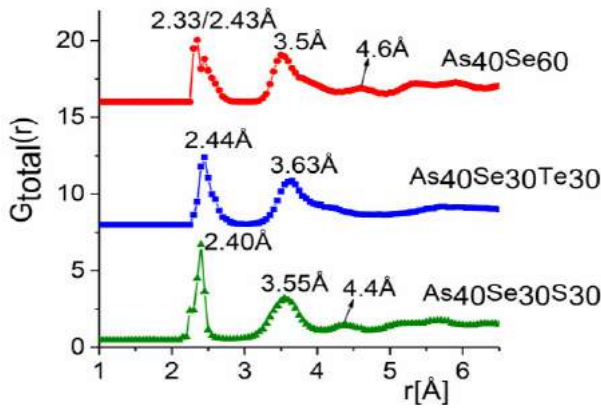


Fig. 2 Total pair correlation function obtained from the RMC modeling of $As_{40}Se_{60}$, $As_{40}Se_{30}Te_{30}$ and $As_{40}Se_{30}S_{30}$ compositions

The positions of the observed maxima on the graphs of $G_{total}(r)$ correspond to the radii of the coordination spheres. As a result, application of Reverse Monte Carlo simulation (RMC) are determined the partial structural factors, $S_{ij}(Q)$ and partial pair correlation functions, $g_{ij}(r)$. The results obtained show that, the FSDP intensity depends on the atomic number of chalcogen and also indicate the decisive role of the Se-Se correlation in the formation of MRO area. In Table 1 are summarized the short-range order parameters, i.e. “the partial coordination numbers” N_{ij} , i.e. the average number of j atoms around i atom, average number of neighbors, total coordination number, average coordination number. As can be seen, the coordination number of homopolar bonds in all the compositions is appreciably high both are between the arsenic atoms and between the chalcogenide atoms.

Table 1

Sample	Central	Neighbor				Total	Average coordination number	Calculated by the rule 8-N
		As	Se	S	Te			
$As_{40}Se_{60}$	As	0.67	2.36	-	-	3.03	2.42	2.4
	Se	1.57	0.45	-	-	2.02		
$As_{40}Se_{30}Te_{30}$	As	0.36	1.35	-	1.30	3.01	2.41	2.4
	Se	1.80	0.10	-	0.15	2.05		
	Te	1.73	0.15	-	0.10	1.98		
$As_{40}Se_{30}S_{30}$	As	0.73	1.18	1.09	-	3	2.42	2.4
	Se	1.57	0.2	0.3	-	2.07		
	S	1.45	0.3	0.25	-	2		

Table 2

Sample	Packing density	V_a cm ³ /mol	δ	ρ g/cm ³	d (Å)	L (Å)	Q_0 (Å)	ΔQ (Å)	D (Å)	Area	Amplitude
$As_{40}Se_{60}$	3.57	16.85	-0.0075	4.59	5.04	13.95	1.25	0.45	4.396	0.3954	0.23
$As_{40}Se_{30}Te_{30}$	3.36	17.91	-0.0102	5.13	5.23	12.56	1.20	0.50	4.579	0.2580	0.15
$As_{40}Se_{30}S_{30}$	2.74	15.03	-0.0118	3.86	4.83	15.70	1.30	0.40	4.226	0.6295	0.36

The parameters FSDP determined according to Fig. 1b, the position (Q_0) and full width of half maximum FWHM (ΔQ), the amplitude (Å) and area of peak are shown in Table 2.

As can be seen from the figure and the table, the numerical values of the amplitude (Å) and the maximum area decrease, and FWHM (ΔQ) is increasing, according to order $As_{40}Se_{30}S_{30}$, $As_{40}Se_{60}$, $As_{40}Se_{30}Te_{30}$, which shows the increasing degree of disorder with such series. Using the FSDP parameters, the microstructure parameters are determined by the formula

$$d = 2\pi/Q_0 \quad \text{and} \quad L = 2\pi/\Delta Q_0 \quad (1)$$

Where, the parameter d is related to the structural unit size corresponding to FSDP [4, 5]. Also, this parameter is called the quasi-periodic atomic density fluctuations, can be determined using the position of FSDP (Q_0) [5, 6] L (the structural correlation length) is determined using the width of FSDP. The microstructure parameters calculated by the equations (1) are also presented in Table 2. In case of

$As_{40}Se_{60}$ and $As_{40}Se_{30}Te_{30}$ samples, the value of d increases and L decreases. The growth of d is associated with the increase in atomic radius in some Se, Te chalcogens, while the reduction of L (size of the MRO region) is connected with increasing degree of disorder in the specified row. In Table 2 are presented the numerical values of the compactness of the structure (δ) calculated in accordance with [7], taking into account the atomic density of the elements and the measured density. The smallest value of δ obtained for the composition $As_{40}Se_{60}$ indicates a more perfect structure of the amorphous matrix in this composition. The cluster-void model is proposed by Elliott [8] to explain the nature FSDP. According to this model numerical values of D are computed and the results are presented in Table 2. The results show that value of D is increasing from $As_{40}Se_{30}S_{30}$ to $As_{40}Se_{60}$ and $As_{40}Se_{30}Te_{30}$ compositions. If we consider that the nano-voids are created due to of atoms in themselves, then the growth in their diameter is associated with an increase in the average atomic radius of the indicated compositions. As can be seen from Table 1, the experimentally determined values and

those calculated by the 8-N rule for the coordination number coincide in all compounds, i.e. 8-N rule is satisfied. The optical band gap (E_g) investigated materials undergo a change depending upon the chemical composition. When half of selenium atoms are replaced by sulfur atoms increases the band gap (E_g), determined according Tauc methods [9], but decreases by replacing tellurium atoms. As already mentioned, the substitution part of selenium atoms with sulfur contributes to the improvement of the amorphous matrix, but substitution of Se with tellurium leads to partial destruction of the structure, increasing the degree of disorder. The changes in the values of parameter may occur as a result of changes in the average molar energy of different bonds present in the material and as a result of changes in the degree of disorder of the amorphous matrices. Using the energy of different bonds [10], the average molar energy of bonds is calculated and its values are shown in Table 3, whence it is clear that the participation of sulfur atoms increases and tellurium decreases the value of the E_g parameter.

As seen from Table 3, the values of E_g for the $As_{40}Se_{60}$, $As_{40}Se_{30}S_{30}$ and $As_{40}Se_{30}Te_{30}$ chalcogenide glasses compositions are 1.82, 1.98 and 1.59 eV, respectively. Such a change in the values of E_g depending on the chemical composition can be explained with the assistance of considerations proposed by the authors of [11] considering the values of atomic density in the studied compositions.

Table.3

Film composition	E_g (eV)	Average molar energy of bonds (kcal/mol)
$As_{40}Se_{60}$	1.82	223.6
$As_{40}Se_{30}Te_{30}$	1.59	215
$As_{40}Se_{30}S_{30}$	1.98	238

CONCLUSIONS

The appearance of FSDP in the graphs $-S(Q)$ is due to the emergence of the MRO region and main role in the formation of the MRO region belongs to the Se-Se bonds environment. It has been obtained that, the optical gap strongly depends on the content. This is explained with changes in the degree of disorder and concentration of local defects depending on the chemical composition.

ACKNOWLEDGEMENTS

The research was partly supported by EU-FP7 No. 283883-NMI3 and was supported by the Science Development Foundation under the President of the Republic of Azerbaijan-Grant No. EIF/GAM-3-2014-6(21)

-
- | | |
|---|--|
| <p>[1] <i>J.P. Neufville, S.C. Moss, S.R. Ovshinsky.</i> Photostructural transformations in amorphous As_2Se_3 and As_2S_3 films. <i>J Non-Cryst Solids.</i> 1973;13:191-223</p> <p>[2] <i>O. Gereben, P. Jovari, L. Temleitner, et al.</i> A new version of the RMC++ Reverse Monte Carlo programme, aimed at investigating the structure of covalent glasses. <i>J Optoelect Adv Materials</i>, 2007, 9, 3021-3027</p> <p>[3] <i>E. Sváb, Gy. Mészáros, F. Deák.</i> Neutron Powder Diffractometer at the Budapest Research Reactor. <i>Mater Sci Forum</i>, 1996, 228, 2247-252</p> <p>[4] <i>W.H. Wei, R.P. Wang, X. Shen, et al.</i> Correlation between Structural and Physical Properties in Ge-Sb-Se Glasses. <i>J Phys Chem C.</i> 2013,117, 16571-16576</p> <p>[5] <i>K. Tanaka.</i> Topological phase transitions in amorphous semiconductors. <i>J Non-Cryst Solids</i>, 1987, 97-98, 391-398</p> | <p>[6] <i>S.R. Elliott.</i> Second sharp diffraction peak in the structure factor of binary covalent network glasses, <i>Phys Rev B.</i> 1995, 51, 8599-8601</p> <p>[7] <i>G.A. Isayeva</i> Ph.D. Dissertation in Physics, Institute of Physics, Baku, 2014</p> <p>[8] <i>T.S. Kavetsky.</i> Modified correlation equation in the FSDP-related void-based model for $As_2S(Se)_3$ chalcogenide glasses. <i>Semiconductors Phys, Quantum Electronics & Optoelectronics</i>, 2013, 16, 136-139</p> <p>[9] <i>D.I. Wood, J. Tauc</i> Weak Absorption Tails in Amorphous Semiconductors. <i>Phys Rev B.</i> 1972, 5, 3144-3151</p> <p>[10] <i>M.A. Popescu,</i> Non-Crystalline Chalcogenides (Solid-State Science and Technology Library, Vol. 8). ed. Springer. ISBN10: 0792366484. 2000</p> <p>[11] <i>M. Kastner,</i> Bonding bands, lone-pair bands, and impurity states in chalcogenide semiconductors. <i>Phys. Rev. Lett.</i> 1972, 28, 355-357</p> |
|---|--|

PREPARATION AND STUDY OF ELECTRICALLY CONDUCTIVE CERAMIC NANOCOMPOSITES BASED ON THE AZERBAIJAN BENTONITE RAW MATERIAL AND MULTI-WALLED CARBON NANOTUBES

S.H. ABDULLAYEVA^{1,2}, A.B. HUSEYNOV¹, A.O. ISRAFILOV¹, S.A. MAMMADOVA²

¹Research & Development Center for High Technologies (RDCHT), MTCHT,

Inshaatchilar ave., 2, Az-1073, Baku, Azerbaijan

²G.M. Abdullayev Institute of Physics, Azerbaijan NAS,

H. Javid ave. 131, Az-1143, Baku, Azerbaijan

israfilov.aydin@mail.ru

This work is dedicated to the fabrication and investigation of electroconductive ceramic nanocomposite materials (based on bentonite raw materials of two Azerbaijani (Atyali, Gobu) deposits and synthesized multi-walled carbon nanotubes (MWCNTs)) by means of physicochemical (SEM, XRD, derivatography (TGA / DSC), current-voltage characteristics) methods. It was revealed that the thermal stability in the air environment for both compositions of nanocomposites reached 600 °C, and the highest electrical conductivity (111.5 S m^{-1}) was shown by nanocarbon-ceramic samples obtained on the basis of MWCNTs (8 wt. %) and bentonite clay of the Gobu deposit.

Keywords: MWCNTs, AACVD, bentonite, electroconductive ceramic nanocomposites, SEM, XRD, TGA / DTA.

1. INTRODUCTION

The creation of composite materials with predetermined properties based on carbon nanotubes (CNTs) is one of the most important trends in modern materials science [1]. Ceramic materials, including those based on bentonite clays (BC) deposits of Azerbaijan [2, 3] are one of the promising matrices of composite materials based on nanotubes and are used in areas where high thermal and corrosion resistance is required [4]. In the scientific literature there is practically no data on ceramic nanocomposites based on BC and MWCNTs and the study of their electrophysical characteristics. In this regard, the work is devoted to the fabrication and complex study of electrically conductive composites based on the Atyaly and Gobu bentonite deposits and multi-walled carbon nanotubes synthesized from cyclohexane.

2. THE EXPERIMENTAL PROCEDURE

The synthesis of MWCNTs was performed by the AACVD method. As a carbon precursor, cyclohexane (CyH) was used, and ferrocene (Fc) – as a precursor of the catalyst. The synthesis conditions are given in [5].

Bentonite clay masses were preliminarily subjected to washing (clay was dispersed in distilled water, followed by filtration to remove large non-clay granular impurities). Dispersion of carbon nanotubes in bentonite clay was carried out using the two-factor method developed earlier by our colleagues [6]. Calcination of MWCNTs / BC nanocomposite samples was carried out in a quartz reactor in a flow of gas mixtures – argon (volumetric rate = 0.5 l / min) / hydrogen (volumetric rate = 0.025 l / min) at a temperature of 1050 °C for 120 minutes.

3. RESULTS AND DISCUSSION

Samples of synthesized MWCNTs and composite ceramic materials based on natural bentonite (Atyaly and Gobu) with nanotubes content of 4 % were selected for the

study. SEM image of synthesized MWCNTs is illustrated in Figure 1.

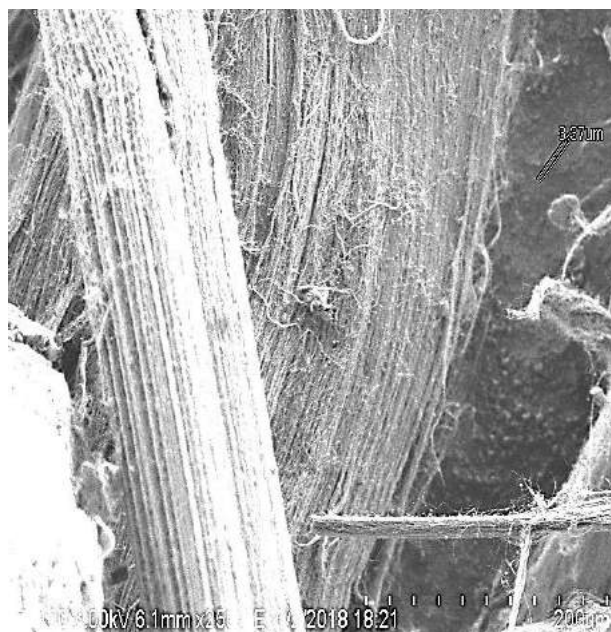


Fig. 1 – SEM image of synthesized MWNTs

From the above picture of MWCNTs (Figure. 1), it is clearly seen that nanotubes are compacted arrays of multi-walled carbon nanotubes having the shape of elongated long filaments, the so-called "carbon nanotubes forests", and the nanotubes themselves have obtained a sufficiently high degree of frequency (there are no non-tubular carbon structures).

For the nanocarbon-ceramic composites, their current-voltage (I-V) characteristics were measured (Figure. 2), and on the basis of these data, the electrical resistivity, specific resistivity, and specific conductivity of the samples were calculated.

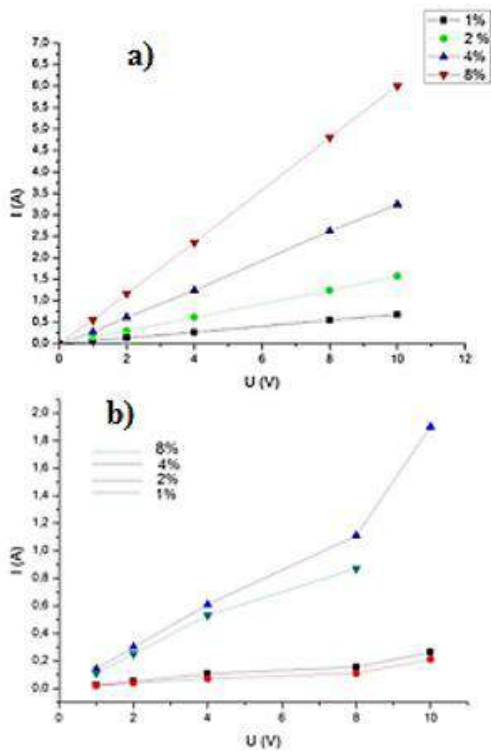


Fig. 2 Current - voltage characteristics of nanocarbon-ceramic composites based on: a) AT/MWCNTs; b) Gobu / MWCNTs.

Analyzing the data obtained, it may be deduced that, with the same MWCNTs content, the electrical conductivity of those ceramic nanocomposites is higher, which includes the clay of the Gobu deposit; this can be explained by the difference in the quantitative composition of the main components and the qualitative composition of clay impurities in two different deposits.

The thermal stability of the composites was studied by the TGA / DTA method. TGA curves of hybrid material samples have a similar character – an increase in the mass of the sample when heated in the temperature range from 80 to 605-640 °C, followed by a sharp decrease in mass with further heating. The increase in mass can be related to the process of oxidation to higher degrees of both nano-sized iron Fe and FeO (formed as a result of the reduction of iron (III) oxide by hydrogen and carbon in the calcination process of BC / MWCNTs composites) as a result of interaction with oxygen and air vapor with the formation of higher oxides (Fe₂O₃) and iron metahydroxide FeOOH. At temperatures of 605-680 °C, in the thermogravimetric curves detected an inflection characterizing sharp mass loss, which is caused by the oxidation of MWCNTs and the destruction of its carbon skeleton, with consequent release of carbon oxides (CO, CO₂). The wide pronounced exopics of oxidation on the DTA curves with a maximum at a temperature of about 700 °C also indicate that weight loss is caused by the degradation of nanotubes during combustion process.

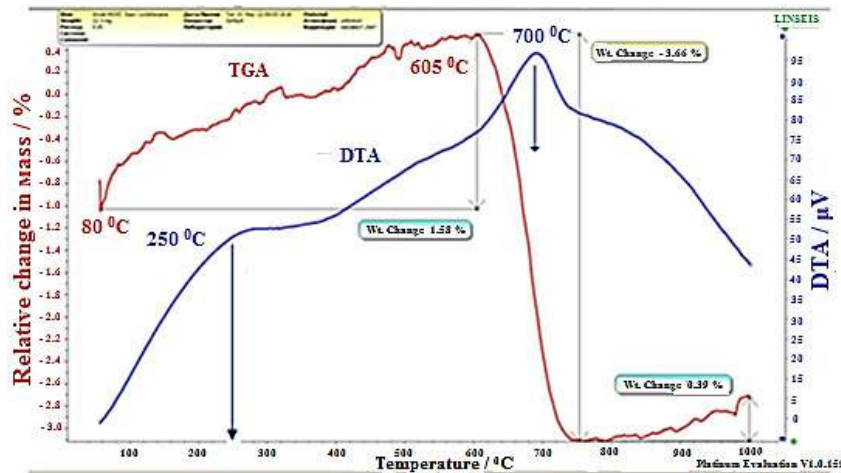


Fig. 3 Derivatogram of mass loss (TGA) and heat fluxes (DTA) curves taken from the sample AT / MWCNTs

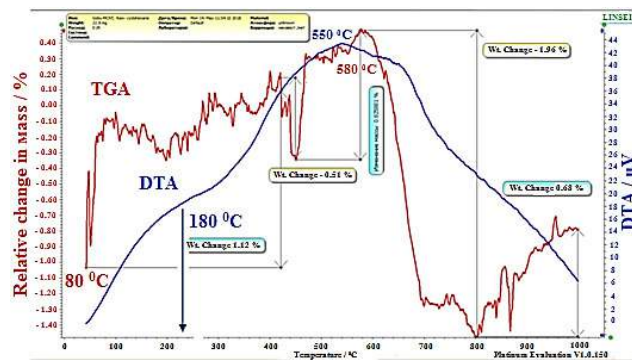


Fig. 4 Derivatogram of mass loss (TGA) and heat fluxes (DTA) curves taken from the sample Gobu / MWCNTs.

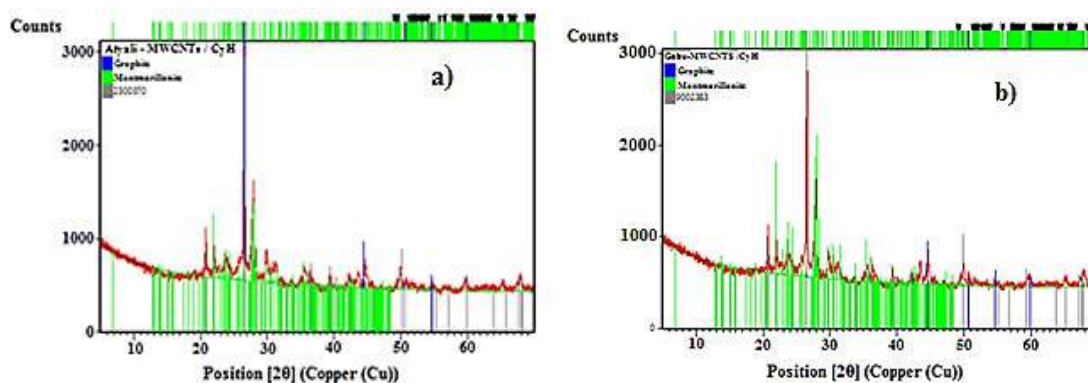


Fig. 5 X-ray diffractograms of the samples: a) AT / MWCNTs; b) Gobu / MWCNTs.

The mineralogical and phase compositions of nanoceramic composite samples were studied by X-ray diffraction analysis (Figure 5)

In the roentgenogram, the most intense peaks (marked in blue in the figure 5) indicated by (002) reflect the concentric cylindrical structure of embedded graphene sheets (hexagonal graphite structure), while the presence of reflexes $2\theta = 25.77^\circ$ imply multilayered nature of carbon nanotubes. The identified phase owned by bentonite is shown on the roentgenogram in green (in the range $25 < 2\theta$

< 47). XRD analysis data confirm the presence in the composites of two main components – multi-walled carbon nanotubes and bentonite. Thus, the above results lead to the conclusion that hybrids, which constituted a system based on bentonite minerals and MWCNTs, are promising materials that have conductivity and withstand high temperatures, by which it is possible to develop various heating elements, electrodes, substrates for microelectronic devices and other products for use in various fields.

-
- [1] S. I. Yengejeh, S.A. Kazemi, A. Öchsner Carbon nanotubes as reinforcement in composites: A review of the analytical, numerical and experimental approaches / Computational Materials Science, 2017, Vol. 136, pp. 85-11
- [2] Z.J. Afandiyeva Investigation of the basic quality properties of the Dashsalahli deposit of bentonite clays / Int. J. Adv. Res, 2018, Vol. 6, No. 2, pp. 438-441
- [3] H.M. Mahmudov, M.K. Ismayilova, G.S. Aliyeva Application of zero-valent nanoparticles for the hydrogen production from using photolysis/ Jour. of Radiation Research, 2016, Vol.3, No. 1, pp. 47-51
- [4] G. Konstantinos Dassios, Guillaume Bonnefont, Gilbert Fantozzi, E. Theodore Matikas. Novel highly scalable carbon nanotube-strengthened ceramics by high shear compaction and spark plasma sintering / Journal of the European Ceramic Society, 2015, Vol. 35, pp. 2599-2606
- [5] S.H. Abdullayeva et al, Characterization of high quality carbon nanotubes synthesized via Aerosol – CVD. / Journal of advances in physics, 2015, Vol.11, No.4, pp. 3229-3240
- [6] S.H. Abdullayeva et al, Carbon Nanotubes Dispersion in Polymers by Two-Factor Mechanical Method. 2016. pp. 291-304

REFINEMENT THE CRYSTAL STRUCTURE OF THE $\text{Ga}_{1-x}\text{In}_{1+x}\text{S}_3$

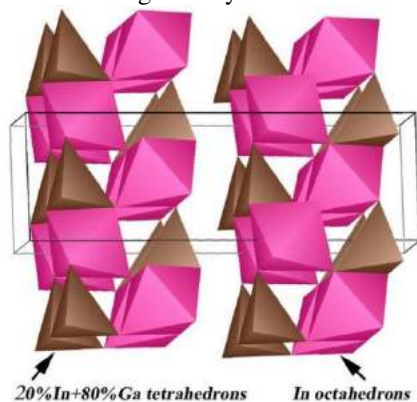
A.B. RAHIMLI, I.R. AMIRASLANOV.

G.M. Abdullayev Institute of Physics, Azerbaijan NAS,

H. Javid ave. 131, Az-1143, Baku, Azerbaijan

iamiraslan@gmail.com

The compounds of the Ga_2S_3 - In_2S_3 system are well studied and the number of grown ternary crystalline phases with the general formula $\text{Ga}_{1-x}\text{In}_{1+x}\text{S}_3$ ($0 \leq x \leq 0.5$) is more than ten [1-8]. Most of them are characterized by a layered structure. It is known that layered chalcogenides mainly refer to the hexagonal system and are characterized by closely packed structures. The building blocks of such structures are two-dimensional infinite slabs consisting of several alternating anion (A)-cation (C) layers of the A-C-... -A type. Repetition of such slabs forms a three-dimensional structure. In this case, van der Waals (vdW) bonds form between the anions of the extreme atomic layers of the neighboring slabs (or packets). Also, in the mentioned Ga_2S_3 - In_2S_3 system with the exception of one orthorhombic phase, all the other phases are belonging to rhombohedral or hexagonal crystal class.

Fig 1. The crystal structure of $\text{Ga}_{0.8}\text{In}_{1.2}\text{S}_3$.

The orthorhombic phase was obtained by the chemical transport reaction from the pre-synthesized $\text{Ga}_{1-x}\text{In}_{1+x}\text{S}_3$ ($0.25 \leq x \leq 0.5$). The transporting agent was I_2 . The crystal structure of orthorhombic GaInS_3 is presented in [3]. This structure is formed from articulated tetrahedral and octahedral fragments, with a ratio of 1: 1. Also, all tetrahedrons are occupied by Ga atoms, and the octahedrons are occupied by In atoms. The slabs of

orthorhombic GaInS_3 crystals consist of five atomic layers of S- (Ga, In) -S- (Ga, In) -S and the vdW space between them is in the form of a zigzag (Fig 1).

It was shown in [9,10] that these crystals are easily intercalated by 4-aminopyridine ($\text{NC}_5\text{H}_4\text{NH}_2$) molecules. They also found that deintercalation occurs in two stages, when about 15% of 4-AP molecules being removed in the first stage at 250°C , and complete removal of organic molecules occur at 345°C . Such a two-step decomposition of intercalate was difficult to harmonize with the crystal structure. Therefore, a need arose for a more detailed study of the crystal structure of the noted orthorhombic structure.

Obviously, octahedral positions can be populated only with indium atoms. However, tetrahedral positions can be inhabited not only by Ga atoms, but also by In atoms. Many sulfide compounds are known, where indium atoms have tetrahedral coordination. Therefore, we assumed that the stoichiometric formula of GaInS_3 does not accurately describe the structure, but should have the form $\text{Ga}_{1-x}\text{In}_{1+x}\text{S}_3$. Therefore, we have refined the crystal structure of $\text{Ga}_{1-x}\text{In}_{1+x}\text{S}_3$. The refinement performed by Rietveld method on the basis of powder x-ray diffraction data ($\text{CuK}\alpha$, $5^\circ \leq 2\theta \leq 120^\circ$, D2 Phaser, Bruker), using the program TOPAS-4.2.

The XRD pattern of $\text{Ga}_{1-x}\text{In}_{1+x}\text{S}_3$ and the difference curve between the experimental and calculated intensities are shown in Fig 2. To refine the structure, the results of [3] were used. However, the positions of the gallium atoms were refined with the condition of the possibility of partial replacement by indium atoms. As a result, it turned out that these positions are populated as 20% In + 80% Ga. Therefore, the stoichiometric formula should be written as $\text{Ga}_{0.8}\text{In}_{1.2}\text{S}_3$.

Refined parameters of the unit cell, atomic positions, interatomic distances and characteristics of the experimental diffraction peaks are shown in tables 1-3. Fig 1 shows the projection on plane of the three-dimensional structure of $\text{Ga}_{0.8}\text{In}_{1.2}\text{S}_3$.

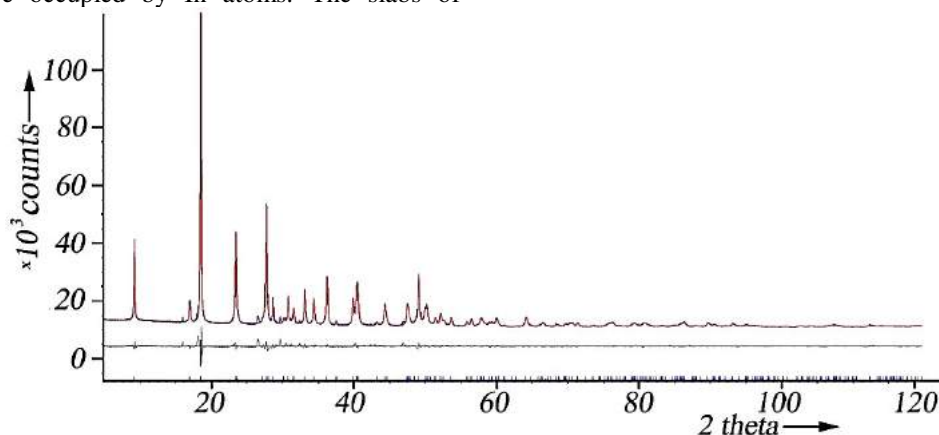
Fig 2. The XRD pattern of $\text{Ga}_{0.8}\text{In}_{1.2}\text{S}_3$

Table 1. Refined parameters of the crystal lattice of the $Ga_{0.8}In_{1.2}S_3$ compound

Space group	A21ma
Lattice parameters at 298 K (Å):	
a	6.2060(2)
b	19.0543(7)
c	3.8163(2)
Volume (Å ³)	451.27(3)
Density (g/cm ³)	4.26 (1)
R-Bregg (%)	1.032

Table 2. Atomic positional parameters of the $Ga_{0.8}In_{1.2}S_3$ crystals

Atom ident.	x	y	z	Atom type	Occupancy
Ga	0.05074(55)	0.0	0.11169(15)	Ga+3	0.80(1)
In	0.5	0.5	0.16679(10)	In+3	1
S(1)	0.2470(12)	0.0	0.22192(40)	S	1
S(2)	0.2133(16)	0.5	0.06556(45)	S	1
S(3)	0.1857(11)	0.5	0.39784(38)	S	1
Ga (In)	0.05074(55)	0.0	0.11169(15)	Ga+3, In+3	0.20(1)

Table 3. Interatomic distances in the $Ga_{0.8}In_{1.2}S_3$ compound

АТОМЫ	S(1)	S(2)	S(3)
Ga (In)	2.428(8)	2.330(6) x 2	2.272(8)
In	2.685(5) x 2 2.616(8)	2.624(9)	2.547(5) x 2

As a result, it was established that the crystals of the orthorhombic phase are characterized by the composition $Ga_{0.8}In_{1.2}S_3$. By high-temperature x-ray diffraction, we studied the temperature dependence of the deintercalation

of the mentioned in above intercalates $Ga_{0.8}In_{1.2}S_3 \cdot 4\text{-AP}$. Now the two-step nature of deintercalation does not seem unexpected.

-
- [1] *I.R. Amiraslanov, Yu.G. Asadov,; R.B. Valiev,; A.A. Musaev,; G.G. Guseinov, Structure and intercalation of GaInS₃ (b,II) polytype. Crystallography (Kristallografiya), 1990, 35, 1298-1299*
- [2] *I.R. Amiraslanov, N.G. Furmanova, F.Yu. Asadov, B.A. Maksimov, V.N. Molchanov, A.A. Musaev, Synthesis of a new semiconductor Ga_{0.5}In_{1.5}S₃ with given structure. Crystallography, 1990, 35,332-336*
- [3] *И.Р. Амирасланов, Г.Г. Гусейнов, А.С. Кулиев, Х.С. Мамедов Кристаллическая структура ромбического GaInS₃. // Кристаллография, 1987, т. 32, №1, с. 243-244*
- [4] *I.R. Amiraslanov, G.G. Guseinov, A.S. Kuliev, Kh.S. Mamedov, A.S. Amirov, Crystal structure of three-packet polytype of Ga In S₃. Crystallography (= Kristallografiya), 1988, 33, 767-768*
- [5] *I.R. Amiraslanov, F.Yu. Asadov, A.A. Musaev, G.G. Guseinov, Crystal structure of the new layered semiconductor Ga_{1.74}In_{2.92}S₇. Soviet Physics, Crystallography, 1989, 34, 611-612*
- [6] *И.Р. Амирасланов, Р.Б. Валиев, Ю.Г. Асадов, А.А. Мусаев, Г.Г. Гусейнов Полиморфное превращение ромбической фазы InGaS₃// Неорг. Матер., 1990, т. 26, с. 642-643*
- [7] *И.Р. Амирасланов, Т.Х. Азизов, Г.Г. Гусейнов, Г.М. Нуфтиев Фотоэлектрические свойства ромбического монокристалла GaInS₃. // ДАН Азерб. ССР, 1986, т. 42, №9, с.25*
- [8] *Nanfeng Zheng; Xianhui Bu; Pingyun Feng. Nonaqueous Synthesis and Selective Crystallization of Gallium Sulfide Clusters into Three-Dimensional Photoluminescent Superlattices. Journal of the American Chemical Society, 2003, 125, 1138-1139*
- [9] *И.Р. Амирасланов, Ю.Г. Асадов, А.А. Мусаев, Б.Г. Тагиев, Г.М. Нуфтиев, Ч.О. Мамедяров Рентгенографическое и оптическое исследования интеркалированных кристаллов InGaS₃. // Неорг. матер., 1990, т. 26, №8, с. 1614*
- [10] *И.Р. Амирасланов, Р.Б. Валиев, Ю.Г. Асадов, Г.Г. Гусейнов, А.А. Мусаев Структура и интеркалирование двухпакетного политипа GaInS₃(b,II). // Кристаллография, 1990, т. 35, вып. 5, с. 1298*

INFLUENCE OF INTERFACIAL PHASES ON THERMAL AND ELECTRICAL CONDUCTIVITY IN GaSb-CrSb EUTECTIC SYSTEM

**M.V. KAZIMOV, D.H. ARASLY, İ.KH. MAMMADOV*,
R.N. RAHİMOV, A.Ə. KHALİLOVA**

Institute of Physics of the Azerbaijan National Academy of Sciences

**Azerbaijan National Academy of Aviation*

mobilkazimov@gmail.com

GaSb-CrSb eutectic alloys were prepared by the vertical Bridgman method. By investigating of microstructure of GaSb-CrSb eutectic composite by electron microscope, it has been established that the interfacial zone between the semiconductor matrix and metallic inclusions is generated. In computations of effective electrical and thermal conductivity of the composite were taken into account the role of these interfacial zones.

Keywords: Eutectic composite, SEM and EDX analysis, thermal and electrical conductivity, thermoelectrics, interfacial zone.

PACS: 536.21

INTRODUCTION

Diluted magnetic semiconductor materials based on III-V compounds and 3d-metals eutectic composites, having a stable composition and properties, are promising materials for spintronic devices [1-3]. GaSb-CrSb eutectic composite, where CrSb antiferromagnetic needles are distributed in GaSb matrix is of significant interest.

Previously, by X-ray diffraction analysis it was confirmed that the GaSb-CrSb composite has a two-phase structure, and enthalpy of fusion and specific heat were determined. Heat flow and specific heat capacity studies for GaSb-CrSb eutectic composite have been made in the 293-1273K temperature range. The initial and final points of melting temperature are determined as 943K and 965K, respectively. The peaks observed on the specific heat capacity curves possibly due to magnetic transitions [4]. It has been shown that in calculation of the heat and electrical conductivity, the inter-phase zones should be taken into consideration.

EXPERIMENTAL

GaSb-CrSb eutectic composites were prepared by using the vertical Bridgman method as described in detail in ref. [5,6]. Samples for electric measurement were prepared in a parallelepiped form with size $(2 \times 4 \times 10) \text{cm}^3$. On both the lateral sides of the samples, four contact probes were attached to measure the electrical conductivity (σ), thermal power (α) using the compensation method and the thermal conductivity (K) was measured by the absolute stationary heat flow method [7,8].

RESULTS AND DISCUSSION

An investigation of the temperature dependences of the electrical conductivity in the direction of the growth of crystallization, electric current, and magnetic field in the temperature range 80-300K shows that the short-circuit effect of metallic inclusions leads to anisotropy of these parameters.

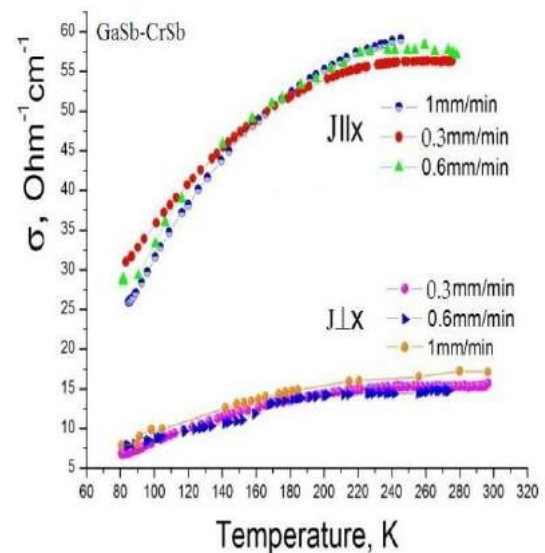


Fig.1. Temperature dependence of electric conductivity for GaSb-CrSb composite

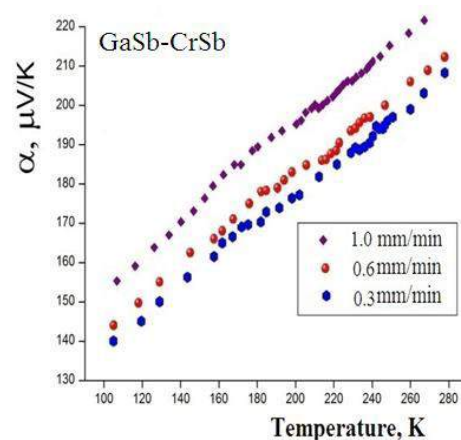


Fig.2. Temperature dependence of thermopower for GaSb-CrSb composite

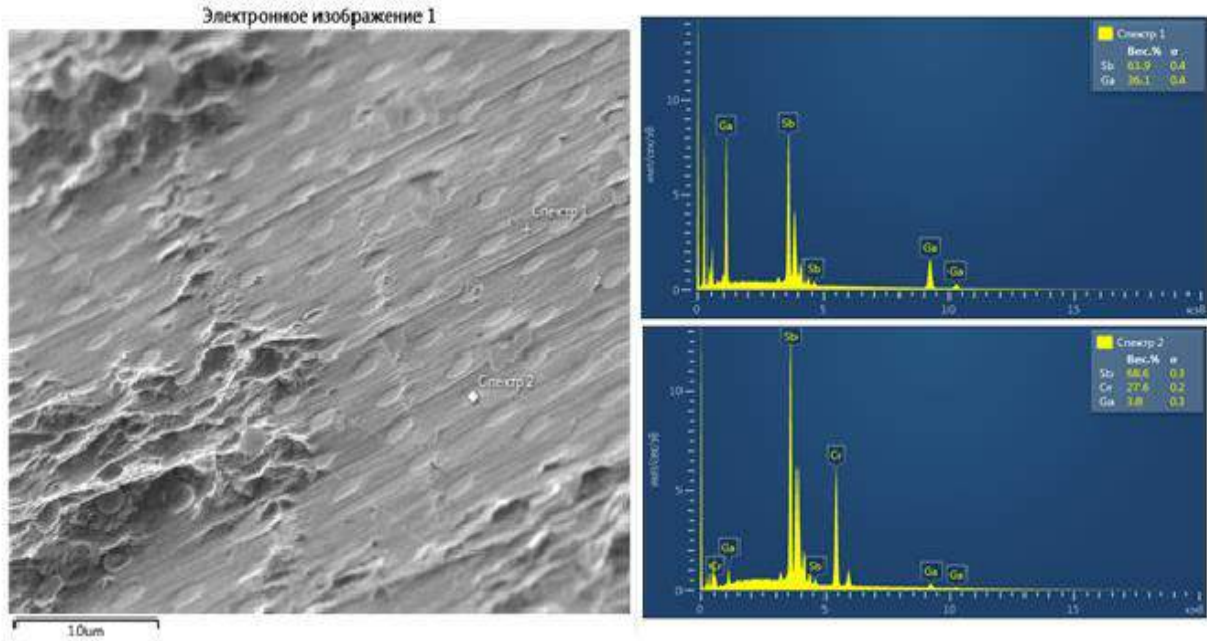


Fig.3. X-ray spectra of GaSb–CrSb obtained with SEM–EDX from the needle and matrix phases along the lateral directions of the specimens

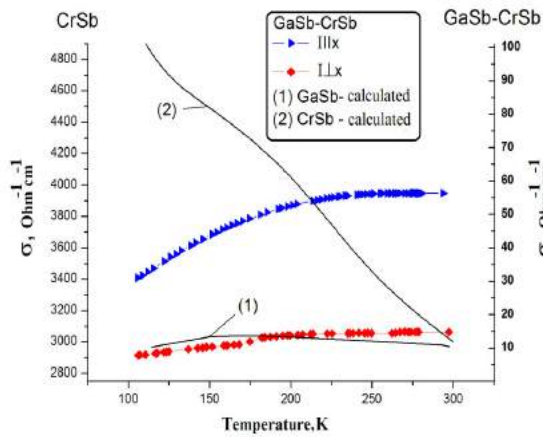


Fig.4. Temperature dependence of electric conductivity for GaSb–CrSb composite curves 1 and 2 are calculated from the formula (1)

As seen from Fig.1, due to short-circuiting action by needle-shaped inclusions, the electrical conductivity in the $I||x$ direction is significantly larger than that in the $I\perp x$ direction. The coefficient of conductivity anisotropy at 80 K is $\sigma_{||}/\sigma_{\perp}=3.2$ and decreases with increasing temperature: $\sigma_{||}/\sigma_{\perp}=3$ at 300K.

The electrical conductivity (Fig.1.) and thermopower(Fig.2.) of the samples taken with different crystallization speeds (1mm/min, 0.6mm/min, 0.3mm/min) was measured. The temperature dependence of thermo power at the mutual directions of current, magnetic field and inclusions between of 80K and 300K have been investigated. Strong anisotropy is also observed in the temperature dependence of the thermoelectric power (Fig.2).

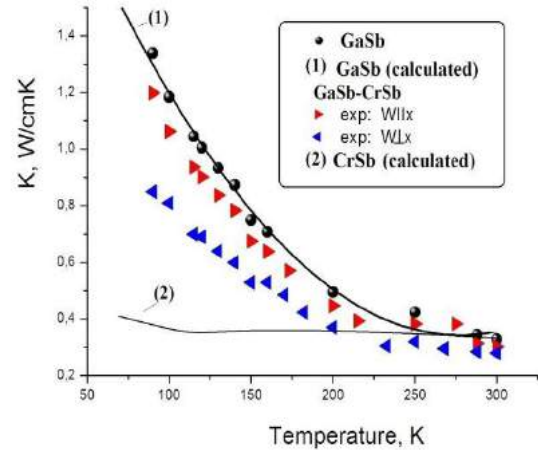


Fig.5. Temperature dependence of thermal conductivity for GaSb–CrSb composite curves 1 and 2 are calculated from the formula (2)

The short-circuiting of V_{α} potential by metallic inclusions in $\Delta T||x$ direction is caused by a decrease in the thermo power with anisotropy degree of $\alpha_{\perp}/\alpha_{||}=2.4$. The observed change in electrical conductivity and thermopower at different crystallization rates, associated with changes in the size of the inclusions, indicates the possibility of controlling the parameters of the material under study [9].

Based on SEM examinations (Fig.3), the needle-shaped metallic inclusions with a diameter of about 0.9-1.6 μm , a length of 20÷50 μm and a density of $\sim 6 \cdot 10^4 \text{ mm}^{-2}$ are uniformly and parallel distributed in the GaSb matrix. It was found that the matrix contains Ga = 36.1wt%, Sb = 63.9 wt% (Fig.3, spectrum 1), the inclusion are contained Cr = 27.8 wt%, Sb = 68.6 wt%, Ga = 3.8wt% (Fig.3, spectrum2).

Different models were proposed in order to determine composite physical parameters. In the present study, heat and electrical conductivity of the GaSb-CrSb eutectic composite was calculated based on the theory of effective ambient.

The effective electrical conductivity in the direction of crystallization (σ_{\parallel}) and perpendicular to it (σ_{\perp}) was calculated by the following expressions [10,11]:

$$\sigma_{\perp} = \frac{(\sigma_1 - \sigma_2) \left(1 - \sqrt{\frac{c}{1+c}}\right) + \sigma_1 \sqrt{\frac{1+c}{c}}}{1 + \frac{(\sigma_2 - \sigma_1) \sqrt{\frac{1+c}{c-1}}}{\sigma_1}}, \quad \sigma_{\parallel} = \sigma_1 \frac{1}{1+c} + \sigma_2 \frac{c}{1+c} \quad (1)$$

here σ_1 and σ_2 are the electrical conductivity of the matrix and metal phase, and c is the volume fraction of the metal inclusions.

The following formula is used for the effective thermal conductivity in parallel (K_{\parallel}) and perpendicular (K_{\perp}) to the metal needles [12]:

$$\left. \begin{aligned} K_{\parallel} &= K_2 + (1 - c)(K_1 - K_2) \\ K_{\perp} &= K_2 + \frac{2K_2(1-c)(K_1 - K_2)}{2K_2 + c(K_1 - K_2)} \\ c &= \frac{V_i N_i}{1 - V_i N_i} \end{aligned} \right\} \quad (2)$$

here K_1 and K_2 are the thermal conductivity of the matrix and metal phase, respectively, N_i is the density of the metal phase, V_i is the volume of the metal needles. The influence of the inclusions on the thermal conductivity is negligible due to their low volume fraction.

The temperature dependence of thermal conductivity $K(T)$ of GaSb-CrSb eutectic composite are presented on the fig. 6. Thermal conductivity up to 200K depends on temperature as $\sim T^{-0.8}$. Two features are observed in the temperature dependence: the anisotropy in $K(T)$ in parallel and perpendicular directions of metallic inclusions to the solidification front and additional thermal conductivity. At 80 K, anisotropy degree is 1.27 with temperature increasing it reduces and at room temperature disappears. The calculations have shown that free path length of the long-wavelength phonons is the same order as the transverse dimensions of metallic inclusions, which indicates the relationship of the observed anisotropy to the long-wavelength phonons scattering at the boundary inclusions.

The heat transfer mechanisms have been investigated in the framework of Callaway model. The total thermal conductivity of the composite is calculated taking into account contributions of the electron and phonon parts.

Electronic thermal conductivity is calculated by the formula Wiedemann-Franz, and phonon thermal conductivity is for relaxation model of Callaway [13]:

$$K_f = \frac{k}{2\pi^2 v} \left(\frac{k}{\eta}\right)^3 T^3 \int_0^{\theta/T} \frac{\tau_c z^4 e^z}{(e^z - 1)^2} dz \quad K_i = K_{el} + K_f, \quad (3)$$

here θ is the Debye temperature, $z = \frac{\eta\omega}{k_0 T}$, ω is the phonon frequency, τ_c is the generalized relaxation time.

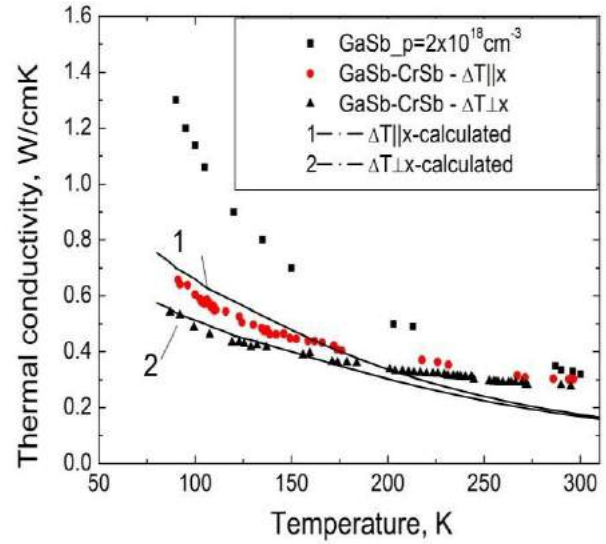


Fig.6. Thermal conductivity of GaSb and GaSb-CrSb composite, curves 1 and 2 are calculated from the formula (3)

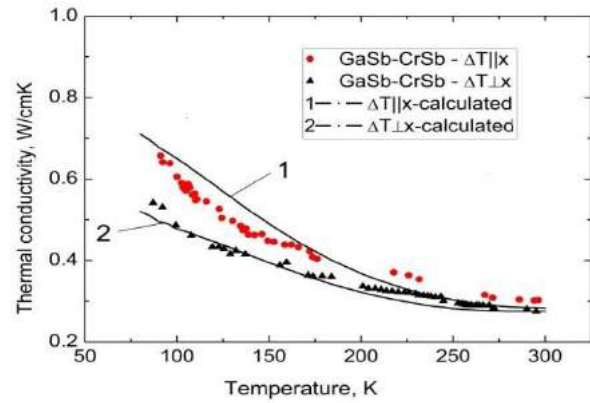


Fig.7. Thermal conductivity of GaSb and GaSb-CrSb composite, curves 1 and 2 are calculated from the formula (4)

As can be seen from Fig.6, above 200K the calculated curve is below the experimental one due to the additional thermal conductivity which is 30% of the total at 300K. Most likely, in this region there are the other mechanisms of heat transfer. Such mechanisms can be magnon and photon thermal conductivity. However, calculations show that in this region, their parts in thermal conductivity are negligible. According to Koshino and Ando model [14] the resonance energy transfer can be the dominant mechanism in thermal conductivity increasing. It is known that 3d-transition metal impurities may produce the deep and shallow impurity levels in the III-V group compounds [15]. When the excited electron from a deep local level in the band gap moves into the conduction band, other conduction electron returns to the shallow level. At thermal gradient, ionization energy is transferred to the cold edge of the sample. As seen from fig.1 electrical conductivity of GaSb-CrSb eutectic composite in the range of 80÷300K prevails over the extrinsic conductivity and in this region the resonance energy transfer is expressed as follows [13]:

$$K_2 = K_{el} + K_f + K_R \quad (4)$$

Here ϵ_{∞} is the dielectric constant, k_B is the Boltzmann constant, n_d is the local level concentration, E_d is the energy of the local level, m_0 is the mass of the

electron, we have assumed $\epsilon_{\infty}=16$ and $E_d=0.02\text{eV}$. The total thermal conductivity calculated by formula (4) well agrees with the experimental data (Fig. 6).

CONCLUSIONS

It has been shown that the role of the interphase zone in anisotropy of electric and thermal conductivity of eutectic compositions of the semiconductor-metal type is substantial and that it is necessary to take into account

volume fractions of the interphase zone in computation of effective thermal conductivity in the framework of the effective medium theory. The influence of the inclusions on the thermal conductivity is negligible due to their low volume fraction. The heat transfer mechanisms have been discussed in the framework Callaway model. The thermal conductivity calculated with taken into account the role of the charge carriers transfer, point defects, three-phonon normal and three-phonon umklapp processes and the mechanism of resonance transfer of ionization energy.

-
- [1] *S. Polesya, G. Kuhn, S. Mankovsky, H. Ebert, M. Regus, W. Bensch*, Structural and magnetic properties of CrSb compounds: NiAs structure., *J Phys Condens Matter*. 2012 Jan 25;24(3)
- [2] *M. Shirai*, Possible half-metallic ferromagnetism in zinc blende CrSb and CrAs // *Journal of Applied Physics*, 2003, v.93, No 10, pp.6844-6846
- [3] *Liu Yong, S.K. Bose, J.Kudrnovsky*, Magnetism and half-metallicity of some Cr-based alloys and their potential for application in spintronic devices. *World Journal of Engineering*, 9 (2012) 125-132
- [4] *R.N. Rahimov, I.Kh. Mammadov, M.V. Kazimov, D.H. Arasly, A. Khalilova*, *Transaction Azerbaijan NAS (Physics and Astronomy)*, 35, 5, 104 (2015)
- [5] *Y. Umehara, S. Koda*, Structure of a unidirectionally solidified GaSb-CrSb eutectic alloy // *J.Japan Inst. Metals*, 1986, v.50, pp.666-670
- [6] *R.N. Rahimov, I.Kh. Mammadov, M.V. Kazimov, D.H. Arasly, A.A. Khalilova*, *Journal of Qafqaz University-Physics*. 1, 166 (2013)
- [7] *R.N. Rahimov, M.V. Kazimov, D.H. Arasly, and A.A. Khalilova, I.Kh. Mammadov*, Features of Thermal and Electrical Properties of GaSb-CrSb eutectic composite // *Journal Ovonic Research*, 2017, v. 13, No 3, pp.113 – 118 123
- [8] *R.N. Rahimov, I.Kh. Mammadov, M.V. Kazimov, D.H. Arasly, A.A. Khalilova*, Structure and electrophysical properties of GaSb-CrSb eutectic composite, *Moldavian Journal of the Physical Sciences*, 14, 44 (2015)
- [9] *S.F. Marenkin, A.V. Kochura, I.V.Fedorchenko, A.D. Izotov, M.G.Vasilev, V.M. Trukhan, T.V. Shelkovaaya, O.A. Novodvorsky, and A.L. Zheludkevich*, Growth of Eutectic Composites in the InSb–MnSb System // *Inorganic Materials*, 2016, v.52, No 3, pp. 268-273
- [10] *W.K. Liebman and E.A. Miller*, 1963 *J. Appl. Phys.* 34 2653–9
- [11] *V.V. Leonov, E.N. Chunarev and Y.E. Spektor*, 1977, Physical–chemical process in heterogeneous system (in Russian) *Krasnoyarsk 67*
- [12] *B.I. Odelevskiy*, 1951 *J. Tech. Phys.* 21 667–77 (in Russian)
- [13] *J. Callaway, H. Baeyer*, Effect of point-imperfections on lattice thermal conductivity. *Phys. Rev.*, 120, 1149 (1960)
- [14] *S. Koshino, T. Ando.*, *J. Physical Society of Japan*, 16, 1151 (1961)
- [15] *E.M. Omelyanovskiy, V.I. Fistul*, Impurity of Transition Metal in Semiconductors (in Russian) *Moskow, Metallurgiya*, 192 (1983)

TEMPERATURE DEPENDENCE OF PHOTOLUMINESCENCE OF ZnIn₂Se₄

T.G. KERIMOVA ^{1*}, I.A. MAMEDOVA ^{1**}, Z. KADIROGLU,
N.A. ABDULLAYEV ¹, M. FELDMAN ²

¹Institute of Physics NAS Azerbaijan, ave. G. Javid, 131, AZ 1143, Baku, Azerbaijan

²Spectra-Physics Inc., 3635 Peterson Way, Santa Clara, CA 95054, USA

taira-kerimova@mail.ru*, irada_mamedova@yahoo.com**

Photoluminescence of ZnIn₂Se₄ in a wide temperature interval 10÷300K was investigated. PL spectrum consists of a wide infra-red band at 896 nm and for the first time observed band at 725 nm. Activation energy of temperature quenching of the emission band with a maximum of 896 nm is determined. The scheme of electronic levels in the band gap is constructed.

Keywords: Antistructural defects, a photoluminescence, activation energy, ZnIn₂Se₄

PACS: 78.67.Ch, 78.55.Kz, 78.66.Tr

INTRODUCTION

A²B³C₄⁶ group compounds with the ordered vacancy in a cation sublattice are intensively investigated due to their perspective application in optoelectronic devices. ZnIn₂Se₄ is typical candidate of this group. Electrical and optical properties have been investigated in [1]. Width of direct and indirect band gaps are E_{dir}=1,82 eV and E_{ind}=1,74 eV, accordingly. In [2] photoluminescence properties in the range 55÷200K are studied. Wide band of luminescence at 1,22 eV authors explained by the energy levels formed by I and V_{Zn} complexes or antistructural defects of A_B, B_A type. Photosensitive properties are studied in [3]. Photosensitive structures on the basis of In/n-ZnIn₂Se₄ are received. Width of direct and indirect band gaps determined in this work are E_{dir}=1,82 eV and E_{ind}=1,74 eV. Photoelectrical memory effect is revealed in [4], where this effect is interpreted due to existence of double charged acceptor levels.

Optical transmittance ZnIn₂Se₄ (R3m, Z=4,5) investigated by us in [5]. Optical energy gap at 300K is determined as 1,62 eV. Here transmittance spectrum is

characterized with the presence of absorption band at 850 nm.

In this work for the purpose of obtain additional information on radiation properties and electronic levels in the band gap ZnIn₂Se₄ photoluminescence properties studied in the wide temperature range 10÷300K.

SYNTHESIS AND EXPERIMENTS

Crystals for measurements were synthesized from the initial components of Zn, Ga and S were taken in the stoichiometric quantities in graphitized quartz ampoules in a vacuum silica tubes of about 10⁻⁴ mm Hg column. X-ray diffraction measurements were carried out on a Bruker D8 device. Crystals were grown by Bridjmen method. X-ray analyses of powder showed the tetragonal structure with the space group S₄². In fig.1 X - ray diffraction spectrum of the ZnIn₂Se₄ powder is shown. For photoluminescence measurements Nd:YAG laser with the wavelength of λ_{ex}=532 nm and titanium-sapphire femtosecond MaiTai laser (Spectra-Physics company) with λ_{ex}=400 nm were used as excitation sources.

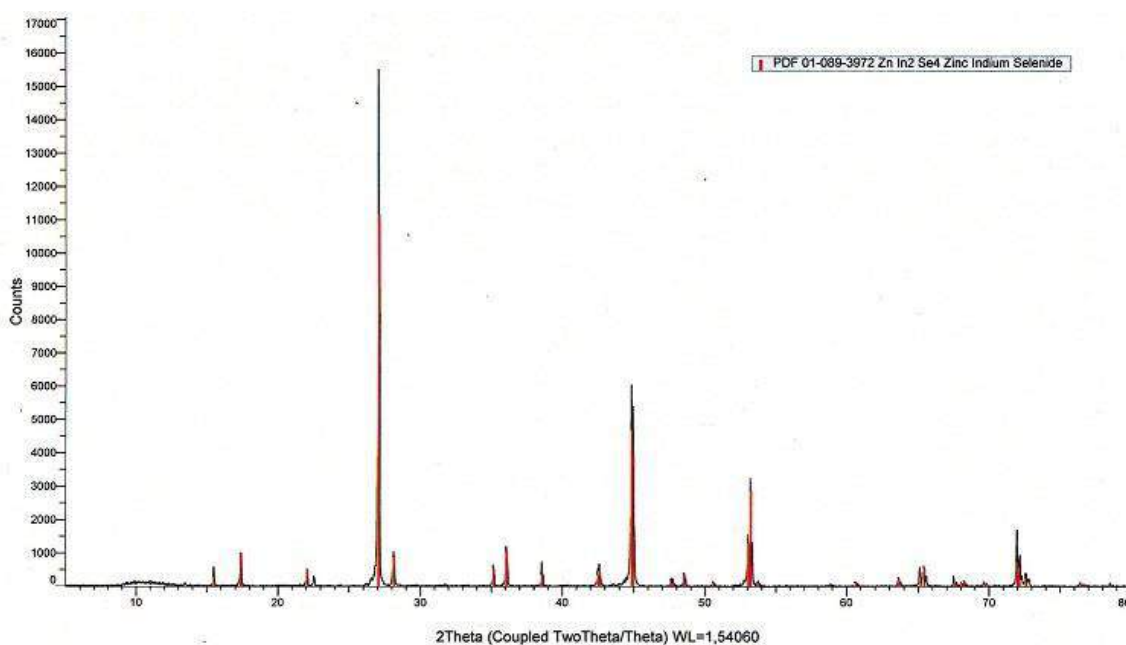


Fig.1 X-Ray diffraction spectrum of ZnIn₂Se₄ powder

DISCUSSION OF RESULTS

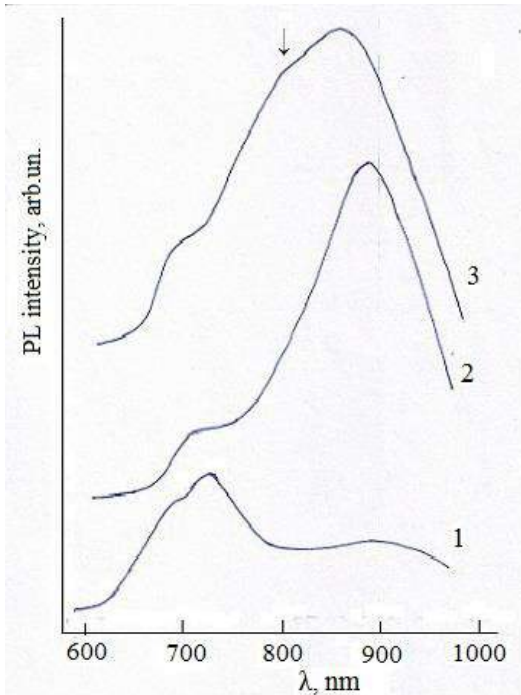


Fig.2 Photoluminescence spectra of ZnIn₂Se₄ at different temperatures 300K-(1), 83K-(2), 10K-(3)

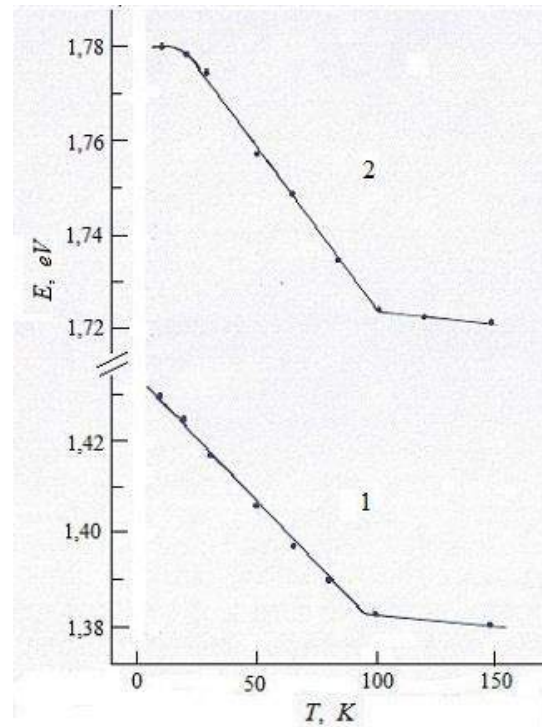


Fig.4 Thermal shift of PL maxima (1- 725nm, 2-896nm) in ZnIn₂Se₄

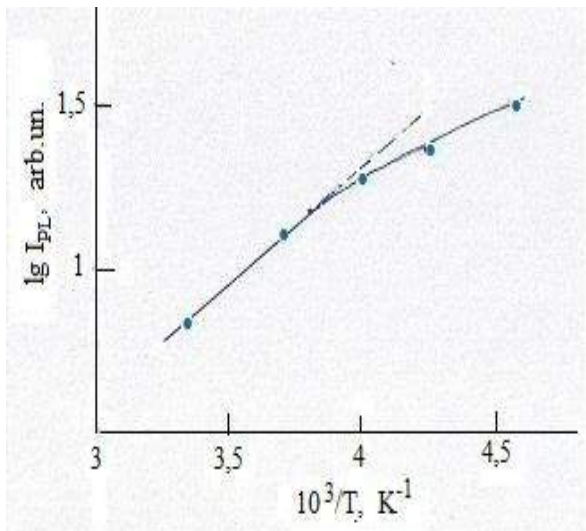


Fig.3 Temperature dependence of PL (896 nm) intensity of ZnIn₂Se₄

In fig.2 photoluminescence spectra of ZnIn₂Se₄ at 300K (1), 83K (2), 10K (3) are presented. As it is shown spectrum at 300K consist of two bands with maxima at 725 nm (1,71 eV) with short wavelength shoulder at 685 nm (1,81 eV) and less intensive wide infrared band at 896 nm (1,39 eV) (рис.2 (1)). One can assume that the split red band (685nm и 725m) is connected with interband transitions, as the value of maxima agree with the optical absorption data [1,6]. Splitting of band, apparently, is connected with valence band splitting ($\Delta_{sp}=110\text{meV}$) [7]. With the decrease of temperature bands intensity increases and below 200K infra-red band becomes more intensive (fig.2 (2)), then at temperature below 20K this band is broaden due to merge with new appearing band at ~790 nm (fig.2 (3)).

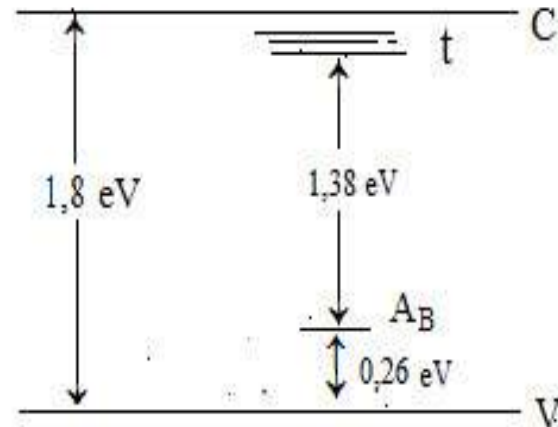


Fig.5 Energy levels scheme of electronic processes in ZnIn₂Se₄

Temperature dependence of PL band (896 nm) intensity $\lg I=f(10^3/T)$ is presented in fig.3. As it is shown, the slow temperature quenching takes place in the range 200÷260K, whereas above 260K quenching rate increases. Linear part of the temperature dependence $\lg I=f(10^3/T)$ is described by following relation:

$$I=K\exp(\Delta E/kT) \quad (1)$$

where: I is the PL intensity, K -constant, ΔE is a activation energy, k - Bolsman constant. Value for activation energy is determined equal to 164 meV.

When the temperature increase from 10K emission bands shift towards lower energies. Temperature shift coefficient of bands maxima (725 nm and 896 nm) in the linear range of shift (20÷100K) is $dE/dT \approx -0,7\text{m}\text{eV}/\text{K}$ (fig.4).

On the base of results the scheme of the radiation transitions is constructed (fig.5). Here quasi-continuously distributed states t and energy level A_B due to intrinsic disorder (antistructural defects) which characteristic for $A^2B_2^3C_4^6$ group crystals are presented. This scheme agrees with [2,8].

CONCLUSION

It is shown, that in PL spectra of ZnIn₂Se₄ the band at 896 nm at 300K is due to nature structural defects (A_B , B_A) characteristic for these compounds of $A^2B_2^3C_4^6$ group.

Activation energy of temperature quenching of photoluminescence was determined as equal 164 meV. Thus, it was established that maximum at 896 nm is connected with radiation transition from the traps located near the conduction band below for 164 meV to the energy level located above top of valence band maximum for 0,24 eV.

ACKNOWLEDGMENT

This work was supported by the grant (grant № EIF-BGM-3-BRFTF-2+/2017-15/02/1) from Science Development Foundation under the President of Azerbaijan Republic.

-
- [1] *J.A. Beun, R. Nitsche and M. Lichtensteiger*, Optical and electrical properties of ternary chalcogenides, *Physica* 27, 448-452 (1961)
- [2] *E. Grilli, M. Guzzi, and R. Molteni* *phys. Luminescence of ZnIn₂Se₄*, *Crystals, Phys. stat. sol. (a)* 37, 399 (1976)
- [3] *A.A. Vaipolin, Yu.A. Nikolaev, V.Yu. Rud', Yu.V. Rud', E.I. Terukov*, Photosensitive structures on ZnIn₂Se₄ single crystals, *Semiconductors* 37 (2003) 432
- [4] *J. Filipowicz, N. Romeo, L. Tarricone*, Photoelectrical memory effect in ZnIn₂Se₄, *Solid State Commun.* 38(1980) 619
- [5] *T.G. Kerimova, S.G. Aadullayeva, A.G. Sultanova, I.A. Mamedova*, *AJF, Fizika*, XIII,4 126-127(2007)
- [6] *Sung-Hyu Choe*, Optical energy gaps of undoped and Co-doped ZnIn₂Se₄ single crystals, *Current Applied Physics* 9 (2009) 1–3
- [7] *T.G. Kerimova*, Features of electronic spectra formation of complex diamond-lake chalcogenides of $A^{II}B_2^{III}C_4^{VI}$ type, *Inorganic Materials* 25, N11,1874-1878(1989)
- [8] *A.N. Georgobiani, S.I. Radautsan, I.M. Tiginyanu*, Wide-Gap II-III₂-VI₄ semiconductors: optical and photoelectric properties and potential applications, *Semiconductors*, 19 (1985) 193-212

INVESTIGATION OF LOW DIMENSIONAL MATERIALS ON SAPPHIRE SUBSTRATE FOR SENSOR APPLICATION

SEVDA ABDULLAYEVA^{1,2}, GULNAZ GAHRAMANOVA^{1,2}, NAHIDA MUSAYEVA^{1,2},
TEYMUR ORUJOV^{1,2}, RASIM JABBAROV^{1,2}

¹*Institute of Physics, Azerbaijan National Academy of Sciences, 131 G. Javid ave.,
AZ 1143 Baku, Azerbaijan*

²*Research and Development Center for High Technologies, Ministry of Transport, Communication
and High Technologies of Azerbaijan Republic, 2 Inshaatchilar ave., AZ 1073, Baku, Azerbaijan*
rjabbarov@physics.ab.az

In this paper we mainly analyzed the carbon nanotubes (CNTs) grown on c-plane sapphire substrate for performance of next generation sensors. The synthesis of CNTs on sapphire substrate was performed by A-CVD system with horizontal quartz reactor covered by movable electric furnace. The CNTs were grown at higher temperature (850-1000°C) using the two different methods: 1) The CNTs were synthesized by decomposition of ferrocene (Fe(C₅H₅)₂) mixed cyclohexane (C₆H₁₂) (5mg/ml) solution on pure sapphire. 2) The growth of CNT on thin Fe catalyzer (10-20 nm thickness) covered sapphire substrate using the pure cyclohexane as carbon source. Atomic Force Microscopy (AFM), Scanning Electron Microscopy (SEM) and Raman spectroscopy methods have been used to observe morphology and structure of CNTs.

1. INTRODUCTION

Low dimensional materials composed of carbon and carbon nanomaterials are a remarkable class of materials with unique properties. Materials with a large surface area to volume ratio can be a good candidate in optoelectronics applications. The past decade has seen a rapid emergence in the use of nanomaterials for sensing applications including the development of high-sensitivity and high-specificity biosensors. Since their discovery CNTs have become important scientific objects of extensive research due to their remarkable physical properties and technological applications. CNTs share the mechanical strength of graphene, but the electronic structure has many features not seen in graphene, such as the van Hove singularities arising from the one dimensional confinement, that lead to many interesting optical and electronic effects [1–3].

On the other hand CNTs are promising nanomaterials due to their high aspect ratio, superlative mechanical, thermal and electronic properties such as high thermal conductivity, high elasticity and high optical transmittance. The chemical vapor deposition (CVD) growth produces high-quality, perfectly aligned CNTs on substrates [4–6]. In this paper we mainly analyze the synthesis of CNTs on sapphire substrate for performance of next generation (bio)sensors at the next research stage. As a continuation of this work, the grown of GaN layers on the CNT/sapphire and the role of CNTs to improve the quality of GaN will be study.

2. EXPERIMENTS

The synthesis of CNTs on the c-plane sapphire substrate was performed by aerosol-chemical vapor deposition (A-CVD technique from SCIDRE). The A-CVD system consists of horizontal quartz reactor covered by movable electric furnace. This technology is based on the injection of the solution in the reactor as an aerosol and its decomposition under high temperature (850-1500°C).

As a solution for the aerosol the carbohydrate liquids were used. The high frequency (790 kHz) has been used by ultrasonic device (transducer) to obtain an aerosol from solution. Ar/H₂ mixture was flowed to the system during the synthesis process as a transport gas and the total gas flow was 300 sccm. The CNTs were grown on c-plane sapphire substrate using Fe catalyzer and organic cyclohexane solvent with two different methods:

1) The CNTs were synthesized by decomposition of ferrocene (Fe(C₅H₅)₂) mixed cyclohexane (C₆H₁₂) solution (5mg/ml ratio) on pure sapphire. In this case optimal ferrocene and cyclohexane ratio was 5mg/ml. the growth temperature and time were 950°C and 10 minutes respectively (sample A).

2) The growth of CNTs on thin Fe catalyzer (10-20 nm thickness) covered sapphire substrate using the pure cyclohexane as carbon source. Fe catalyst was deposited on c-plane sapphire substrate in 10⁻⁶Tor vacuum by e-beam evaporator (SNTEX) device. The thicknesses of catalyst approximately were between 10 and 20 nm. One piece of Fe covered sapphire substrate was annealed in air atmosphere at 500°C for 30 minutes, and then CNTs were synthesized on this substrate (sample B). The CNT also was grown on the second piece of thin Fe layer covered (not annealed) sapphire substrate (sample C). The growth temperature and time for these two samples were same with sample A.

3. RESULTS AND DISCUSSIONS

Atomic Force Microscopy (AFM), Scanning Electron Microscopy (SEM) and Raman spectroscopy methods have been used to observe morphology and structure of CNTs.

The Raman spectroscopy (532 nm) was used for detection of carbon nanotubes on sapphire and study of nanotube structure (Fig. 1). The samples were investigated at room temperature and pressure at 4mW and 8mW laser excitation powers.

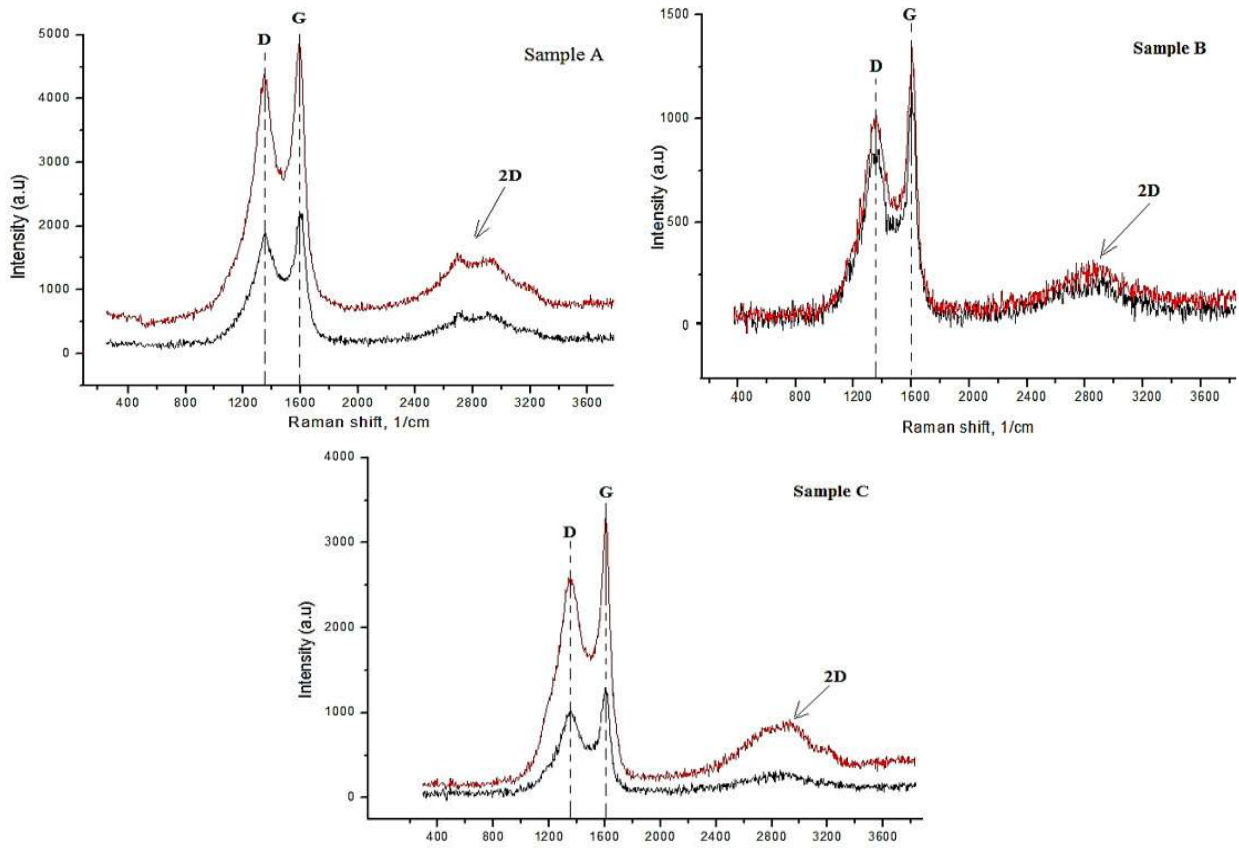


Fig. 1. Raman spectrum from a MWCNTs samples grown on sapphire substrate (black- at 4mW red- at 8 mW laser excitation powers).

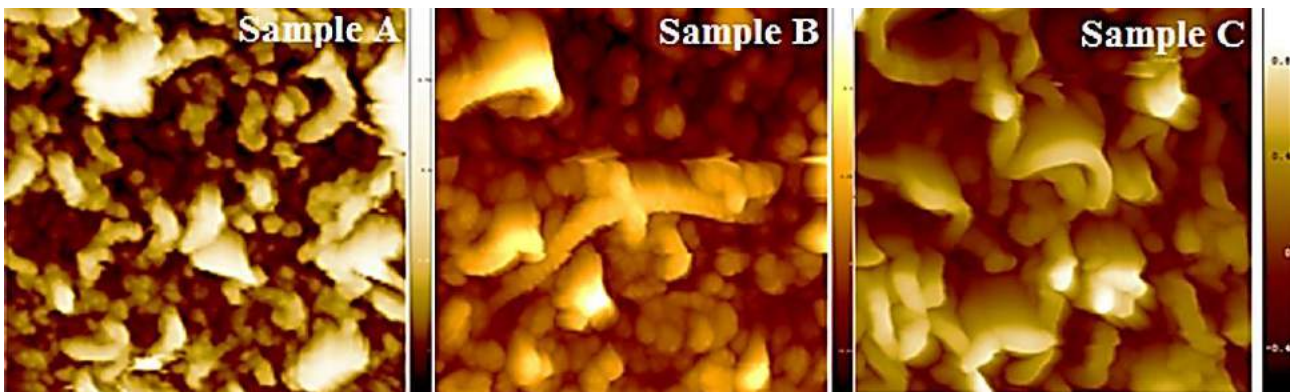


Fig. 2a-c show the atomic force microscopy topography forward 2D images of CNTs.

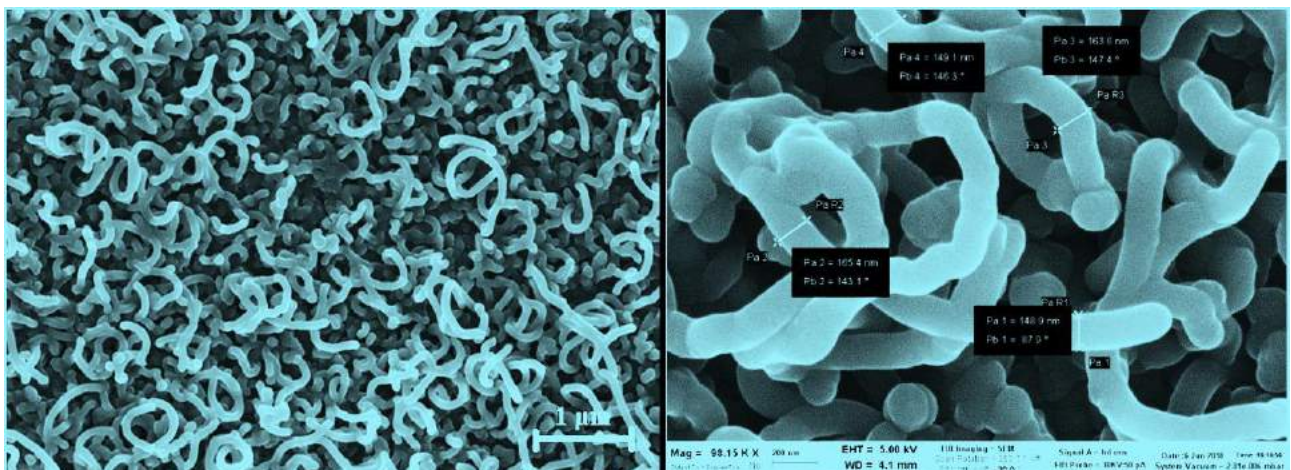


Fig. 3 SEM picture of the CNTs deposited on Fe covered c-plane sapphire substrate (left). On the right the magnification is enlarged. (SEM investigations were done at Institute of Materials for Electronics and Magnetism, in Italy)

Due to the specific Raman resonance effects it was possible to detect Raman scattering spectra of a small bundle of MWCNTs. A strong feature at around 1323 cm^{-1} , 1337 cm^{-1} , 1327 cm^{-1} respectively sample A, B and C, the so-called D line, assigned to disordered graphitic material. A group of peaks in the approximate range $1600\text{--}1610\text{ cm}^{-1}$ labelled the G band. In graphite, the G band exhibits a single peak related to the tangential mode vibrations of the C atoms. A line at around 2800 cm^{-1} , the second order harmonic of the D mode, labelled 2D. According to the Raman intensity and lines ratio samples C indicates high structure quality and less amorphous carbon to compare sample A and B.

AFM (Bruker) experiments were performed in ambient condition. Topography forward 2D images indicate the horizontal and mixed CNTs on sapphire substrate (Fig. 2). Comparison of AFM results from three examples it can be also seen that CNTs are more visible in sample C. Therefore the SEM investigation was done for only on sample C. SEM (ZEISS FE) investigations were confirmed that the empty (without Fe inside tube) CNTs were grown

on sapphire substrate and the diameters some of them were between $145\text{nm}\text{--}165\text{ nm}$ (Fig. 3).

4. CONCLUSIONS

The CNTs have been grown on sapphire substrate at 950°C by two catalytic (Fe) methods. The optimal growth method was confirmed by Raman spectroscopy and AFM. SEM investigations were indicated that the most of CNTs were empty (Fe free) and the diameter and length of CNTs were 170 nm and $1\text{ }\mu\text{m}$ respectively.

ACKNOWLEDGEMENTS

The authors thank Dr. Babayev Sərdar for performing Raman spectroscopy measurements. This work was partly financially supported by the Science Development Foundation under the President of the Republic of Azerbaijan-Grant № EIF/GAM-4-BGM-GİN-2017-3(29)-19/02/1

-
- [1] *R.H. Baughman, A.A. Zakhidov, and W.A. de Heer, Science* 297, 787, 2002
- [2] *S. Han, X.L. Liu, C.W. Zhou* Template-free directional growth of single-walled carbon nanotubes on a- and r-plane sapphire. *J Am Chem Soc*, 2005, 127: 5294–5295
- [3] *Z.Y. Zhang, X.L. Liang, S. Wang, et al.* Doping-free fabrication of carbon nanotube based ballistic CMOS devices and circuits. *Nano Lett*, 2007, 7: 3603–3607
- [4] *Y.B. Chen, J. Zhang*, Chemical vapor deposition growth of single-walled carbon nanotubes with controlled structures for nanodevice applications. *Acc. Chem. Res.* 2014, 47, 2273–2281
- [5] *C.Q. Feng, Y.G. Yao, J. Zhang, Liu, Z.F.* Nanobarrier-terminated growth of single-walled carbon nanotubes on quartz surfaces. *Nano Res.* 2009, 2, 768–773
- [6] *Y.B. Chen, Y.Y. Zhang, Y. Hu, L.X. Kang, S.C. Zhang, H.H. Xie, D. Liu, Q.C. Zhao, Q.W. Li, J. Zhang*, State of the art of single-walled carbon nanotube synthesis on surfaces. *Adv. Mater.* 2014, 26, 5898–5922

THE STRUCTURAL FEATURES OF CRYSTALLINE PHASES OF THE GaSe-InSe SYSTEM

I.R. AMIRASLANOV, K.K. AZIZOVA, S.S. BABAYEV, Y.R. ALIYEVA

Institute of Physics ANAS, Baku, Azerbaijan

iamiraslan@gmail.com

The phase formation in the GaSe - InSe systems is considered. Synthesized compositions $Ga_xIn_{1-x}Se$ ($x = 0, 0.1, 0.2, \dots, 1.0$) and the regions of mutual solid solutions of these compounds are determined. The investigations were carried out by XRD, DTA and Raman spectroscopic methods. The temperatures of the transitions from the hexagonal phase to the tetragonal phase are determined. The presence of an individual compound of $GaInSe_2$ was confirmed.

Keywords: semiconductor, solid solution, crystal structure, XRD, DTA, Raman spectroscopy

It is known that layered compounds of GaSe and InSe crystallize in a hexagonal structure, the slabs of which consist of four atomic layers, such as Se-Me-Me-Se [1-8]. The structures and physical properties of these compounds have been studied quite well. However, the structures of ternary compounds of the type $Ga_xIn_{1-x}X$ ($X = S, Se, Te$) have been studied little. The information available in the literature is scanty and sometimes contradictory. The only paper devoted to X-ray structure analysis of $GaInSe_2$ was published in 1985 by the authors H.-J. Deiseroth, D. Muller, H.Hahn [9]. To obtain the $GaInSe_2$ compound, Ga and In were first melted in stoichiometric ratios, then adding Se, all the components were re-melted together. Further, the solidified ingot was annealed for a long time at temperatures of 550-650° C. The authors established that the compound crystallizes in the tetragonal system on the structural type $Tl^{IV}Tl^{III}Se_2$. It is noted that in the diffraction pattern there are quite a lot of non-indexed peaks, the origin of which was not established.

In [10], the presence of a hexagonal phase for $GaInSe_2$ is reported for the first time. However, the values of the parameters a and c given here correspond to the above-mentioned tetragonal phase. A detailed inspection of the work [10] showed that the diffraction indices indicated in this work also correspond to the tetragonal phase, rather than the hexagonal one. Consequently, the representation of this phase as hexagonal is erroneous. This error is corrected in [11], where the diffraction pattern taken from the article [10] is given, but the author characterizes it as tetragonal. In the literature, there are no other data on the structure of $GaInSe_2$ crystalline phases. Consequently, only the tetragonal phase is known for $GaInSe_2$, which crystallizes in the structural type $TlSe$.

The semiconductor compounds GaSe and InSe are of great practical interest as a promising material for optoelectronics. The study of the phase diagram of GaSe-InSe and the refinement of the solid solution regions of these compounds can contribute to controlling their properties. As is known, the crystal structures of GaSe and InSe contain intermetallic Ga-Ga and In-In bonds, respectively. Another interesting issue is the refinement of the nature of the interactions between Ga and In atoms in $Ga_xIn_{1-x}Se$ solid solutions. Are intermetallic Ga-In bonds formed? To answer these and other similar questions, we synthesized the formulations $Ga_xIn_{1-x}Se$, where x varies in the interval $0 \leq x \leq 1$ in steps of 0.1. Synthesis was carried out by melting the elements in the ratios taken in the appropriate chemical formula and placed in evacuated

quartz ampoules. Further, in order to homogenize, the obtained ingots were annealed at a temperature of 450°C for a period of 14 days. Figure 1 shows the diffraction patterns of all synthesized ingots.

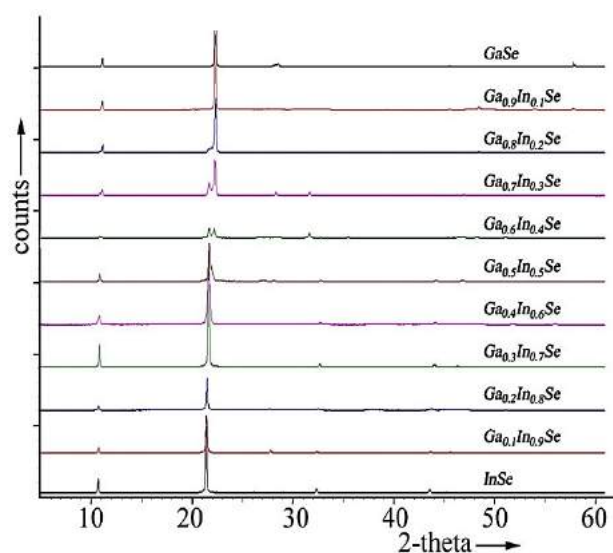


Figure 1. Diffraction patterns of obtained ingots with compositions $Ga_xIn_{1-x}Se$.

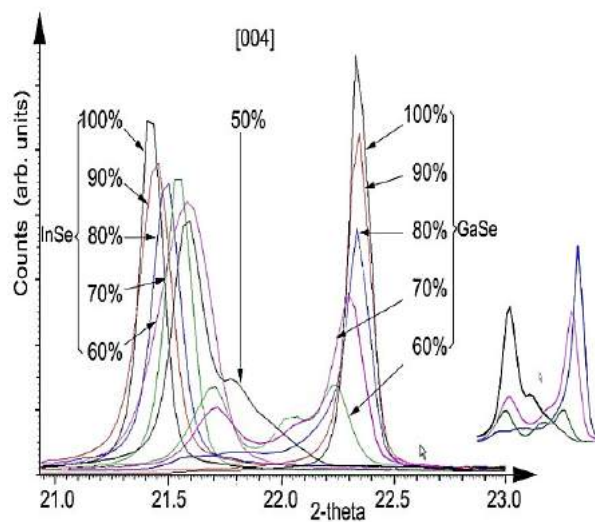


Figure 2. Diffraction peak profiles for the reflex [004], for all received ingots $Ga_xIn_{1-x}Se$

From these diffractograms, we can draw the following conclusions:

- all these diffraction patterns refer to the structural type of GaSe. As is known, this structure is layered, and its blocks consist of four atomic layers of Se-Ga-Ga-Se. Due to the presence of a Ga-Ga bond in it, it is not a stoichiometric compound.

- As can be seen from the figure in the interval between InSe and 0.6InSe-0.4GaSe, the peak profile is symmetrical and looks as one. Apparently, this site can be considered as the solid solution region based on InSe. In this segment, the resulting compounds also belong to the structural type of GaSe.

- On the basis of the obtained diffraction patterns, the values of the parameters of the hexagonal axis "c" were determined. It is found that for GaSe and InSe they differ approximately 0.7 Å (15.94 Å and 16.64 Å, respectively). Differences in the parameters of the unit cell led to the individual behavior of these two compounds. As can be seen from Fig. 1, continuously solid solution, covering the whole spectrum, is not observed. This is clearly seen in the central part of the figure, where two peaks are clearly visible. The left of them will refer to solid solutions based on InSe, and the right ones to solid solutions based on GaSe

- With a close examination at the central section of the picture, another peak is visible. (Fig. 2). However, when inspecting the whole diffraction image in general, no peaks were found that did not fit into the overall GaSe type diffraction pattern. This suggests that the compound to which these intermediate peaks belong also crystallizes in the structural type of GaSe.

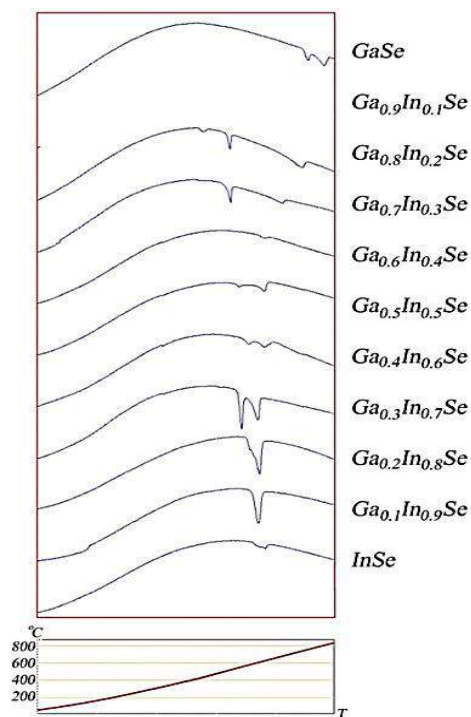


Figure 3. DTA characteristics of all obtained ingots $Ga_xIn_{1-x}Se$.

We think that under these conditions the appearance of these peaks indicates the formation of an individual

compound of the Se-Ga-In-Se type. Of course, for a convincing proof of this assumption, carrying out additional research is necessary.

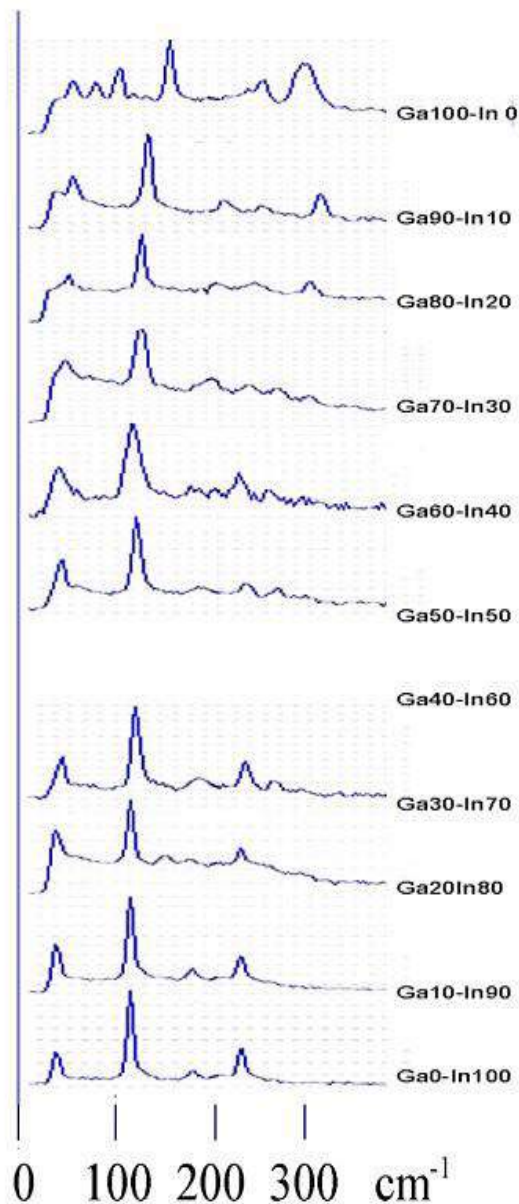


Figure 4. Raman spectra of all obtained ingots $Ga_xIn_{1-x}Se$.

Figure 3 shows the differential thermal analysis (DTA) curves of synthesized ingots. In the section where the In content predominates, two endo effects are seen. The second one relates to the melting of compounds. Our investigations showed that the first endo-effect relates to the transition to the tetragonal phase, which was noted in [1]. We obtained a tetragonal phase and refined its crystal structure. Figure 4 shows the Raman spectra of the samples obtained. A detailed description of the comparative analysis of the results obtained from x-ray studies, DTA characteristics and Raman spectra will be given in the report.

- [1] *P. Gomez da Costa, R.G. Dandrea,, R.F. Wallis, M. Balkanski*, First-principles study of the electronic structure of gamma-InSe and beta-InSe. *Physical Review, Serie 3. B - Condensed Matter* (18,1978-), 1993, 48, 14135-14141
- [2] *Y. Watanabe, H. Iwasaki, N. Kuroda, Y. Nishina*, A pressure-induced nonlayered structure of indium monoselenide. *Journal of Solid State Chemistry*, 1982, 43, 140-150
- [3] *A. Likforman, D. Carre, J.E. Bachet, B. Bachet*, Structure cristalline du monoseleniure d'indium In Se. *Acta Crystallographica B* (24,1968-38,1982), 1975, 31, 1252-1254
- [4] *R.W.G. Wyckoff*, Second edition. Interscience Publishers, New York, New York *Crystal Structures*, 1963, 1, 85-237
- [5] *L.I. Tatarinova, Yu.K. Auleitner, Z.G. Pinsker*, The electron diffraction analysis of GaSe. *Kristallografiya*, 1956, 1, 537-541
- [6] *K. Schubert, E. Doerre, M. Kluge*, Zur Kristallchemie der B-Metalle. III. Kristallstruktur von Ga Se und In Te. *Zeitschrift fuer Metallkunde*, 1955, 46, 216-224
- [7] *K. Cenzual, L.M. Gelato, M. Penzo, E. Parthe*, Inorganic structure types with revised space groups.I. *Acta Crystallographica B*, 1991, 47, 433-439
- [8] *R.W.G. Wyckoff*, Second edition. Interscience Publishers, New York, New York *Crystal Structures*, 1963, 1, 85-237
- [9] *H.-J. Deiseroth, D. Muller, H. Hahn*. Strukturuntersuchungen an InGaSe, und InGaTe. *Z. anorg. allg. Chem.* 525 (1985) 163-172
- [10] *M. Mobarak, H. Berger, G. F. Lorusso, V. Capozzik, G. Pernak, M.M. Ibrahimand, G. Margaritondo*. The growth and characterization of GaInSe₂ single crystals. *J. Phys. D: Appl. Phys.* 30 (1997) 2509–2513
- [11] *R.H. Al Orainy*. Interpretation of Switching Properties of InGaSe₂ Single Crystal. Vol. 121 (2012) *Acta Physica Polonica A*

INFLUENCE OF TEMPERATURE, FREQUENCY AND COMPOSITION OF $\text{TlIn}_{1-x}\text{Er}_x\text{Se}_2$ SOLID SOLUTIONS ON THEIR DIELECTRIC PERMITTIVITY AND CONDUCTIVITY

A.M. PASHAEV, E.M. KERIMOVA, S.N. MUSTAFAEVA

Institute of Physics NASA, Bakusolmust@gmail.com

$\text{TlIn}_{1-x}\text{Er}_x\text{Se}_2$ ($x=0; 0,001; 0,005; 0,01$) solid solutions have been obtained by direct synthesis method from initial elements. By X-ray method there have been determined crystallographic parameters of $\text{TlIn}_{1-x}\text{Er}_x\text{Se}_2$ crystals. It is shown that with the increase of Er concentration in the crystals the unit cell parameters a and c decrease. There have been measured dielectric characteristics of Er-doped TlInSe_2 crystals. It is found that doping of TlInSe_2 crystals by erbium leads to decrease in the values of the dielectric permittivity and the electrical conductivity, not having a substantial effect on the behavior of temperature dependences of given characteristics and phase transitions temperatures. The density of states at the Fermi level; the average time of charge carrier hopping between localized states, average hopping distance, scattering of trap states near the Fermi level have been evaluated for crystals of $\text{TlIn}_{1-x}\text{Er}_x\text{Se}_2$ solid solutions.

Keywords: chalcogenides, semiconductors, solid solutions, unit cell parameters, dielectric permittivity, specific electric conductivity, phase transition

PACs: 71.20.Eh, 71.20.Nr72.15.Eb, 72.15.Rn, 72.20.Ee, 72.20.Jv, 72.30.+q

TlInSe_2 ternary compound belongs to the great group of $\text{TlA}^{\text{III}}\text{B}_2^{\text{IV}}$ ($A=\text{In, Ga, B}=\text{S, Se, Te}$)-typed semiconductors-segnetoelectrics has the interesting set of physical properties both scientifically and practically. Most of this group crystals are layered that leads to the strong anisotropy of their physical characteristics. Layered packets can be shifted easily with respect to each other that brings about to the advent of polytype modifications and as a result the substantial influence of production method and external effects on their properties [1,2]. For some of this family with the temperature change the sequence of structural phase transitions due to the presence of long-period commensurate and incommensurate modulated superstructures have been observed [3,4]. There have been a number of works in which the investigation results of various physical properties of given crystals owing to the temperature and anomalies on the curves of these dependences are revealed that are indicative of phase transitions in $\text{TlA}^{\text{III}}\text{B}_2^{\text{IV}}$ -typed compounds [5-7]. While investigating thermal capacity and crystallographic parameters of TlInSe_2 crystals the authors [6-7] found out phase transitions at $T_1=135\text{K}$ and $T_2=185\text{K}$ and suppose that these transitions are due to the modulated structure. Although in [8] by investigating TlInSe_2 crystal thermal capacity within temperatures $42\div 300\text{K}$ no anomalies on the curve $C_0=f(T)$ are found out. This family crystals are of significant practical interest for optoelectronics as they are optically active and have high photosensitivity within wide spectral range.

It is known that composition change by various element doping and creating solid solutions has a significant influence on physical properties [9-12]. In [9,10] there have been presented the results of influence of Er-doping on the physical properties of TlGaSe_2 and TlGaS_2 crystals. It is shown that partial substitution of Ga by Er leads to the decrease of dielectric permittivity, specific conductivity and to the increase of charge carrier concentration in forbidden band.

It is of great interest to establish how TlInSe_2 compound doping affects on its physical properties. Therefore, the aim of the given work is to investigate

structural and dielectric characteristics of $\text{TlIn}_{1-x}\text{Er}_x\text{Se}_2$ system due to the temperature, frequency and composition.

$\text{TlIn}_{1-x}\text{Er}_x\text{Se}_2$ solid solutions have been obtained by direct synthesis method from initial elements taken in stoichiometric relations by their immediate alloying in vacuum up to 10^{-3}Pa . From TlInSe_2 -based obtained samples $\text{TlIn}_{1-x}\text{Er}_x\text{Se}_2$ single crystals are growth by using Bridgman method. X-ray diffraction study of $\text{TlIn}_{1-x}\text{Er}_x\text{Se}_2$ crystals was carried out on X-ray diffractometer DRON-3 with using CuK_α monochromatic radiation. Registration of diffraction spectra was made out automatically in step-by-step regime with $0,03^\circ$ along 2θ . The calculations of unit cell parameters are conducted on the base of recorded diffraction patterns using the method of Rietveld analysis with Fullprof program packet. Measurements of dielectric constant (ϵ) and electric conductivity (σ) were carried out by method of plane condensator by digital meter E-7-20 at frequencies $10^3\text{-}10^6\text{Hz}$ within temperature range $85\text{-}300\text{K}$. The temperature was controlled by differential chromel-copel thermocouple and multipurpose digital voltmeter. There has been used the method of continuous quazi-static heating at a rate of $\sim 0,5\text{K/min}$ for measurements. Measurement accuracy of temperature is $0,1\text{-}0,2\text{K}$. Error of dielectric characteristics measurements is $\sim 0,5\%$.

From diffraction patterns of mono- and polycrystalline samples of $\text{TlIn}_{1-x}\text{Er}_x\text{Se}_2$ it was found that the obtained $\text{TlIn}_{1-x}\text{Er}_x\text{Se}_2$ crystals ($x=0; 0,001; 0,005; 0,01$) are homogenous. It was shown that $\text{TlIn}_{1-x}\text{Er}_x\text{Se}_2$ doped by Er crystallizes into the structure with space group $D_{4h}^{18}\text{-I}4/mcm$. On the base of obtained roentgenograms there have been calculated unit cell parameters a and c of crystals under investigation depending on the composition. Calculation results are shown in Fig.1. It is seen that the partial substitution of In by Er brings about the decrease of unit cell parameters. In Fig.2 there have been presented temperature dependences of dielectric permittivity of $\text{TlIn}_{1-x}\text{Er}_x\text{Se}_2$ crystals at the frequency of 1MHz . The dependences within the phase transitions for the first and fourth compositions (TlInSe_2 and $\text{TlIn}_{0,99}\text{Er}_{0,01}\text{Se}_2$) have been shown in the upper left corner of Figure 2.

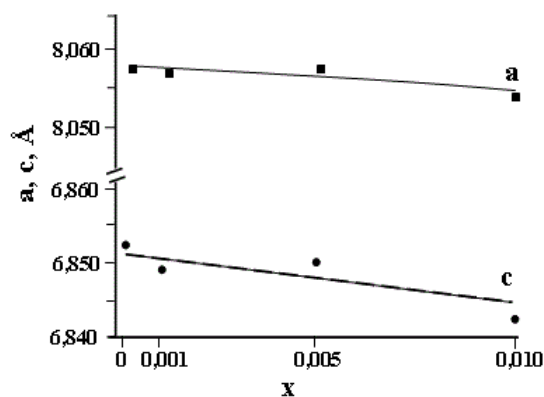


Fig.1 Concentration dependences of $TlIn_{1-x}Er_xSe_2$ unit cell parameters

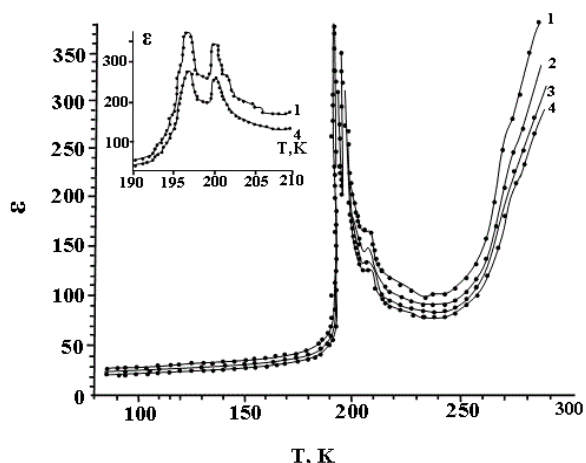


Fig.2 Temperature dependences of dielectric permittivity of $TlIn_{1-x}Er_xSe_2$ crystals: 1 - $x = 0$; 2 - $x = 0.001$; 3 - $x = 0.005$; 4 - $x = 0.01$.

It is seen that the partial substitution of In by Er leads to the slight decrease of magnitude ϵ and does not affect on the view of temperature dependence and anomaly positions related to the phase transitions of the second kind of “commensurate- noncommensurate phase” that are characteristic of given compound [5].

At all studied frequencies the ac - conductivity of the Er-doped $TlInSe_2$ crystals (Figure 3) varies according the law $\sigma_{ac} \sim f^{0.8}$, characteristic of hopping conduction through localized states near the Fermi level [13]. In terms of Mott theory, we calculated the density of states at the Fermi level from the measured experimental values of the conductivity $\sigma_{ac}(f)$. Calculated values of N_F for $TlIn_{1-x}Er_xSe_2$ ($x = 0.005$ and 0.01) single crystals were equal to $8 \cdot 10^{17}$ and $1.2 \cdot 10^{18} \text{ eV}^{-1} \cdot \text{cm}^{-3}$, correspondingly. The theory of ac hopping conductivity provides an opportunity to determine the average distance R and time τ of charge carrier hopping from one localized state to another. Calculated values of τ and R for both $TlIn_{1-x}Er_xSe_2$ ($x = 0.005$ and 0.01) single crystals were equal to $5,7 \cdot 10^{-2} \mu\text{s}$ and 320 \AA , correspondingly. We estimate also energetic scattering of trap states near the Fermi level: $\Delta E = 0.018 \text{ eV}$ for $TlIn_{1-x}Er_xSe_2$ crystals with $x = 0.005$ and 0.012 eV for $x = 0.01$.

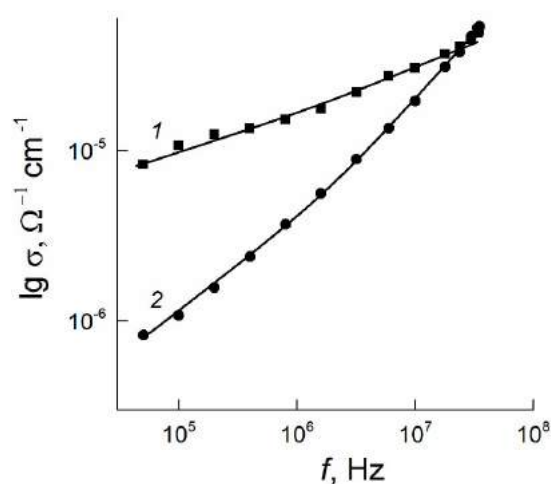


Fig. 3. AC-conductivity of $TlInSe_2$ (curve 1) and $TlInSe_2:Er$ (1 mol % Er) (curve 2) vs frequency at $T = 300 \text{ K}$.

- | | |
|---|--|
| <p>[1] N.A. Borovoy Physics of Solid State. 2009.V. 51. No 11. P. 2229-2232</p> <p>[2] O.B. Plush, A.U. Sheleg. Crystallography reports. 1999. V. 44. No 5. P. 873-877</p> <p>[3] D.F. McMorrow Journal of Physics: Condensed Matter. 1990. V. 2. No 16. P. 3699-3703</p> <p>[4] A.U. Sheleg, O.B. Plush Physics of Solid State. 1994.V. 36. No 1. P. 226-230</p> <p>[5] A.U. Sheleg, A.G. Hurtavy, S.N. Mustafaeva, E.M. Kerimova Physics of Solid State. 2011.V. 53. No 3. P. 443-445</p> <p>[6] O.Z.Alekperov, M.A.Aljanov, E.M. Kerimova Turkish Journal of Physics. 1998. V. 22. No 11. P. 1053-1058</p> <p>[7] V.A. Aliev, M.A. Aljanov Inorgan.Materials. 1998. V. 34. No 3. P. 274-276</p> <p>[8] K.K. Mamedov, A.M. Abdullaev, E.M. Kerimova PSS(a). 1986. V. 94. No 1. P. 115-119</p> | <p>[9] S.N. Mustafaeva, M.M. Asadov, E.M. Kerimova, N.Z. Gasanov Inorganic Materials. 2013. V. 49. № 12. P. 1175–1179</p> <p>[10] С.Н. Мустафаева, М.М. Асадов, Э.М. Керимова ФТТ. 2013. Т. 55. № 12. С. 2346–2350</p> <p>[11] А.М.Пашаев, С.Н. Мустафаева, Э.М. Керимова Ученые записки Национальной Академии Авиации. 2013. Т. 15. № 4. С. 56-64</p> <p>[12] А.М.Пашаев, С.Н. Мустафаева, Э.М. Керимова, Н.З. Гасанов Ученые записки Национальной Академии Авиации. 2014. Т. 16. № 3. С. 29 - 37</p> <p>[13] N. Mott and E. Davis, Electron processes in noncrystalline materials, Clarendon Press, Oxford, 1971. 472 p.</p> |
|---|--|

IBR-2 - PULSED SOURCE FOR NEUTRON SCATTERING RESEARCH AT JINR

V.N. SHVETSOV

Joint Institute for Nuclear Research, Dubna, Russia

shv@nf.jinr.ru

Joint Institute for Nuclear Research (JINR), which was established in 1956 by 12 countries, at present is a partnership of eighteen member-countries committed to the goal of collective performance of theoretical studies, building and operating of the world's leading facilities for research in condensed matter physics, nuclear physics and elementary particle physics. Participation of six associated member-countries in JINR activities is based on bilateral agreements signed on the governmental level. The

The IBR-2 fast pulsed reactor is operated by the Frank Laboratory of Neutron Physics (FLNP), one of the seven JINR Laboratories. FLNP provides user access to the 15 modern neutron scattering instruments enabling high level research, based on neutron scattering techniques and complementary methods to investigate the structure, dynamics and microscopic properties of nanosystems and novel materials, which are of great importance for the development of nanotechnologies in the fields of electronics, pharmacology, medicine, chemistry, modern condensed matter physics and interdisciplinary sciences.

Present status of the IBR-2 reactor as well as the complex of its spectrometers will be presented.

INTRODUCTION

The IBR-2 - a powerful high-flux periodically pulsed reactor was put in operation in 1978-1984 at a mean power of 2 MW [1, 2]. In 2007, the reactor reached the service life limit on fuel burn up and fluence on the reactor vessel and was shut down for modernization and replacement of the primary reactor equipment. The main objectives of the modernization were to increase safety, reliability and experimental possibilities of the reactor for the next 25 years of operation [3].

IBR-2 REACTOR

By 2010 the installation of new equipment was completed and followed by a successful power startup in 2011. The IBR-2 parameters before and after modernization are presented in Table 1 [4]. The main parts of the reactor are shown schematically in Figure 1. The reactor core is an irregular hexahedron composed of fuel

element subassemblies. Plutonium dioxide pellets with 95% of ^{239}Pu are used as a reactor fuel. The cooling system has three circuits and two loops. The IBR-2 is a sodium-cooled fast neutron reactor. The core is installed in a double-walled steel vessel and surrounded by several stationary reflectors, control and safety units among them, as well as water moderators serving 14 horizontal beam extraction ports. Water moderators of the reactor thermalize fast neutrons down to a thermal energy range used by experimenters on the extracted neutron beams.

A unique feature of the reactor is the periodic modulation of reactivity, which is accomplished by the rotation of the main moveable reflector and the auxiliary moveable reflector near the core (Figure 2). The rotors of the main and auxiliary movable reflectors rotate in opposite directions with different velocities. At a frequency of 5 Hz the reactor is brought from a deep subcritical state to a prompt supercritical one. A power pulse is generated at the moment when both reflectors approach the core.

Table 1.

IBR-2 Parameters before and after Modernization

Parameter	Before modernization	After modernization
Average power, MW	2	2
Fuel	PuO ₂	PuO ₂
Number of fuel assemblies	78	69
Maximum burnup, %	6.5	9
Pulse repetition rate, Hz	5, 25	5, 10
Pulse half-width, μs :		
fast neutrons	215	245
thermal neutrons	320	340
Rotation rate, rev/min:		
main reflector	1500	600
auxiliary reflector	300	300
Coolant	Sodium	Sodium
Thermal neutron flux density from moderator surface:		
- time average	$\sim 10^{13} \text{ n/cm}^2\cdot\text{s}$	$\sim 10^{13} \text{ n/cm}^2\cdot\text{s}$
- burst maximum	$\sim 10^{16} \text{ n/cm}^2\cdot\text{s}$	$\sim 10^{16} \text{ n/cm}^2\cdot\text{s}$

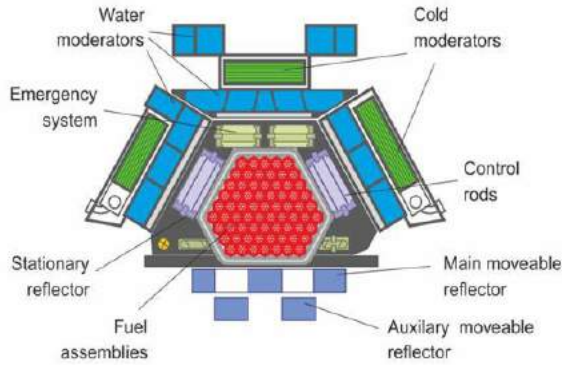


Figure 1 Main parts of the IBR-2 reactor

After modernization of the IBR-2 reactor a pelletized cold neutron moderator based on the solid mixture of aromatic hydrocarbons (benzene derivatives) as the moderating material, was installed [5]. IBR-2 cycles (approximately 8-9, comprising 2500 hours of operation per year) are usually carried out either in the water or cryogenic mode.

By 2015 the number of the instruments accessible within the user program reaches 15, compare to 11 before the modernization, significantly extending the experimental capacities and areas of research carried out [6].

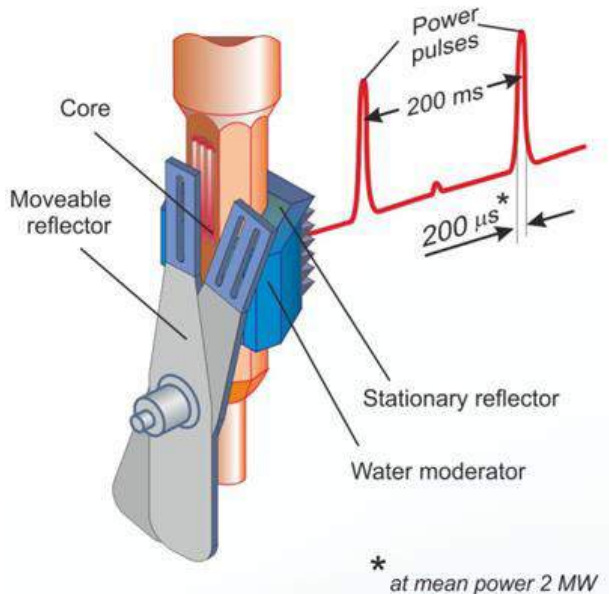


Figure 2 Core of the IBR-2 reactor with a movable and stationary reflector and water grooved moderators

SCIENCE AT THE IBR-2 REACTOR INSTRUMENTS

The main objectives of the research at the IBR-2 reactor instruments are the applications of neutron scattering techniques and complementary methods to investigate the structure, dynamics and microscopic properties of nanosystems and novel materials, which are of great importance for the development of nanotechnologies in the fields of electronics, pharmacology, medicine, chemistry,

modern condensed matter physics and interdisciplinary sciences [6].

The list of the main scientific directions, performed at the IBR-2 neutron scattering instruments and other facilities includes:

- ✓ Investigation of the structure and properties of novel functional materials;
- ✓ Investigation of the structure and properties of materials under extreme conditions;
- ✓ Investigation of fundamental regularities of real-time processes in condensed matter;
- ✓ Investigation of atomic dynamics of materials for nuclear power engineering;
- ✓ Computer simulation of physical and chemical properties of novel crystalline and nanostructured materials;
- ✓ Investigation of magnetic properties of layered nanostructures;
- ✓ Investigation of structural characteristics of carbon- and silicon-containing nanomaterials;
- ✓ Investigation of molecular dynamics of nanomaterials;
- ✓ Investigation of magnetic colloidal systems in bulk and at interfaces;
- ✓ Structural analysis of polymer nanodispersed materials;
- ✓ Investigation of supramolecular structure and functional characteristics of biological materials;
- ✓ Investigation of structure and properties of lipid membranes and lipid complexes;
- ✓ Investigation of texture and physical properties of Earth's rocks, minerals and engineering materials;
- ✓ Non-destructive control of internal stresses in industrial products and engineering materials;
- ✓ Introspection of internal structure and processes in industrial products, rocks and natural heritage objects;
- ✓ Radiation hardness of the semiconductors, polymers and biological objects;
- ✓ Neutron activation analysis in Life Sciences, biotechnology and material science.

NEW DUBNA SOURCE FOR NEUTRON SCATTERING

The Frank Laboratory of Neutron Physics proposes a project of a new fourth-generation neutron source with record parameters, which is to be put into operation after expiration of the service life of the IBR-2 research nuclear facility in 2032-2037 (depending on the operating mode). The working title of the project is Dubna fourth-generation neutron source: DIN-IV. The scientific rationale for the project was presented at the meeting of the Program Advisory Committee for Condensed Matter Physics on January 19, 2017 [7]. The need for a next-generation neutron source is driven not only by the development of neutron research in JINR, but also by a growing interest in these investigations against the background of a steadily decreasing number of neutron sources in the world, as evidenced by the analysis of a specially established

ESFRI Physical Sciences and Engineering Strategy Working Group [8].

The DIN-IV is a subcritical assembly with mechanical modulation of reactivity driven by a superconducting linear proton accelerator with an energy of about 1.0 GeV and an average current of about 0.1 mA with a variable pulse duration from 10 to 200 μ s. The principal difference between the DIN-IV and the world's existing and projected pulsed neutron sources is the use of a subcritical core with an internal neutron-producing target with the total neutron multiplication at a level of several tens, which ensures nuclear-safe operation of this

facility. The proton beam power on the target is only about 0.1 MW, which is 50 times less than the declared power of the ESS accelerator. Calculations show that the average thermal neutron flux density of this source can be higher than $5 \cdot 10^{14}$ n/cm²s, which is comparable to the calculated estimate of the European Spallation Source (ESS) being constructed in Lund, Sweden and other projects. The DIN-IV is designed to operate in two neutron pulse duration modes: short pulses of 20 \div 30 μ s and long pulses of 200 \div 300 μ s, which will make it possible to study the structure and dynamics of condensed matter with optimum spatial and energy resolution.

-
- [1] *V. L. Aksenov, V. D. Ananyiev, and E. P. Shabalin*, "Repetitively pulsed research reactor IBR-2: 10 years of operation," in Proceedings of the Topical Meeting on Physics, Safety and Applications of Pulse Reactors, Washington, D.C., Nov. 13–17, 1994, p. 111
- [2] *A.V. Belushkin*, IBR-2 – the fast pulsed reactor in Dubna. Neutron News 1991, 2, 14-18
- [3] *V.D Ananiev, A.V. Vinogradov, A.V.Dolgikh, Yu. N. Pepelyshev* Physical and power start-up of the modernized IBR-2M research reactor. Proceedings of the European Research Reactor Conference, Saint-Petersburg, Russia, 21-25 April, 2013, p. 4-10
- [4] *V.N. Shvetsov*, Neutron Sources at the Frank Laboratory of Neutron Physics of the Joint Institute for Nuclear Research. Quantum Beam Sci.2017,1, 6
- [5] *V. Ananiev, A. Belyakov, M. Bulavin, E. Kulagin, S. Kulikov, K. Mukhin, T. Petukhova, A. Sirotin, D. Shabalin, E. Shabalin, V. Shirokov, A. Verhoglyadov*, The world's first pelletized cold neutron moderator at a neutron scattering facility. Nuclear Instruments and Methods in Physics Research B 320 (2014) 70–74
- [6] *V.L. Aksenov, A.M. Balagurov, D.P. Kozlenko* Condensed matter research at the modernized IBR-2 reactor: from functional materials to nanobiotechnologies. PEPAN 2016, 47, 627–646
- [7] *V.L. Aksenov* JINR Communications E3-2017-12, JINR, Dubna, 2017
- [8] Neutron scattering facilities in Europe. Present status and future perspectives, ESFRI PSE Strategy Working Group, Neutron Landscape Group, ESFRI Scripta Vol. I, 2016

SUPERLATTICE STRUCTURE OF YbAs₄S₇ NANO THICK FILMS

E.Sh. HAJIYEV

*Institute of Physics, Academy of Sciences of Azerbaijan,
131 H. Javid, Baku AZ – 1143, Azerbaijan
hellase75@gmail.com*

The conditions growth of thin films of YbAs₄S₇ obtained vacuum deposition has been defined using electron diffraction method. It is established epitaxy relations existing between long periodic superstructure phases and initial structures.

Keywords: growth of thin films, electron diffraction, super lattice structure

PACs: 68.55. + b, 68.60. + q.

The study of crystallization kinetics of amorphous thin layers of the structure of phases and thin epitaxial layers in the nanoparticles of the Yb - As - S system and the ternary of the given systems is one of the perspective directions of the limited size structures. These compounds are one of the most promising materials in the development of nanoelectronics because the use of these materials opens up new opportunities for the creation of semiconductor materials and devices on the basis of nanometer-scale structure elements. Unique properties of multicomponent nanoparticles with rare earth element are of particular importance in nanotubing of devices that can be controlled by external magnetic fields.

YbAs₄S₇ film thickness of ~ 20 nm, prepared by evaporation of the synthesized substance and deposition rate with 5.0 nm/sec to crystals of NaCl, KCl, NaBr, LiF, KJ and celluloid, are obtained at room temperature in the amorphous state (Fig.1).

The electron diffraction pattern of YbAs₄Se₇ amorphous film shows diffuse rings corresponding to the values $s=4\pi\sin\theta/\lambda=25,33; 41,70; 62,50; 84,20; 95,60\text{nm}^{-1}$ obtained in [1]. Prolonged storage of the amorphous films at room temperature does not lead to spontaneous crystallization. Heating the YbAs₄Se₇ amorphous layers on single crystal substrates up to $T_s=473$ K resulted in the formation of the crystalline phase orthorhombic modification. Polycrystalline films diffraction pattern from which indicate based rhombic crystal lattice parameters $a = 1,191; b = 1,445; c = 0,403$ nm, as obtained by preheated in a substrates temperature range 373 - 513 K (Fig. 2).

A different picture is observed on the electron diffraction patterns taken from samples obtained on NaCl and KCl substrates heated above 473 K. In addition to the main reflections characteristic of the known lattices YbAs₄S₇, new satellite diffraction reflections also appear on the electron diffraction patterns. In the temperature range of LiF substrates from 573 to 613 K, a mixture of polycrystalline samples with a mosaic single crystal is formed. (fig.3).

By increasing temperature, the intensity of the lines of the diffraction field corresponding to the polycrystalline decreases, and the point reflexes indicative of the formation of monocrystalline blocks increase. Further increase in substrate temperatures to 633 K leads to the formation of a mosaic YbAs₄S₇ single crystal. (fig.4.)

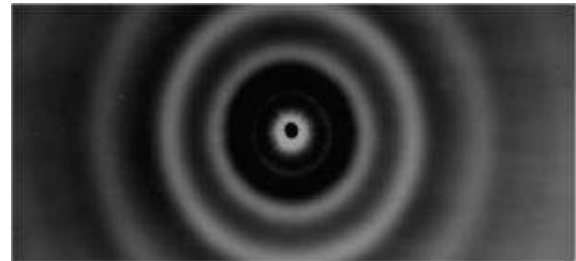


Fig.1 Electron diffraction pattern of amorphous YbAs₄S₇ films

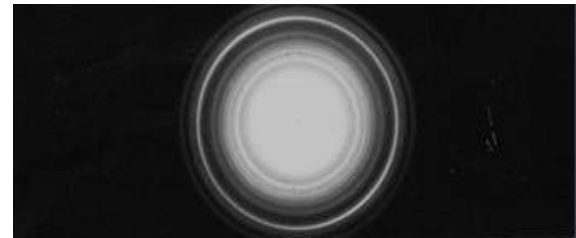


Fig.2 Electron diffraction pattern of polycrystalline YbAs₄S₇ films

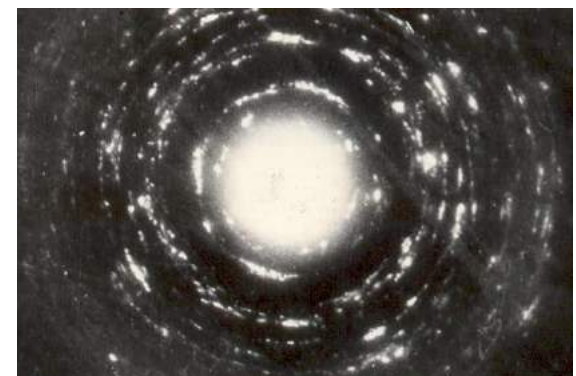


Fig.3 Electron diffraction pattern of polycrystalline samples with a mosaic single crystal.



Fig.4 Electron diffraction pattern from single crystal superstructure phase of YbAs₄S₇.

The electron diffraction patterns obtained from these films, including additional weak ones, are displayed in the orthorhombic cell with parameters: $a \approx 2a_0 = 2.382$; $b \approx 2b_0 = 2.891$; $c \approx 2c_0 = 0.806$ nm. These relationships indicate

that the new crystal lattice should be considered as a superstructure of the known lattice of YbAs_4S_7 nanothin films.

[1] *E.G. Efendiyev and E.Sh. Hajiyev* Short – range order parameters in amorphous YbAs_2S_4 and

YbAs_4S_7 films. // *J. of Non – Crystalline Solids* 163, 1993, p. 29– 34

ROLE OF SULPHUR IN THE A- CVD GROWTH OF SINGLE WALL CNTs

R.F. HASANOV^{1,2}, N.N. MUSAYEVA^{1,2}, S.S. BABAYEV¹¹*Institute of Physics, ANAS,**131, H. Javid ave. , Baku, Azerbaijan*²*R&D Center for High Technologies MCHT,**2, Inshaatchilar ave. Baku, Azerbaijan*rovshen_1989@mail.ru

Single-walled carbon nanotubes (SWCNTs) have exceptional electrical and unique optical properties, rendering them being applied in various application fields, especially in transparent conducting films (TCFs). The fabrication methods of SWCNTs play a big role in their obtaining and controlling the diameters and structures..

For many years sulphur has been known as a good promoter to growth of carbon fibers in the metal-catalyzed chemical vapor deposition systems. In the present paper the Single Wall carbon nanotubes (SWCNTs) were synthesized by means of Aerosol CVD method. A little amount of pure sulphur powder was mixed with Ferrocene, which is used as a catalyzer and high frequency (800 kHz) transducer transformed the solution (ferrocene/sulphur/x-lene) to the aerosol. The growth processes were carried out at 850-1000°C in the horizontal reactor at the atmospheric pressure.

The morphology of the samples was observed by SEM and Raman spectroscopy with 532 nm laser being used to analyze the diameter distribution of the obtained nanotubes. The presence of 1- 1.4 nm diameters of SWCNTs in the samples has been determined.

Keywords SWCNTs, Raman, Sulphur, A-CVD, SEM

PACs: 85.35.Kt; 81.16.Be

INTRODUCTION

Single-walled carbon nanotubes (SWCNTs) have exceptional electrical and unique optical properties, rendering them being applied in various application fields, especially in transparent conducting films (TCFs). The fabrication methods of SWCNTs play a big role in their obtaining and controlling the diameters and structures.

The synthesis methods as arc – discharge [1], laser ablation [2, 3] are suitable to grow SWCNTs with low diameter, high – quality and purity, but the drawback is the high cost of synthesis. The catalytic CVD method has drawn much attention due to it being different from all above. CCVD has a potential for producing SWCNTs continuously and in large amount, in which SWCNTs are grown on a substrate or as agglomerates in the reactor with the use of pure hydrocarbon gases or carbon monoxide as feedstock [4-6]. Additionally, CNTs are synthesized by CCVD method, in which a carbon containing gas is decomposed at high temperature in the presence of a metal catalyst [7, 8]. The metallic catalyst is often a transition metal, with iron, cobalt and nickel being the notable ones.

Other metals such as chromium, platinum, molybdenum, palladium and copper are used as catalyst promoters [9,10]. Such promoters change the electronic structure of the catalyst, which lowers the activation energy for dissociation. Kim et.all. used Pd film as a gas activator to decrease the growth temperature of carbon nanotubes [11].

Among the metallic promoters, nonmetallic promoter materials are used in the growth process to decrease the diameter of CNTs. Sulphur and sulphur containing materials are effective in controlling the diameter as well as the number of walls of grown carbon nanotubes [12]. Sulphur can influence SWCNT growth by blocking active sites on the catalyst particle, lowering

the melting point of the catalyst, or interacting with the growing nanotube [13].

In the present paper the Single Wall carbon nanotubes (SWCNTs) were synthesized by means of Aerosol CVD method using pure sulphur as promoter together with iron catalyst.

EXPERIMENT

The synthesis process was carried out by conventional aerosol-assisted chemical vapor deposition (A-CVD) technique from SCIDRE, Germany, which uses liquid hydrocarbon as carbon source. MWCNTs with diameters of 10-85 nm and a small percent of SWCNTs with diameters of 0.85 and 1.14 nm has been grown by the aerosol chemical deposition method in our previous report [14].

A small amount of pure Sulphur powder was mixed with Ferrocene (Fe:S)=10:1 (atomic weight) and x-lene in a special flask, which then inside of high frequency (800 kHz) transducer transformed into the aerosol during the synthesis process. The growth processes were carried out at 850- 1000°C in the horizontal reactor at the atmospheric pressure. Ar/H₂ mixture was used as a transport gas which the total flow in the ratio of 10:1. H₂ gas was flowed to the system during the synthesis process. The system is cooled under the Ar flow.

The morphology of the samples was analyzed by scanning electron microscopy (Auriga cross beam SEM rom Carl Zeiss, installed in IMEM, CNR) and RBM mode of crystalline phases of the CNT samples were analyzed by Raman spectroscopy using Tokio Instruments Nanofinder 30 Confocal Laser Spectroscopy setup with green excitation laser beam at 532 nm. All the measurements were performed at room temperature. The Raman signal was collected by a back-thinned CCD.

RESULT AND DISCUSSION

In order to gain a better understanding of the role of sulphur in the growth of SWNTs by the aerosol CVD system, we produced different types of nanotube materials by varying the reaction furnace temperature from 850 to 1000°C, using a fixed Ferrocene/Sulphur concentration of 22mg/ml in x-lene. By analyzing the works of other authors [15, 16], we decided on 10:1 relation between Fe and S.

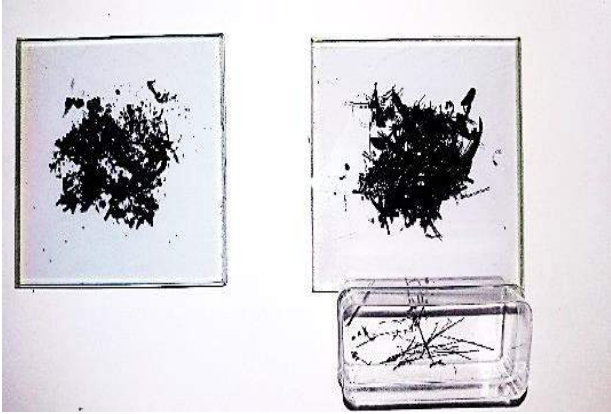


Fig. 1. Photography of the sample grown without (left) and with (right) pure Sulphur

Fig.1. shows produced CNTs without (left) and with (right) sulphur in the starting solution. Visually it is seen that the presence of the Sulphur leads to the formation of long (1,5-2.0 cm) whiskers (see right picture) and increase of yield.

We have analyzed one of such whiskers by SEM and show this in fig 2. On the picture it is seen as a twisted thin film.

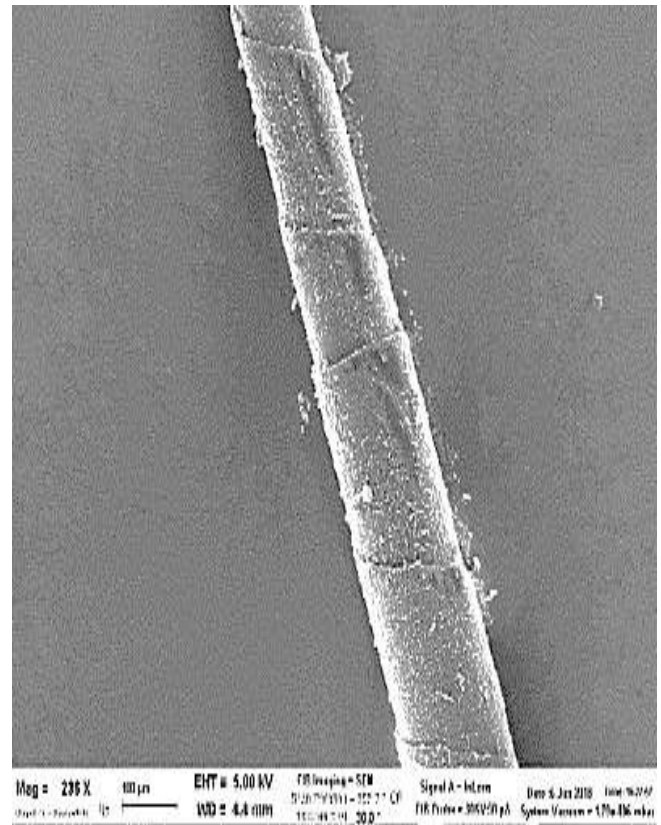


Fig.2. SEM image of one of the whisker

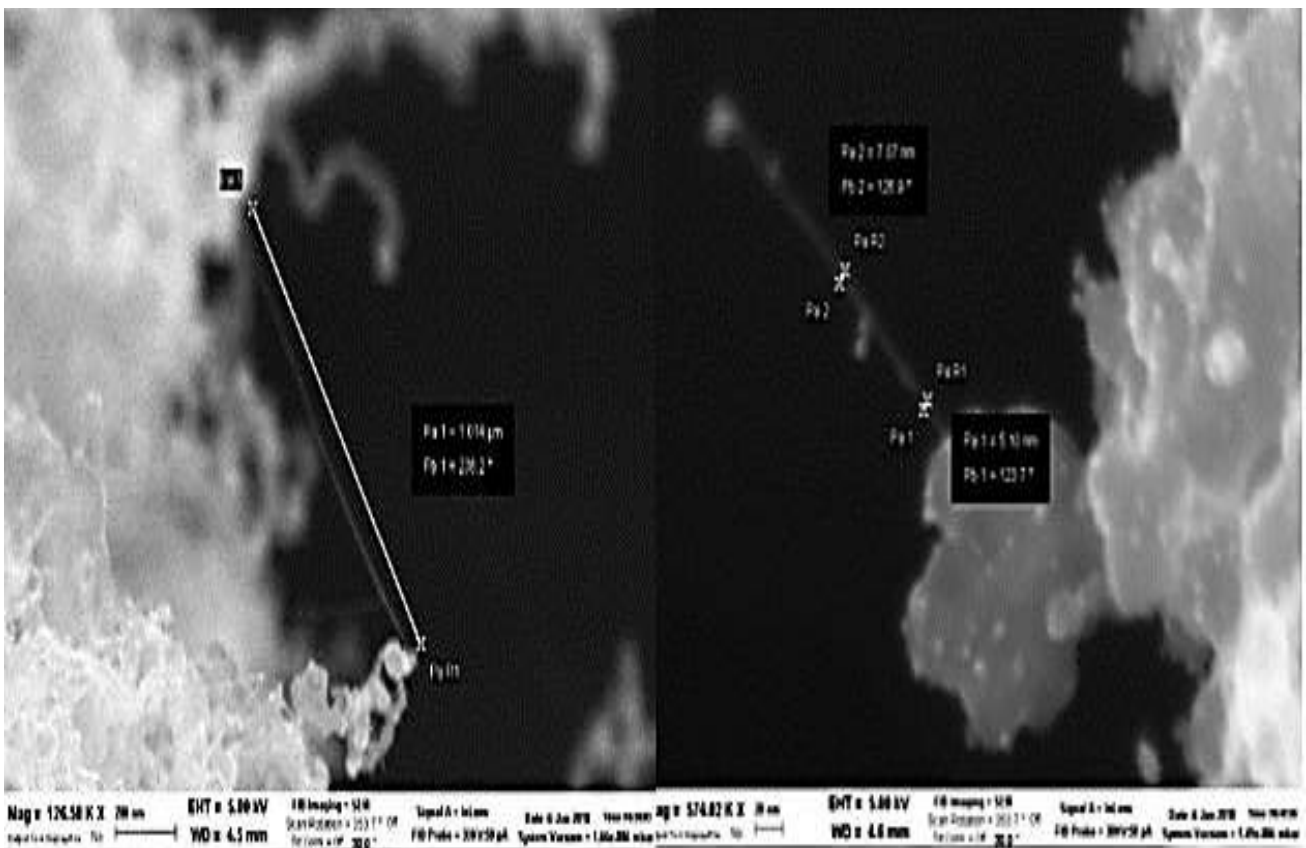


Fig.3. SEM image of the CNTs observed on twisted thin film

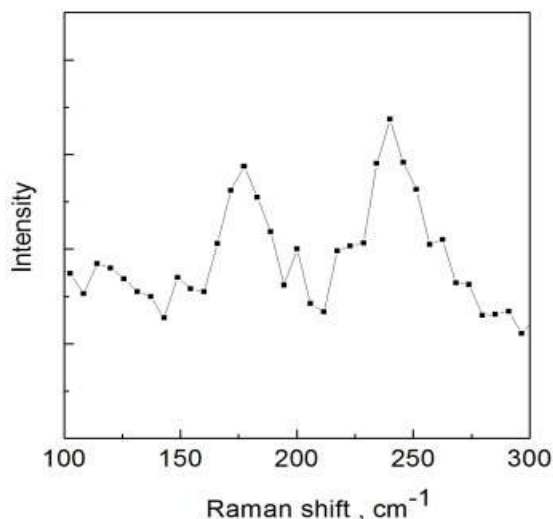


Fig.4. RBM bands of the Raman spectrum of the CNTs observed on twisted thin film

To confirm the obtained results the Raman spectroscopy analysis was carried out. The Raman experiment condition was the same as our previous works [14]. Radial breathing mode (RBM), which is characteristic of SWCNTs (due to easy vibration of single wall by low frequency signals), with peaks located at $X_{RBM}=178$ and 240 cm^{-1} , which confirms the presence of nanotubes of 1.4 and 1nm, respectively (Fig.4).

Regarding the crystallinity of the grown material, we could also use the intensity ratios between the D (defectiveness) and G (graphite) bands (Fig.5). As the D band becomes weaker, the material tends to be more crystalline. We calculated $D/G = 0.39$. Such value can explain the presence of amorphous carbon among with SWCNTs, and possibly the signal is also detected from a twisted film, which contains amorphous carbon. It is important to have amorphous carbon free single-wall carbon nanotubes.

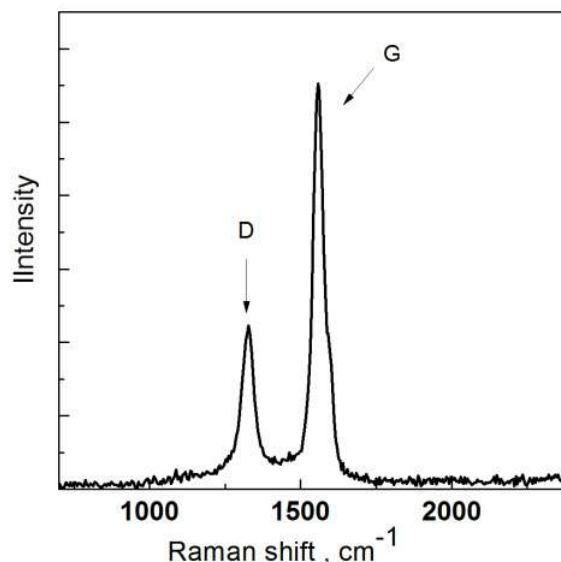


Fig.5. Raman spectrum of the CNTs grown on the twisted thin films

CONCLUSIONS

We concluded that using sulphur makes it easy to decrease the diameters of grown CNTs. By SEM the CNTs with 5 -7 nm diameters are observed, and from RBM peaks of the Raman spectra it is calculated that there are SWCNTs with 1-1,4 nm diameter.

ACKNOWLEDGMENT

This work was financially supported by the bilateral project between IMEM-CNR and Institute of Physics, ANAS. The authors would like to thank M.Bosi and Ch.Sultanov for carrying out of SEM measurements.

-
- [1] R.H. Baughman, A. A. Zakhidov, W. A. de Heer, "Carbon Nanotubes—The Route toward Applications," *Science*, Vol. 297, No. 5582, 2002, pp. 787-792. doi:10.1126/science.1060928
- [2] C. Journet, W.K. Maser, P.Bernier, A. Loiseau,; de La Chapelle, M. Lamy, S. Lefrant, P.Deniard, R. Lee, J. E. Fischer, "Large-scale production of single-walled carbon nanotubes by the electric-arc technique" *Nature*, Volume 388, Issue 6644, pp. 756-758 (1997). doi:10.1038/41972
- [3] Z.J. Shi, Y.F. Lian, F.H. Liao, et al. "Large scale synthesis of single-wall carbon nanotubes by arc-discharge method". *J. Phys Chem. Solids*. 61: 1031–1036. (2000); doi:10.1016/S0022-3697(99)00358-3
- [4] M. Zhang, M. Yudasaka, S. Iijima, "Single-wall carbon nanotubes: a high yield of tubes through laser ablation of a crude-tube target", *Chem. Phys. Lett.* 336: 196 – 200. (2001); doi:10.1016/S0009-2614(01)00101-4
- [5] J. Kong, A.M. Cassell, H. Dai, "Chemical vapor deposition of methane for single-walled carbon nanotubes", *Chem. Phys. Lett.* 292: 567 – 574. (1998); doi:10.1016/S0009-2614(98)00745-3
- [6] A. Magrez, J.W..Seo, R. Smajda, M. Mionić and L. Forró "Catalytic CVD Synthesis of Carbon Nanotubes: Towards High Yield and Low Temperature Growth", *Materials* 2010, 3, 4871 – 4891; doi:10.3390/ma3114871.
- [7] M. Kumar, Y. Ando "Chemical vapor deposition of carbon nanotubes: A review on growth mechanism and mass production", *J. Nanoscience. Nanotechnology*. 2010, 10, 3739 – 3758. doi:10.1166/jnn.2010.2939
- [8] C.J. Lee, J. Park, Kim, J.M.; Y. Huh, J.Y. Lee, K.S. No "Low-temperature growth of carbon nanotubes

- by thermal chemical vapor deposition using Pd, Cr, and Pt as co-catalyst”, *Chem. Phys. Lett.* 2000, 327,277–283. doi:10.1016/S0009-2614(00)00877-0
- [9] W.M. Yeoh, K.Y. Lee, S.P. Chai, K.T. Lee, A.R. Mohamed “The role of molybdenum in Co-Mo/MgO for large-scale production of high quality carbon nanotubes”, *J. Alloys Compd.* 493 (2010) 539–543. doi:10.1016/j.jallcom.2009.12.151
- [10] S.P. Chai, S.H.S. Zein, A.R. Mohamed “Preparation of carbon nanotubes over cobalt-containing catalysts via catalytic decomposition of methane”, *Chem. Phys. Lett.* 426 (2006) 345 – 350. doi:10.1016/j.cplett.2006.05.026
- [11] J.Kim, K.No, Ch. Jin Lee “Growth and field emission of carbon nanotubes on electroplated Ni catalyst coated on glass substrates”, *Journal of Applied Physics* 90, 2591 (2001); doi: 10.1063/1.1389761
- [12] Thomas P. McNicholas, Lei Ding, Dongning Yuan, and Jie Liu, “Density Enhancement of Aligned Single-Walled Carbon Nanotube Thin Films on Quartz Substrates by Sulfur-Assisted Synthesis”, *J. Nano Letters* Vol. 9, No.10 (2009) 3646 – 3650. doi:10.1021/nl901890x
- [13] M.S. Mohlala, et al. “Carbon nanotube synthesis using ferrocene and ferrocenyl sulfide. The effect of sulfur”. *Appl. Organomet. Chem.* 2007, 21 (4), 275–280. doi:10.1002/aoc.1176
- [14] S.Abdullayeva, N.N.Musayeva, C.Frigeri, A.B.Huseynov, R.B.Jabbarov, R. B.Abdullayev, Ch.A.Sultanov, R.F.Hasanov “Characterization of high quality carbon nanotubes synthesized via Aerosol –CVD”. *Journal of Advances in Physics*, 2015, Vol. 11, No. 4, pp.3229-324
- [15] R. Rahul, P. Neal, X. Zhang, W. Robert, M. Benji, T. Saikat *Materials Express*, Volume 1, Number 2, June 2011, pp. 160-166(7)
- [16] A. Barreiro, C. Kramberger, M.H. Rummeli, A. Gruneis, D. Grimm, S. Hampel, T. Gemming et al. “Control of the single-wall carbon nanotube mean diameter in sulphur promoted aerosol-assisted chemical vapour deposition”. *Carbon* 45 (2007) 55–61. doi:10.1016/j.carbon.2006.08.013

STRUCTURAL FEATURES OF MANGANESE CONTAINING TOPOLOGICAL INSULATORS THE BASIS OF Bi_2Te_3

I.R. AMIRASLANOV, Z.S. ALIYEV, P.A. ASGEROVA, A.B. NURIYEVA

Institute of Physics, Baku, Azerbaijan

iamiraslan@gmail.com

Synthesis, crystal growth, X-ray examination of Mn-Bi-Te system compounds was carried out. It is shown that individual compounds with the general formulas $\text{MnTe} \cdot n\text{Bi}_2\text{Te}_3$ (where $n = 1, 2, 3, \dots$) crystallize in this system. The existence in this series of compounds of $\text{MnBi}_8\text{Te}_{13}$ ($n = 4$) and $\text{MnBi}_{10}\text{Te}_{16}$ ($n = 5$) is shown for the first time. In this work, the structural characteristics of the compounds of this homologous series are also given.

Keywords: Topological insulators, synthesis, crystal growth, X-ray diffraction

PACs: . 64.70.K, 73.20. r, 73.25.+i, 73.50. h

Bi_2Te_3 has long been studied as one of excellent ambient-temperature thermoelectric materials. Recently, however, Bi_2Se_3 and Bi_2Te_3 have been of renewed interest because they are bulk topological insulators. Topological insulators (TIs) are insulators in bulk but show metallic conduction at the surface [1]. The conductive properties of the surface are a consequence of the strong spin-orbit interaction. The first experimentally discovered topological insulators were the $\text{Bi}_{1-x}\text{Sb}_x$ alloys. The same surface states were discovered in tellurides and selenides of bismuth and antimony: Bi_2Se_3 , Bi_2Te_3 , Sb_2Te_3 . In the seventies of the last century, the structures of Bi_2Te_3 crystals and many of its analogues were grown and solved. Authors showed that these crystals are layered and crystallize in the structural type of tetradymite. The contribution of the authors RM Imamov and SA Semiletov in the study of the crystal chemistry of these compounds was very large [2]. Almost forgotten these works after revealing their possession of the TI property again attracted the attention of scientists. So, Bi_2Te_3 is one of the most promising TIs. The blocks of this layered structure consist

of quintuples of Te-Bi-Te-Bi-Te. Of particular interest have the influence of magnetic impurities and ferromagnetism on the topological surface states. The Bi_2Te_3 compound is a convenient matrix for the incorporation of magnetic impurities. It is shown that when the manganese is inserted up to nine percent, the structure of Bi_2Te_3 type is preserved [3]. We examined the interactions of Mn-Bi-Te elements with melting, at higher manganese contents. A further increase in concentration leads to the formation of structural blocks consisting of seven atomic layers. The first such compound consisting of seven-layer blocks (septuple) is MnBi_2Te_4 . However, in the interval between Bi_2Te_3 and MnBi_2Te_4 , several layered compounds with the general formula $\text{MnTe} \cdot n\text{Bi}_2\text{Te}_3$ ($n = 1-5$) are formed. It is not difficult to make sure that the number "n" corresponds to the number of quintuples located between septuples. Among these compounds, the MnBi_2Te_4 structure has already been refined. For the values $n = 2$ and 3, namely, for MnBi_4Te_7 and $\text{MnBi}_6\text{Te}_{10}$ their structural analogues are known.

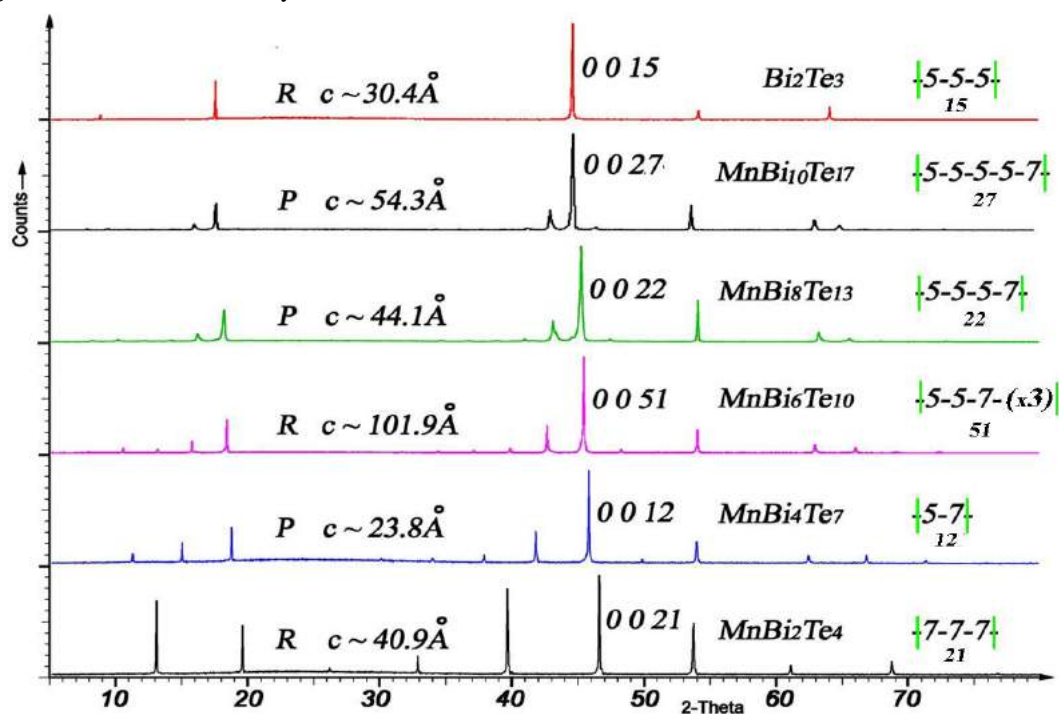


Fig. 1. The diffraction patterns of $\text{MnTe} \cdot n\text{Bi}_2\text{Te}_3$ ($n = 1-5$) and Bi_2Te_3 .

However, the formation of compounds with the compositions $\text{MnBi}_8\text{Te}_{13}$ ($n = 4$) and $\text{MnBi}_{10}\text{Te}_{16}$ ($n = 5$) for the first time we show. It should be noted that the growth of individual crystals of ternary phases of these compounds with dimensions of few millimeters for technologists is an impossible task. The main reason for this is the formation of a very stable MnTe phase at high temperatures. As a result of a long and painstaking work, we managed to isolate these phases in sizes of 1-3 mm. The fig 1 shows the diffraction patterns from cleaves of the selected crystals. In these pictures, reflexes like (00 l) are visible, which allow us to determine the "c" parameters of these phases.

As can be seen from the fig 1, in all these compounds the strongest reflexes are in the 2-theta range of 44-47°. It is easy to verify that the values of the index l of these reflexes are equal to the number of atomic layers in one unit cell. Also, with a decrease in the relative amount of manganese in the composition, this peak shifts toward a decrease in the value of the 2-theta. It is clear that this is

due to the difference in the ionic radii of the Mn and Bi atoms. As noted above, one cannot yet single-phase compounds of $\text{MnBi}_{2x}\text{Te}_{3x+1}$ formulations ($x=1,2,\dots$), but a mixture of several phases is always grown. Therefore, the determination of the exact positions of strong peaks in the range $2\theta= 44-47^\circ$ would unambiguously identify the phase composition of the sample.

X-ray diffraction analysis of the compounds MnBi_2Te_4 ($n = 1$) and MnBi_4Te_7 ($n = 2$) and $\text{MnBi}_6\text{Te}_{10}$ ($n = 3$) showed that in all these compounds the Te atoms are arranged in the cubic close packing type. Therefore, the value of the parameter $c=44.1\text{Å}$, shown in the fig 1 for $\text{MnBi}_8\text{Te}_{13}$ ($n = 4$), it is possible that it increases threefold. The fact is that the 22-layer structure cannot fit into a cubic package. Most likely, it will move into a 66-layer rhombohedral structure with the parameter $c\sim 132.3\text{Å}$. However, additional studies are needed to confirm this.

The report will discuss the structural features of the above-mentioned crystals.

-
- [1] *Hai-Jun Zhang, Chao-Xing Liu, Xiao-Liang Qi, Xiao-Yu Deng, Xi Dai, Shou-Cheng Zhang, and Zhong Fang.* Electronic structures and surface states of the topological insulator $\text{Bi}_{1-x}\text{Sb}_x$. *Phys. Rev. B* 80, 085307, 2009
- [2] *R. M. Imamov and S. A. Semiletov,* *Kristallografiya*, 15, No. 5, 972–978 (1970)
- [3] *Y. S. Hor, et al.* Development of ferromagnetism in the doped topological insulator $\text{Bi}_{2-x}\text{Mn}_x\text{Te}_3$. *Phys. Rev. B.* 81, 195203 (2010)

CONTENTS

1.	Spectral variability of the line HeI 5876Å/Be Herbig type star HD 179218 A.N. Adigezalzade	3
2.	Kramers-Kronig analysis of Ni _{1-x} Zn _x Fe ₂ O ₄ ferrites infrared diffuse reflectance spectra Sh.A. Ahmadova, A.A. Sadigova, Sh.N. Aliyeva, T.R. Mehdiyev	6
3.	Response of silver chalcogallates to X-rays S.M. Asadov, S.N. Mustafaeva, V.F. Lukichev	9
4.	Influence of fullerenes C ₆₀ on operating characteristics of liquid crystal MBBA T.D. Ibragimov, A.R. Imamaliyev, G.F. Ganizade	11
5.	De Sitter cosmological model and the problem of dark matter and energy B.A. Rajabov	13
6.	New electromagnetic methods of slowdown and trapping of particles Azad Ch. Izmailov	15
7.	Synthesis and photoluminescent properties of iodinated multi walled carbon nanotubes S. H. Abdullayeva, S.A. Mammadova, A.B. Huseynov, A.O. Israfilov	19
8.	Neutron diffraction study of As ₄₀ Se ₆₀ , As ₄₀ Se ₃₀ S ₃₀ , As ₄₀ Se ₃₀ Te ₃₀ chalcogenide glasses R.I. Alekberov, A.I. Isayev, S.I. Mekhtiyeva, M. Fábíán	21
9.	Preparation and study of electrically conductive ceramic nanocomposites based on the Azerbaijan bentonite raw material and multi-walled carbon nanotubes S.H. Abdullayeva, A.B. Huseynov, A.O. Israfilov, S.A. Mammadova	24
10.	Refinement the crystal structure of the Ga _{1-x} In _{1+x} S ₃ A.B. Rahimli, I.R. Amiraslanov	27
11.	Influence of interfacial phases on thermal and electrical conductivity in GaSb-CrSb eutectic system M.V. Kazimov, D.H. Arasly, İ.Kh. Mammadov, R.N. Rahimov, A.Ə. Khalilova	29
12.	Temperature dependence of photoluminescence of ZnIn ₂ Se ₄ T.G. Kerimova, I.A. Mamedova, Z. Kadiroglu, N.A. Abdullayev, M. Feldman	33
13.	Investigation of low dimensional materials on sapphire substrate for sensor application Sevda Abdullayeva, Gulnaz Gahramanova, Nahida Musayeva, Teymur Orujov, Rasim Jabbarov	36
14.	The structural features of crystalline phases of the GaSe-InSe system I.R. Amiraslanov, K.K. Azizova, S.S. Babayev, Y.R. Aliyeva	39
15.	Influence of temperature, frequency and composition of TlIn _{1-x} Er _x Se ₂ solid solutions on their dielectric permittivity and conductivity A.M. Pashaev, E.M. Kerimova, S.N. Mustafaeva	42
16.	IBR-2 - pulsed source for neutron scattering research at JINR V.N. Shvetsov	44
17.	Superlattice structure of YbAs ₄ S ₇ nano thick films E.Sh. Hajiyev	47
18.	Role of sulphur in the A- CVD growth of single wall CNTs R.F. Hasanov, N.N. Musayeva, S.S. Babayev	49
19.	Structural features of manganese containing topological insulators the basis of Bi ₂ Te ₃ I.R. Amiraslanov, Z.S. Aliyev, P.A. Asgerova, A.B. Nuriyeva	53



www.physics.gov.az